Optical Second Harmonic Generation and Pump-Probe Reflectivity Measurements from Si/SiO$_2$ interfaces

by

Gibson Peter Nyamuda

Dissertation presented for the degree of **Doctor of Science** at Stellenbosch University

Promoter: Prof. E.G. Rohwer, University of Stellenbosch

Faculty of Science, Department of Physics

Co-promoters: Dr. C.M. Steenkamp, University of Stellenbosch

Faculty of Science, Department of Physics and

Prof. H. Stafast, Friedrich-Schiller-University, Germany

Faculty of Physics and Astronomy, Department of Physics

December 2010

Declaration

By submitting this dissertation electronically, I declare that the entirety of the work contained therein is my own, original work, and that I have not previously in its entirety or in part submitted it for obtaining any qualification.

December 2010

Abstract

Silicon/silicon dioxide (Si/SiO_2) interface is widely used in microelectronics as the gate between the drain and source of most metal oxide semiconductor field effect transistors (MOSFETs). The functionality, reliability and electrical properties of such transistors are strongly dependent on the quality of the Si/SiO_2 structure forming the gate. Characterization of the Si/SiO_2 interface is important in understanding device degradation therefore the Si/SiO_2 interface is a subject of intensive investigation. Research studies of Si/SiO_2 interfaces using optical methods have been reported by many groups around the world but to date many open questions still exist. The physics of photoinduced trap or defect generation processes and the subsequent trapping of charge carriers, the precise role of photoinduced interfacial electric field in altering optical properties of the Si/SiO_2 interface and its role in affecting the second harmonic (SH) yield measurements are not well understood.

In this work a commercial near infrared femtosecond (fs) laser source [1.55 eV, 75 $\pm$ 5 fs, 10 nJ, 80 MHz] is used to study native Si/SiO_2 interfaces of free standing single crystalline Si membrane and bulk Si. Optical second harmonic (SH) generated at the Si/SiO_2 interfaces of a Si membrane in reflection and for the first time in transmission is demonstrated as well as stationary, single colour, pump-probe reflectivity measurements from the Si/SiO_2 interface of bulk n-type Si. The experimental setups for the second harmonic generation (SHG) and pump-probe techniques were designed and implemented, and measurements were recorded by a computer controlled data acquisition system. Free standing Si membrane samples were successfully produced at the Institut für Photonische Technologien (IPHT) in Jena, Germany from bulk Si using a chemical etching process and were characterised using the z-scan technique.

The penetration depth of light with a photon energy of 1.55 eV in silicon allows transmission of the fundamental fs laser pulses through the Si membrane ($\sim$ 10 μm in thickness) and this is exploited to generate a SH signal in transmission from the Si/SiO_2 interfaces of the Si membrane. In the presence of sufficiently intense fs laser light defects are created at the

interfaces and populated by multiphoton transfer of charges from Si to SiO_2 where they are subsequently trapped. The transfer of charge establishes interfacial electric fields across the interfaces of the Si membrane and this enhances SHG. This phenomenon is called electric field induced second harmonic (EFISH) generation. To our knowledge, EFISH measurements from interfaces of Si membrane performed in transmission are demonstrated for the first time in the present study. The demonstration of EFISH in transmission revealed new results which allowed us to provide additional perspectives on the EFISH generation process at Si/SiO_2 interfaces never reported before. The temporal response of SH signals from virgin spots were recorded at different incident laser powers for both reflection and transmission geometries. The SH responses measured in transmission were observed to be time dependent and show an increase during irradiation of the sample corresponding to EFISH process.

A series of SH measurements were recorded at different laser powers to compare the magnitudes of SH yield in each detection geometry for a single Si/SiO_2 interface. The magnitude of the SH yield measured in transmission was higher than expected and surpassed the SH yield measured in reflection. The expectation is based on the fact that the local intensity of the fundamental beam at the second interface where the SH in transmission is generated is low compared to the local intensity at the first interface where the SH in reflection originates. A physical model is developed to consistently interpret the experimental results obtained in this study. In this model we established the origin of EFISH signals in each detection geometry, explain the unexpected high SH signals measured in transmission and provide an analysis of the time constants extracted from SH response in transmission and reflection.

In addition, we also report for the first time stationary pump-probe reflectivity measurements from bulk n-type Si(111) samples with native oxide. A strong pump beam was focused on the same spot as a weak probe beam from the same fs laser source. The change in reflectivity of the $Si(111)/SiO_2$ system was recorded by monitoring the change in intensity of the weak reflected probe beam. The temporal evolutions of the reflectivity of the material were recorded at different pump powers. The reflectivity of the material increases over several minutes of irradiation and reaches steady-state after long time irradiation. The change in reflectivity of the material is attributed to a nonlinear process called Kerr effect, and the temporal response

arises from the photoinduced interfacial electric field across the Si(111)/SiO$_2$ interface caused by multiphoton charge transfer from bulk Si(111) to the SiO$_2$ layer.

The results reported in this study contribute to the understanding of the photoinduced interfacial electric field caused by charge carrier separation across buried solid-solid interfaces. They also reveal nonlinear optical processes such as the Kerr effect caused by charge dynamics across the interface in addition to the well known SHG process.

Opsomming

Die silikon/silikon dioksied (Si/SiO$_2$) skeidingsvlak word algemeen gebruik in mikro-elektronika as die hek tussen die put en die bron van die meeste metaaloksied halfgeleier veld-effek transistors (MOSFETs). Die werkverrigting, betroubaarheid en elektriese eienskappe van sulke transistors word grootliks bepaal deur die kwaliteit van die Si/SiO$_2$ struktuur wat die hek vorm. Karakterisering van die Si/SiO$_2$ skeidingsvlak is belangrik om die degradering van die transistor te verstaan en daarom is die Si/SiO$_2$ skeidingsvlak die onderwerp van intensiewe ondersoek. Ondersoek van die Si/SiO$_2$ skeidingsvlak deur van optiese metodes gebruik te maak is geraporteer deur verskeie internasionale groepe, maar daar bestaan tot vandag toe nog n groot aantal onbeantwoorde vrae. Die fisika van die fotogenduseerde generering van defekte en van posisies waarin ladings gevang kan word, asook die daaropvolgende vasvang van ladingsdraers, die presiese rol van die fotogeïnduseerde elektriese veld oor die skeidingsvlak in die verandering van die optiese eienskappe van die Si/SiO$_2$ skeidingsvlak en die grootte van die tweede harmoniek (SH) sein word nog nie goed verstaan nie.

In hierdie werk word n kommersile naby-infrarooi femtosekonde (fs) laserbron [1.55 eV, 75 $\pm$ 5 fs, 10 nJ, 80 MHz] gebruik om natuurlike Si/SiO$_2$ skeidingsvlakke van vrystaande enkelkristallyne Si membrane en soliede Si te bestudeer. Optiese tweede harmoniek (SH) wat by die Si/SiO$_2$ skeidingsvlakke van 'n Si membraan gegenereer word - in refleksie en vir die eerste keer in transmissie - is gedemonstreer, asook stasionêre, een-golflengte pomp-toets refleksiemetings op die Si/SiO$_2$ skeidingsvlak van soliede n-gedoteerde Si. Die eksperimentele opstellings vir die tweede harmoniek generering (SHG) en pomp-toets tegnieke is ontwerp en uitgevoer en metings is opgeneem deur 'n rekenaarbeheerde dataversamelingstelsel. Vrystaande Si membraan monsters is suksesvol by die Institut für Photonische Technologien (IPHT) in Jena, Duitsland vervaardig uit soliede Si deur 'n chemiese etsproses en is gekarakteriseer met behulp van die z-skanderingstegniek as deel van hierdie studie.

Die diepte waartoe lig met 'n fotonenergie van 1.55 eV in silikon indring laat die transmissie van die fundamentele fs laserpulse deur die Si membraan (met $\sim$ 10 μm dikte) toe en dit word ontgin om 'n SH sein van die Si/SiO$_2$ skeidingsvlakke van die Si membraan in transmissie te meet. In die teenwoordigheid van fs laserlig met voldoende intensiteit word defekte by die

skeidingsvlakke geskep en bevolk deur meer-foton ladingsoordrag van die Si na die SiO_2 waar die ladings daaropvolgens vasgevang word. Die oordrag van ladings skep elektriese velde oor die skeidingsvlakke van die Si membraan en dit versterk die SHG. Hierdie verskynsel word elektriese veld geïnduseerde tweede harmoniek (EFISH) generering genoem. Sover ons kennis strek is die meting van EFISH seine van skeidingsvlakke van Si membrane in transmissie vir die eerste keer in hierdie studie gedemonstreer. Die demonstrasie van EFISH in transmissie het nuwe resultate opgelewer wat ons toegelaat het om bykomende perspektiewe op die EFISH genereringsproses by Si/SiO_2 skeidingsvlakke te verskaf waaroor nog nooit vantevore verslag gedoen is nie. Die tydafhanklike gedrag van die SH seine van voorheen onbestraalde posisies is gemeet by verskillende drywings van die inkomende laserbundel vir beide die refleksie en transmissie geometrieë. Die gedrag van die SH sein in transmissie is waargeneem om tydafhanklik te wees en 'n toename te toon gedurende bestraling van die monster in ooreenstemming met EFISH prosesse.

'n Reeks van SH metings is opgeneem by verskillende laserdrywings om die groottes van die SH opbrengste in elke meetgeometrie vir 'n enkele Si/SiO_2 skeidingsvlak te vergelyk. Die grootte van die SH opbrengs wat in transmissie gemeet is was hoër as verwag is en het die grootte van die SH opbrengs in refleksie oortref. Die verwagting is gebaseer op die feit dat die lokale intensiteit by die tweede skeidingsvlak waar SH in transmisie gegenereer word relatief laag is in vergelyking met die lokale intensiteit by die eerste skeidingsvlak waar SH in refleksie ontstaan. 'n Fisiese model is ontwikkel om die eksperimentele resultate wat in hierdie studie verkry is op 'n konsekwente wyse te interpreteer. In hierdie model het ons die oorsprong van EFISH seine in elke meetgeometrie vasgestel, die onverwagte hoë SH seine wat in transmissie gemeet is verklaar en 'n analise van die tydkonstantes wat uit die SH gedrag in transmissie en refleksie afgelei is gedoen.

Verder rapporteer ons ook vir die eerste keer stasionêre pomp-toets reflektiwiteitsmetings van soliede n-gedoteerde Si(111) monsters met 'n natuurlike oksied. 'n Sterk pompbundel is gefokus op dieselfde posisie as 'n swak toetsbundel van dieselfde laserbron. Die verandering in reflektiwiteit van die Si(111)/SiO_2 stelsel is gemeet deur die verandering in die intensiteit van die swak weerkaatste toetsbundel te monitor. Die tydevolusie van die reflektiwiteit van die mate-

riaal is gemeet by verskillende pompdrywings. Die reflektiwiteit van die materiaal neem toe gedurende etlike minute van bestraling en bereik 'n stasionêre toestand na 'n lang tyd van bestraling. Die verandering in reflektiwiteit van die materiaal word toegeskryf aan 'n nie-liniêre prosess, naamlik die Kerr effek, en die tydafhanklike gedrag ontstaan as gevolg van die fotogeïnduseerde elektriese veld oor die $Si(111)/SiO_2$ skeidingsvlak wat veroorsaak word deur meer-foton ladingsoordrag van die soliede $Si(111)$ na die SiO_2 laag.

Die resultate wat in hierdie studie gerapporteer word dra by tot die verstaan van die fotogeïnduseerde elektriese veld oor die skeidingsvlak wat veroorsaak word deur die skeiding van ladingsdraers oor die bedekte kristal-kristal skeidingsvlak. Dit lê ook nie-liniêre optiese prosesse soos die Kerr effek bloot wat veroorsaak word deur die dinamika van ladings oor die skeidingsvlak, bykomend tot die bekende SHG proses.

Acknowledgements

I would like to thank the German Academic Exchange Programme - Deutscher Akademischer Austausch Dienst (DAAD) for funding my doctoral studies including a research visit to Germany and the National Research Foundation for purchasing some of the project equipment.

I would like to express my sincere gratitude to the following people who contributed significantly to this project

- Prof E.G. Rohwer and Dr C.M. Steenkamp for their supervision, support in many ways and numerous discussions which have contributed to the success of this project.

- Prof H. Stafast for project insights and his help during my research visit to Germany.

- Dr P.H. Neethling for useful discussions on the project.

- All members of the Laser Research Institute for their excellent collaboration and useful discussions.

- All members of the IPHT, Jena in Germany for their assistance during my research visit in particular Dr W. Paa, Dr F. Garwe, Mr A. Bochmann and Dr E. Kessler. Special mention goes to Dr E. Kessler for manufacturing samples used in this study.

- Last but not the least my lovely wife and daugther who endured my absence as I work on this project, my parents, sisters, brothers and friends for their love and support. **Above all I thank God who make all things possible.**

Contents

List of Figures

List of Tables

Chapter 1

Introduction

The lifetime and performance of most silicon based metal-oxide-semiconductor (MOS) devices strongly depends on the quality of silicon/silicon dioxide (Si/SiO$_2$) interfaces, therefore characterization of these interfaces and understanding mechanisms that lead to degradation is important in the functionality and reliability of these electronic devices. The SiO$_2$ is used as a gate dielectric between the conducting channel, source and drain of metal-oxide-semiconductor field-effect transistors (MOSFETs) making Si/SiO$_2$ the world's most economically and technologically important interface.

The ever-rising demand for high speed, smaller, more reliable and power economic electronics in modern technology, has caused most silicon based components to reach the fundamental limit of their scaling [2]. As component density of microelectronic integrated circuits continue to increase, the size of the MOSFET shrinks, leading to the corresponding reduction of gate dielectric oxide from microns to few nanometres (5 nm or less) [3]. New technological problems will arise as a result of reduction in size of the gate oxide insulating layer and these include the dielectric thickness variation, dopant penetration through the SiO$_2$ [2], high leakage current from the channel to the gate electrode as a result of quantum tunnelling leading to excess power dissipation [2], enhanced scattering of carriers in the channel [4] which can compromise the functionality of these electronic devices.

Due to its technological relevance the Si/SiO_2 interface has received enormous scientific attention by various researchers around the world. Si/SiO_2 is a prototype material system, in particular for the study of ultrathin oxides (< 5 nm). The structural, optical, as well as the electronic properties of nanoscale Si/SiO_2 structures are of great interest to understand since surfaces and interfaces exhibit properties and behaviours that are distinctively different from those of the bulk material. The microscopic structure, morphology and oxidation kinetics of SiO_2 are subjects of intensive investigation. Much of the work in the past and present is to understand creation of defects in SiO_2, whether they are hole traps, electron traps or interface states, and their direct relationship to device breakdown [5, 6].

Optical second harmonic generation (SHG) has been demonstrated as a powerful tool for contact-less, non-invasive with in-situ capabilities of studying buried interfaces which are not accessed by other techniques [2, 3]. It is a sensitive technique for studying surfaces [7, 8], and interfaces of centrosymmetric material such as Si/SiO_2 interface [3]. The atomic scale surface and interface sensitivity make optical SHG a powerful probe to access the structural, optical, as well as electronic properties of solid-solid interfaces [9] such as Si/SiO_2 interfaces. Due to its unique characteristics such as the ability to induce optical defects, ionization of defects or trapping charges, the Si/SiO_2 interface has been studied extensively by optical SHG to understand charge dynamics and their effect on the electronic properties of the interface. When the interface is irradiated with sufficient intensities charge transfer and trap sites are induced at the interface through a nonlinear process and some of the charges are trapped in the oxide and this establishes a quasi-static interfacial electric field. The induced electric field across the interface will enhance SHG through a process called electric field induced second harmonic (EFISH) process.

We report on two main experiments performed on Si/SiO_2 interfaces of Si membrane[1] and bulk n-type Si. Firstly, SHG using fs laser was employed to study Si/SiO_2 interfaces of Si membrane in reflection and transmission geometries. SHG measured in transmission using Si membrane samples is demonstrated for the first time in this study. The membrane is a unique sample with two Si/SiO_2 interfaces which can be optically probed to measure both the EFISH

---

[1]The words silicon membrane or membrane shall be used interchangeably throughout this document to refer to free standing single crystalline silicon of thickness of ~ 10 μm fabricated in this study.

in transmission and reflection. We observed a time dependent EFISH response in transmission which depicts well known time dependent SH response in reflection from Si/SiO_2 interfaces of bulk Si. The temporal evolution of the SH response in transmission and reflection from the Si membrane were measured and compared at different incident laser powers. The time constants extracted from the time dependent SH response measurements in reflection reproduced what is reported in literature. The origin of the time dependent EFISH signal in each detection geometry is established in particular for transmission measurements using both experimental results and calculations based on the optical properties of Si.

The magnitude of the SH signals from Si membrane were measured in reflection and transmission at different incident laser powers. A comparison of the SH yield measured in both detection geometries revealed that the SH signals measured in transmission are higher than expected. The magnitude of the SH signals measured in transmission are approximately three times greater than in reflection despite being probed by much lower incident laser intensities. The unexpected SH signals measured in transmission has opened a new dimension which has never been reported before of interpreting EFISH signals at Si/SiO_2 interface.

Secondly, we report on a new phenomenon of time dependent reflectivity which was observed from Si/SiO_2 interface of bulk n-type Si(111). The results are reported for the first time in this study and were obtained using stationary, single colour pump-probe technique. The experimental setup for pump-probe measurements performed in reflection was designed and implemented. The change in reflectivity was recorded from a weak probe beam after irradiating the same spot with a strong pump-beam while both the pump and probe beams are stationary. The change in reflectivity increased with time over several minutes of irradiation. The experiment was repeated for different pump powers and time constants were extracted from each time dependent reflectivity curve. The analysis of the extracted time constants and their interpretation are discussed.

1.1   Outline

The dissertation is presented as follows:

Chapter 2 provides a brief overview of the research accomplished by SHG as a diagnostic tool particularly in the study of Si/SiO_2 interfaces. Different ways in which SHG has been employed by various researchers around the world to study oxide morphology, effect of annealing, chemical contamination, interface roughness and defect related studies are reported.

In Chapter 3, the background theory that is necessary for understanding the experimental work reported in later chapters is given. The formalism describing the interaction of light and matter is outlined and relevant nonlinear processes are summarised. The theory and model for SHG from surfaces of noncentrosymmetric media including the general EFISH phenomena are presented.

Chapter 4 describes the experimental setup and methods used in this study. A description of the laser system used in this work is given and the necessary laser parameters are provided. Sample preparation and characterization methods are summarised. The experimental setups for SHG in transmission and pump-probe reflectivity measurements are described.

The experimental results obtained from this study are presented in Chapter 5. A detailed discussion of the results using related previous studies in literature is given in Chapter 6. New results on transmission SHG and pump-probe reflectivity measurements are discussed. A physical model to explain EFISH measurements from Si membrane is presented. Finally the summary and conclusions of the work done in this study and possible future investigations are presented in Chapter 7.

Chapter 2

Research Overview

The application of SHG on silicon surfaces as a probe technique was first reported by Bloember-gen and coworkers in 1968 [10] in which the dependence of SHG yield with incident angle from the sample surface was demonstrated in reflection. A decade later, experiments on rotational anisotropy on Si/SiO_2 interfaces were reported by Tom and coworkers [11]. The rotational pattern for different polarization combination of input and output beams was used to study Si(100) and Si(111) surfaces. The two silicon samples were found to exhibit a strong SHG dependence on the angle of rotation about the surface normal. The rotational pattern from Si(100) and Si(111) were different indicating the difference in surface structural symmetry.

Two years later Heinz et al [12] used the polarization dependence of the rotational anisotropy to distinguish surface reconstruction in Si(111) sample surface. The rotational anisotropy pattern was shown to be sensitive to different phases of surface reconstruction caused by the different bonding configurations of surface atoms which produce neighbouring dangling bonds. This marked the use of SHG technique as a surface-sensitive tool for surface probing and thereafter rotational anisotropy was applied in various surface investigations such as vicinal surfaces with steps and terraces [13, 14, 15, 16], structure strain [17, 18], microroughness [19, 20, 21], chemical modifications of the interface [22, 23, 24, 25, 26, 27], and oxide thickness and annealing effect [14, 28, 29, 30].

Chemical modifications of the interface results in the dramatic change of the nonlinear response. The modification of interfaces by using chemicals can be introduced by direct wet chemical process [27] or by annealing the oxide in the presence of different gases such as hydrogen and nitrogen. It was observed that the peak height in the rotational anisotropy pattern did not change with nitrogen annealing but decreased with hydrogen annealing while the anisotropy pattern is conserved in both cases [25, 29]. The decrease in peak height is due to the reduction of the nonlinear susceptibility tensor components caused by hydrogen termination of interface dangling bonds in the direction normal to the interface [25].

The rotational anisotropy of the SH signal from the Si/SiO_2 interface with a thermally grown SiO_2 film was observed to change with different annealing procedures. The effect of annealing can cause highly oriented microcrystallites at buried interfaces [13] and the orientation also depends on annealing conditions such as time and temperature. According to Hirayama and Watanabe [28] annealing of native oxide changes the imperfect oxidation state of the oxide layer to become stoichiometric. The stoichiometric change causes the oxide layer to expand and increases the interface stress which can be compensated by creation of interface dangling bonds. The dangling bonds are generated by the release of interface stress caused by lattice expansion, which is accompanied by stoichiometric change from SiO_x $(x < 2)$ to SiO_2. This can change atomic layer arrangement at the interface and the SHG rotational anisotropy reflects the change.

Optical second harmonic spectroscopy has also been demonstrated as a powerful tool for studying charge transfer across the Si/SiO_2 interface. The SHG spectrum is measured while the photon energy of the incident radiation is changed. A strong electric-field induced SH contribution is caused by electron capture in the oxide layer, which is resonantly enhanced at the SH photon energy close to the bulk E_1 critical bandgap (3.3 eV) transition in silicon [31]. Lim et al [32] showed that the E_1 SH resonance can be red shifted or blue shifted depending on the chemical treatment of silicon. It was shown that variations in peak position and normalized SHG intensity among the spectra are favourable for the application of SHG in monitoring the progress of surface chemical reactions [33].

SHG was also demonstrated to be extremely sensitive to presence of electric fields. Aktsipetrov

and coworkers [34] were the first to demonstrate that SHG signal changes with externally applied voltage over a metal-oxide-semiconductor (Si-SiO$_2$-Cr) device. The SH signal that can be measured in the presence of applied or induced electric fields is called EFISH signal. EFISH measurements were later demonstrated in other semiconductors such as gallium nitride [35]. In these EFISH experiments the measured SH signal was observed to increase with the applied external voltage. In centrosymmetric media the application of external voltage to the crystal breaks the symmetry and the SHG can originate from the bulk crystal. In non-centrosymmetric media the increase in the external bias voltage increases the strength of the third order susceptibility tensor which then increases SH signal generated from the crystal.

EFISH signals can be time dependent, the first time dependent EFISH measurements on Si/SiO$_2$ were reported by Mihayachuk and coworkers [36] in the absence of any external bias. It was reported that a small interfacial electric field can be established at the Si/SiO$_2$ interface upon irradiating with 110 fs laser pulses at average irradiance of about 10 kW/cm^2. The SHG measured from the interface depends on the strength of the induced interfacial electric field. The time dependent EFISH signal was attributed to photoinduced charge transfer across the Si/SiO$_2$ interface inducing an interfacial electric field which then alters the interfacial nonlinear susceptibility tensor. The transferred charges from Si to SiO$_2$ are trapped in the oxide and detrapping occurred in time scales of several minutes much slower than bulk carrier recombination times. The magnitude of the induced electric field depends on the strength of charge transfer across the interface. For surface charge density of $\sim 10^{12}$ cm^{-2}, electric fields can be as high as $\sim 10^5$ V/cm because the interfacial electric field occupies few surface atomic layers of Si making the contribution to SHG observable [36]. It was observed that during irradiation the SH signal rises within time scales of several seconds to reach a saturation value.

Surface charging and electron trapping on Si/SiO$_2$ during electron bombardment [37], X-ray irradiation [38] and ultraviolet (UV) irradiation [39, 40] were also investigated by monitoring the temporal response of the SH signal generated by a laser. Electron bombardment causes prior trap filling of oxide defects therefore the SH signal showed an initial accelerated rise when probed by the laser. The SHG response from Si/SiO$_2$ samples before and after X-ray irradiation was shown to be different especially after longer dark times for example 8 hours

after irradiation time [38]. X-ray irradiation caused permanent defects on the sample. Fomenko and Borguet [39] used Hg/Ar lamp to irradiate Si/SiO$_2$ for 2 hours in ambient air, the samples were latter probed by SHG at different times for up to 20 hours after exposure to UV. The measured SH signal revealed that charges photoinjected to SiO$_2$ during UV irradiation relax back to Si at different rates with electrons being faster than holes. Comparative studies of clean Si/SiO$_2$ and preexposed to UV laser pulses (308 nm, 16 ns, $\sim$ 2.8 J/cm^2) were carried out by Scheidt et al [40]. A dose dependent modification of the SiO$_2$ due to thermally driven interface chemistry was observed using SH imaging when different fluences of UV irradiation were applied to samples.

An elaborate investigation in the variation of time dependent EFISH signals from bulk boron doped Si(100) of different doping concentrations was reported by Scheidt et al [41, 42]. The temporal behaviour of the SH signal in highly doped ($<$ 0.01 Ωcm) samples was shown to be different from undoped or lowly doped samples. The difference in the time dependent SH signal was also observed to differ with the magnitude of the incident laser intensity. This is explained by the presence of doping dependent intrinsic electric field and the different rates in which charges (holes and electrons) are photoinjected into the oxide. An enhancement SH signal after dark time was observed when the incident intensity was enough to induce hole transfer from Si to SiO$_2$. The enhancement of the SH signal was not evident when the samples were radiated at low intensity which is dominated by electron transfer process only showing that hole effect is an intensity dependent process and is possible at high intensity.

All SHG experiments on Si/SiO$_2$ interfaces summarized above were performed by measuring the SH signal reflected from the surfaces of bulk silicon. In this study a new approach is reported in which the SHG is measured in transmission. This was made possible by fabricating suitable thin Si samples which allow sufficient laser light to be transmitted by the sample.

Chapter 3

Theoretical Background

This chapter describes the theory of interaction of light with matter starting from Maxwell's equations. A description of the EFISH in transmission with relevant equations is given. The theory of SHG is summarized and a brief theoretical description of nonlinear processes such as second harmonic generation, multiphoton absorption and nonlinear refractive index is presented.

3.1 Interaction of Light and Matter

At relatively low intensities that normally occur in nature, the optical properties of materials are independent of the intensity of illumination. If the waves are able to penetrate and pass through the medium, this occurs without interaction between the waves [43]. If the intensity is high enough, as become possible with invention of lasers, optical properties start to depend on the intensity of the light and other characteristics of light. Light waves start to interact with each other as well as with the medium.

Generally, light propagation through a medium can be described classically by the Maxwell

equations as [44]

$$\nabla . \mathbf{D} = \rho \tag{3.1}$$

$$\nabla \times \mathbf{E} = -\frac{\partial \mathbf{B}}{\partial t} \tag{3.2}$$

$$\nabla . \mathbf{B} = 0 \tag{3.3}$$

$$\nabla \times \mathbf{H} = -\frac{\partial \mathbf{D}}{\partial t} + \mathbf{J} \tag{3.4}$$

where $\mathbf{D}$ is the electric displacement field, ρ is the electric charge density, $\mathbf{E}$ is the electric field strength, $\mathbf{H}$ is the magnetic field strength and $\mathbf{J}$ is the electric current density. In media the relationship between $\mathbf{E}$, $\mathbf{D}$ and $\mathbf{P}$ is given by

$$\mathbf{D} = \varepsilon_o \mathbf{E} + \mathbf{P} \tag{3.5}$$

with the macroscopic polarisation $\mathbf{P}$, and similarly for the $\mathbf{B}$-field and the $\mathbf{H}$-field

$$\mathbf{B} = \mu_o (\mathbf{H} + \mathbf{M}) \tag{3.6}$$

with magnetization $\mathbf{M}$. We consider materials which are charge free, current free and non-magnetic that is $\rho = 0$, $\mathbf{J} = 0$ and $\mathbf{M} = 0$. Using equations 3.1 to 3.6, Maxwell equations can be summarized as

$$\nabla^2 \mathbf{E} = \mu_o \frac{\partial^2 \mathbf{D}}{\partial t^2}. \tag{3.7}$$

In dielectric medium the charged particles are bound together. If electromagnetic radiation is incident on the material only electrons are capable of following the rapid oscillations of light frequency ($\sim 10^{13}$ - 10^{17} Hz) therefore electrons form oscillatory dipoles with positive charged ion-cores. According to the Lorentz model, a bound electron is pictured as a simple harmonic oscillator. Under a low intensity incident oscillating electric field, the electron will undergo small displacements about its equilibrium position described by harmonic oscillator model [45]. The restoring force is linear and the system follows a harmonic potential. The

electron's response can be described by the linear polarisation term

$$\mathbf{P} = \varepsilon_o \chi^{(1)}.\mathbf{E}, \tag{3.8}$$

where $\chi^{(1)}$ is the linear susceptibility tensor of the medium.
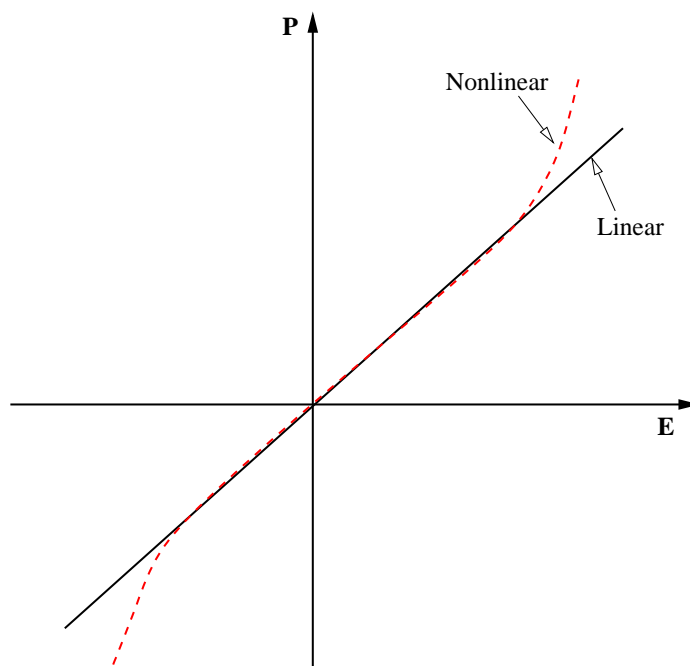
Figure 3.1: The induced polarisation **P** as a function of the applied field **E** for linear and second-order nonlinear materials.

The induced polarisation in the material under the weak field varies linearly with the incident electric field as shown in Figure 3.1. However, if the incident electric field intensity is sufficiently large, that is comparable with internal field which binds together electrons and ions (3×10^{10} Vm^{-1}) which is equivalent to incident intensity of approximately 10^{14} W/cm^2 [43], then the electronic response will be driven into the non-linear regime described by a non-symmetric potential at higher radial distance from the nucleus. The polarisation then varies non-linearly with the applied incident electric field as shown in Figure 3.1. The electrons will undergo anharmonic oscillations, depending on the strength of anharmonicity, new waves with higher frequencies can be emitted.

A more general equation of the electric polarisation in equation 3.5 is required to account for

the non-linear response of the electron. By taking the Taylor expansion of equation 3.8, higher order terms can be included to account for the non-linearity therefore the polarisation can be written as

$$\mathbf{P} = \varepsilon_o(\chi^{(1)}.\mathbf{E} + \chi^{(2)} : \mathbf{E}\ \mathbf{E} + \chi^{(3)} \vdots \mathbf{E}\ \mathbf{E}\ \mathbf{E} + ...) \tag{3.9}$$

where $\chi^{(n)}$ is the nth-order optical susceptibility tensor [45, 46]. The first term in equation 3.9 accounts for linear effects such as reflection, refraction, diffraction, interference and single photon absorption for low intensities. The second and higher order terms are nonlinear terms and are only possible at high incident intensities and processes such as three and four wave mixing, self-focusing, self-phase modulation and multiphoton absorption can occur.

It is convenient to rewrite equation 3.9 as linear and nonlinear terms so that

$$\mathbf{P} = \mathbf{P}^{(1)} + \mathbf{P}^{NL} = \varepsilon_o(\chi^{(1)}.\mathbf{E} + \mathbf{P}^{NL}) \tag{3.10}$$

The displacement field $\mathbf{D}$ in equation 3.5 can be rewritten as

$$\mathbf{D} = \varepsilon_o\mathbf{E} + \varepsilon_o\chi^{(1)}.\mathbf{E} + \mathbf{P}^{NL} = \varepsilon_o\varepsilon^{(1)}\mathbf{E} + \mathbf{P}^{NL} \tag{3.11}$$

where $\varepsilon^{(1)} = 1 + \chi^{(1)}$ is the frequency dependent first order dielectric tensor. Using the nonlinear displacement field in equation 3.11 and substitute in equation 3.7 the following equation is obtained

$$\nabla^2\mathbf{E} - \frac{1}{c^2}\frac{\partial^2\mathbf{E}}{\partial t^2} = \mu\frac{\partial^2\mathbf{P^{NL}}}{\partial t^2} \tag{3.12}$$

This equation has the form of a driven inhomogeneous equation [44]. All optical waves are coupled by the nonlinear polarisation. The nonlinear response of the material is represented on the right side of equation 3.12 and acts as a source term for new waves. In the absence of this source term the equation has solutions of the form of free waves propagating with velocity c/n, where n is the refractive index that satisfies $n^2 = \varepsilon^{(1)}$ [44].

For the case of a dispersive medium, each frequency component of the field is considered

separately. The electric and polarisation fields can be represented as the sum of various positive frequencies

$$\mathbf{E}(z,t) = \sum_n E_n(z,t)e^{i(k_n z - \omega_n t)} + cc, \tag{3.13}$$

$$\mathbf{P}^{NL}(z,t) = \sum_n P_n^{NL}(z,t)e^{i(k_n z - \omega_n t)} + cc, \tag{3.14}$$

in which z is the propagation direction and k_n is the nth wave vector. The wave envelope varies with distance through the medium as a result of both linear and nonlinear processes [43]. Using the slowly-varying envelope approximation, which assumes that the magnitude and phase of the wave amplitude vary slowly in space and time over an optical wavelength and period along the distance z [47]. This is applicable to optical frequencies (10^{15} s^{-1}) and for pulse durations of about 100 fs

$$\frac{\partial^2}{\partial t^2}E_n \ll \omega_n \frac{\partial}{\partial t}E_n \tag{3.15}$$

$$\frac{\partial^2}{\partial z^2}E_n \ll k_n \frac{\partial}{\partial z}E_n \tag{3.16}$$

and for the complex amplitude of the Fourier component of the nonlinear polarisation

$$\frac{\partial^2}{\partial t^2}P_n^{NL} \ll \omega_n \frac{\partial}{\partial t}P_n^{NL} \ll \omega_n^2 P_n^{NL} \tag{3.17}$$

Combining equations 3.15 to 3.17 and substituting into 3.12, the nonlinear equation is linearised to

$$\left(\frac{\partial}{\partial z} + \frac{n_{\omega n}}{c}\right)E_n(z,t) = i\frac{\omega_n}{2\varepsilon_o n_{\omega n}c}P_n^{NL}(z,t)e^{-ik_n z}. \tag{3.18}$$

The equation above describes the electric field in the medium due to the induced nonlinear polarisation. The magnitude of intensities of the incident laser pulses determines the nonlinear terms which can be included in equation 3.18. For example $\chi^{(2)}$ effects or second order processes such as three wave mixing which include sum and difference frequency generation and in particular second harmonic generation can be observed. Third order processes or $\chi^{(3)}$ effects

such as frequency tripling, self-focusing, self phase modulation, and multiphoton absorption can be observed.

In the next section we give a brief theory of nonlinear processes applied in this study. These include second harmonic generation, multiphoton absorption and nonlinear refractive index.

3.2 Optical Nonlinear Effects

This study is based on nonlinear effects and in this section we give a brief overview of three nonlinear processes which are essential for this study. Firstly, the general theory of SHG including a brief overview of second order susceptibility tensor is given. Secondly, a summary of multiphoton absorption processes as one of the nonlinear process important to observe EFISH process is described. Lastly, a brief description of the optical Kerr effect in which the refractive index of a material changes in the presence of high laser intensities is given.

3.2.1 Second Harmonic Generation

Second harmonic generation is the nonlinear conversion of two photons of frequency ω to a single photon of frequency 2ω. It occurs through the second order nonlinear susceptibility tensor, $\chi^{(2)}$, in which high intensities are required to induce nonlinear effects therefore the optical response of the system results in the asymmetric charge oscillation about the equilibrium. This distribution then reradiates new frequencies such as 2ω.

According to the electric dipole approximation SHG occur in the bulk of noncentrosymmetric medium or at surfaces or interfaces of two centrosymmetric media where symmetry is broken. Only few atomic or molecular monolayers on the surface or either side of the interface participate in the symmetry breaking therefore SHG process can be used as a highly surface-selective optical probe of the interfacial phenomena [48].

Assuming a sinusoidal incident electric field given by, $E = E_o\cos(\omega.t + \phi_i)$, and using the

second term in equation 3.9, the second order non-linear polarisation takes the form

$$P^{(2)}(2\omega) = \sum_{i=x,y,z} \frac{\varepsilon_o \chi^{(2)} E_o^2}{2} \left(1 - \cos(2\omega t + \phi_i)\right), \tag{3.19}$$

in which the new frequency, 2ω, shown in equation 3.19 is generated from two photons of frequency ω. The first component which is frequency independent establishes a static electric field in the material.

The second harmonic intensity $I^{2\omega}$ that can be measured from surfaces or bulk noncentrosymmetric materials is proportional to the square of the second order nonlinear tensor, $\chi^{(2)}$, the interaction length (L) and the incident intensity (I^ω) [43, 46, 48, 49, 50, 51] so that

$$I^{2\omega} \propto \left(I^\omega L \chi^{(2)}\right)^2 \left(\frac{\sin\frac{1}{2}\Delta kL}{\frac{1}{2}\Delta kL}\right)^2 \tag{3.20}$$

where $\Delta k = k_2(2\omega) - 2k_1(\omega)$ is called the wavevector or momentum mismatch of the SH and the fundamental waves. The last factor in brackets shown in equation 3.20 is called the phase matching factor. For conditions of perfect phase matching the factor takes a maximum value of one. Figure 3.2 show the SHG conversion efficiency ($I^{2\omega}/I^\omega$) plotted using equation 3.20 against the normalized crystal length in the absence of any absorption and dispersion of the pump beam for different phase mismatching factors. For conditions of perfect phase matching ($\Delta kL = 0$) all the SH signal generated by the fundamental beam adds constructively along the crystal length and it is proportional to the square of the crystal length. For conditions of phase mismatch the fundamental beam is not well coupled to the SH signal therefore there is a small SHG conversion efficiency.

The SHG yield that can be measured from a sample is dominated by the nature of the second order nonlinear tensor ($\chi^{(2)}$) which is determined by the structure of the medium. Using a tensor is more general since the defined axes of the crystal is used to represent the directional dependence of the nonlinear response of the system. In the next section we describe the properties of second order nonlinear susceptibility tensor.
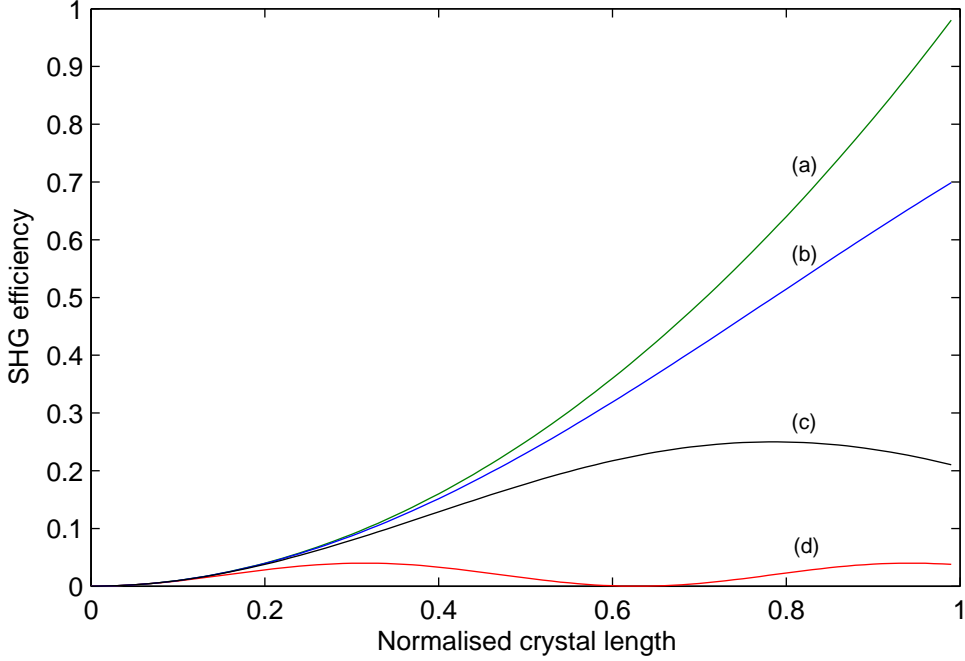
Figure 3.2: Variation of the SHG intensity along the crystal for different phase mismatch (a) $\Delta kL = 0$, (b) $\Delta kL = 1$ (c) $\Delta kL = 2$ and (d) $\Delta kL = 5$.

Second Order Susceptibility Tensor

The polarisation of the medium by an applied optical field is considered to be mainly due to displacement of bound charges. In an anisotropic medium the displacement of charges is direction dependent. The nonlinear susceptibility tensor for an anisotropic material is therefore direction dependent. In an isotropic medium the potential that describes the bonding of electrons is the same in all directions therefore the polarisation and the electric fields are related by a scalar. By taking into account the directional dependence of the second order susceptibility tensor the second term for SHG in equation 3.9 can be written as

$$P_i^{(2)} = \varepsilon_o \sum_{jk} \chi_{ijk}^{(2)} E_j E_k, \tag{3.21}$$

where i, j, k represent the Cartesian coordinates. The second order susceptibility $\chi^{(2)}$ is a third rank tensor with $3 \times 9 = 27$ real elements. The number of tensor elements are reduced by considering symmetry properties such as intrinsic and full permutation symmetries, and the

Kleinman's symmetry [46].

Intrinsic permutation symmetry can be represented as

$$\chi_{ijk}^{(2)}(\omega_n + \omega_m, \omega_n, \omega_m) = \chi_{ikj}^{(2)}(\omega_n + \omega_m, \omega_m, \omega_n), \tag{3.22}$$

the frequencies of the first field (ω_m) and second field (ω_n) can be interchanged freely without changing the properties of the tensor.

In lossless media the symmetry can be expanded to full permutation symmetry in which all the frequency arguments can be freely interchanged as long as the corresponding Cartesian indices are interchanged simultaneously,

$$\chi_{ijk}^{(2)}(\omega_n + \omega_m, \omega_n, \omega_m) = \chi_{jik}^{(2)}(\omega_n, \omega_m + \omega_n, -\omega_m). \tag{3.23}$$

Most of the nonlinear optical interactions involve optical waves with frequencies far from the lowest resonance frequency of the medium. Under these conditions the nonlinear susceptibility is independent of frequency and this is the Kleinman's symmetry. It allows permuting the directional indices without permuting the frequencies. Under Kleinman's symmetry a contracted notation is introduced $d_{ijk} = \frac{1}{2}\chi_{ijk}^{(2)}$. For SHG d_{ijk} should be symmetric in the last two indices.

The notation is simplified by introducing a contracted matrix d_{il} according to [44]

$$
\begin{array}{ccccccc}
jk: & 11 & 22 & 33 & 23, 32 & 31, 13 & 12, 21 \\
l: & 1 & 2 & 3 & 4 & 5 & 6
\end{array}
$$

The nonlinear polarisation leading to SHG can be written in terms of the d_{il} matrix and is

given by

$$
\begin{bmatrix} P_x^{(2)}(2\omega) \\ P_y^{(2)}(2\omega) \\ P_z^{(2)}(2\omega) \end{bmatrix} = 2\varepsilon_o \begin{bmatrix} d_{11} & d_{12} & d_{13} & d_{14} & d_{15} & d_{16} \\ d_{21} & d_{22} & d_{23} & d_{24} & d_{25} & d_{26} \\ d_{31} & d_{32} & d_{33} & d_{34} & d_{35} & d_{36} \end{bmatrix} \begin{bmatrix} E_x^2(\omega) \\ E_y^2(\omega) \\ E_z^2(\omega) \\ 2E_y^2(\omega)E_z^2(\omega) \\ 2E_x^2(\omega)E_z^2(\omega) \\ 2E_x^2(\omega)E_y^2(\omega) \end{bmatrix}.
$$

If the Kleinman symmetry is explicitly applied it is found that 10 of the 18 elements of d_{il} are independent entries. The d_{il} matrix represents the second order nonlinear tensor.

For Si(100) crystal face in which the SH signals are generated from the surface the above equation can be written as [52]

$$
\begin{bmatrix} P_x^{(2)}(2\omega) \\ P_y^{(2)}(2\omega) \\ P_z^{(2)}(2\omega) \end{bmatrix} = 2\varepsilon_o \begin{bmatrix} 0 & 0 & 0 & 0 & d_{15} & 0 \\ 0 & 0 & 0 & d_{15} & 0 & 0 \\ d_{31} & d_{31} & d_{33} & 0 & 0 & 0 \end{bmatrix} \begin{bmatrix} E_x^2(\omega) \\ E_y^2(\omega) \\ E_z^2(\omega) \\ 2E_y^2(\omega)E_z^2(\omega) \\ 2E_x^2(\omega)E_z^2(\omega) \\ 2E_x^2(\omega)E_y^2(\omega) \end{bmatrix}
$$

with three independent non-zero elements. The respective polarisations can be written as

$$
P_x^{(2)}(2\omega) = 4\varepsilon_o d_{15} E_x^2(\omega) E_z^2(\omega),
$$

$$
P_y^{(2)}(2\omega) = 4\varepsilon_o d_{15} E_y^2(\omega) E_z^2(\omega),
$$

and

$$
P_z^{(2)}(2\omega) = 2\varepsilon_o \left(d_{31} E_x^2(\omega) + d_{31} E_y^2(\omega) + d_{32} E_z^2(\omega) \right).
$$

For p-polarized light, incident in the yz plane, $E_x(\omega) = 0$, $E_y(\omega)$ and $E_z(\omega)$ are nonzero, the

second order polarisation that can be induced in the medium is written as

$$P_y^{(2)}(2\omega) = 4\varepsilon_o d_{15} E_y^2(\omega) E_z^2(\omega),$$

and

$$P_z^{(2)}(2\omega) = 2\varepsilon_o \left(d_{31} E_y^2(\omega) + d_{32} E_z^2(\omega) \right).$$

The generated SH beam is also p-polarized with y and z components of induced polarisation.

For s-polarized incident light in the yz plane $E_y(\omega) = E_z(\omega) = 0$ and $E_x(\omega) \neq 0$, the second order polarisation that is induced in the material is in the z direction only and is given by

$$P_z^{(2)}(2\omega) = 2\varepsilon_o d_{31} E_x^2(\omega)$$

The generated SH beam does not have s-polarisation since there is no x component of the induced polarisation.

If the SHG from the medium is detected as p-polarized then the SH intensity that can be measured in a p-p excitation and detection polarisation, $I_{pp}(2\omega)$, is given by

$$I_{pp}(2\omega) \propto |P_y^{(2)}(2\omega)\hat{y} + P_z^{(2)}(2\omega)\hat{z}|^2.$$

This implies that SHG depends on the property of the medium which is represented by the susceptibility tensor and with the polarisation of the incident laser beam. Clearly $I_{ss}(2\omega) = 0$ since the induced polarisation in the medium is only in the z-direction, only polarisations induced in the x-direction contribute to s-polarisation.

3.2.2   SHG from Interfaces of Centrosymmetric Medium

In this study SHG in reflection and transmission geometries were applied to study SHG from Si/SiO$_2$ interfaces of Si membrane. This section provides a phenomenological description of SHG from surfaces of centrosymmetric media for reflection and transmission geometries as proposed by Sipe [53] and later derived by Mizrahi and Sipe [54]. The model for SHG

in reflection was successfully applied by Lupke [9] to represent surface SHG from Si/SiO$_2$ interfaces. The summary for the two models for SHG in reflection and transmission derived in this section is based on literature from [9, 53, 54].

Figure 3.3 shows the experimental geometries used to derive the expressions for surface SH power generated in reflection and transmission. The first interface in Figure 3.3(a) contributes to SHG in reflection. Medium 1 can be air, vacuum or any dielectric material with complex dielectric constant ϵ_1, medium 2 is treated as a thick slab of centrosymmetric material such as silicon with complex dielectric constant ϵ_2 and a polarisation sheet located at z = ξ just above z=0. The dielectric tensors $\epsilon_1(\omega)$, $\epsilon_1(2\omega)$ and $\epsilon_2(\omega)$ are presumed real therefore there is no absorption of the fundamental and SH wave in medium one and two. Medium two is treated as a thick slab therefore multiple reflections of the incident beam are neglected.

Figure 3.4 shows the coordinate system used throughout the derivation for an upward and downward propagating beams in medium one and two. The plus sign represent an upward propagating wave and the minus sign is for a downward propagating beam. According to Lupke [9] the wave vectors $\mathbf{k}_i$, $\mathbf{k}_r$ and $\mathbf{k}_t$ for the incident, reflected and transmitted fundamental radiation and $\mathbf{K}_r$ and $\mathbf{K}_t$ for the reflected and transmitted SH radiation respectively can be expressed as

$$\mathbf{k}_i = p\hat{x} - q_1\hat{z}, \mathbf{k}_r = p\hat{x} + q_1\hat{z}, \mathbf{k}_t = p\hat{x} - q_2\hat{z}, \mathbf{K}_r = P\hat{x} + Q_1\hat{z}, \mathbf{K}_t = P\hat{x} - Q_2\hat{z}.$$

Here $q_i = [k_i^2 - p^2]^{1/2}$ and $Q_i = [K_i^2 - P^2]^{1/2}$ are the positive z-components of the wave vectors in medium $i = 1, 2$. In the following, t_{12}^s and t_{12}^p denotes the Fresnel coefficients for transmission from medium one to medium two for s and p-polarised light, r_{12}^s and r_{12}^p corresponds to reflection coefficients. Capital letters will refer to second harmonic wave for example T_{21}^s is the Fresnel coefficient of second harmonic light from medium 2 to medium 1 for s-polarised wave [9]. The Fresnel coefficients for fundamental and SH light are provided in [9, 54].

Firstly we derive the SH power in reflection geometry using Figure 3.3(a). The SH signal originates from a polarisation sheet located at $z = \xi$ shown in Figure 3.3(a) and we consider
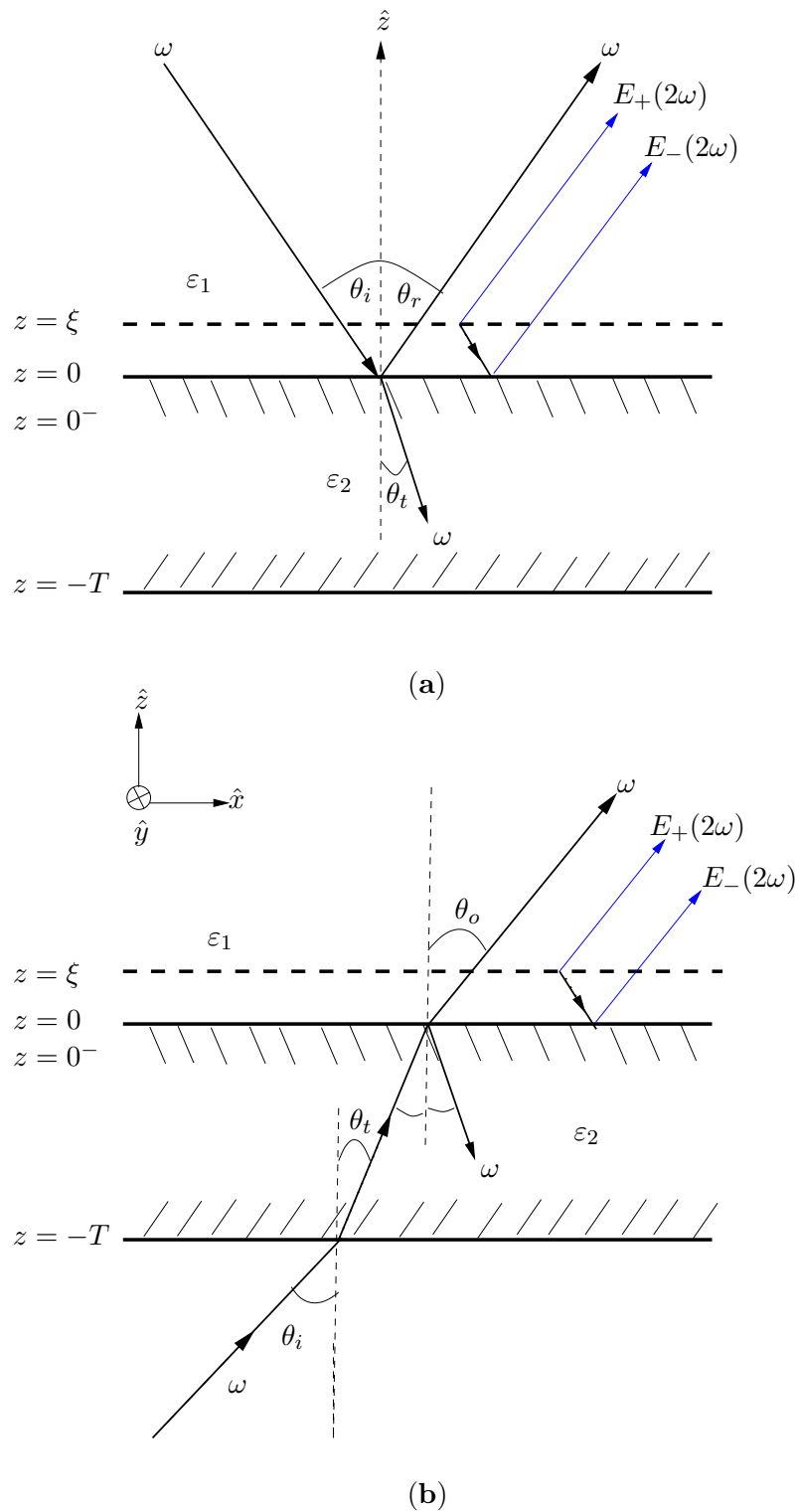
Figure 3.3: The two experimental geometries considered in this study. (a) The standard reflection geometry with the first surface nonlinear active. (b) Transmission geometry with the second surface nonlinear active.
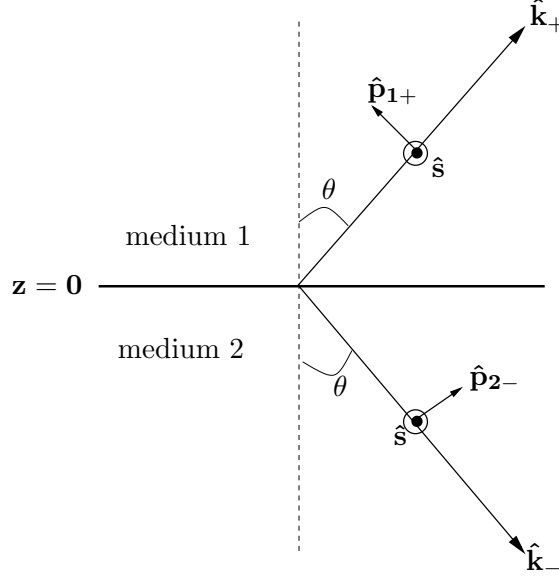
Figure 3.4: The coordinate system used to describe the polarisation directions used in the derivation of the model.

the contribution of the fundamental field at $z = 0^-$, just below $z = 0$. The induced polarisation in the medium is given by

$$\mathbf{P}(\mathbf{r}) = \mathbf{P}(z)\exp(i\kappa.\mathbf{R}) \qquad (3.24)$$

with spatial variation characterised by wave vector κ and $\mathbf{R} = (x, y)$ [9]. We can define the effective second order surface dipole polarisation as

$$\mathbf{P}^{2\omega}(\mathbf{r}) = \chi_s^{(2)} : \mathbf{E}^\omega(\mathbf{r})\mathbf{E}^\omega(\mathbf{r})\delta(z - \xi), \qquad (3.25)$$

where $\chi_s^{(2)}$ is the surface second order susceptibility tensor and $\mathbf{E}^\omega$ is the electric field vector for the fundamental beam and $\delta(z - \xi)$ denotes that the SH polarization is induced in a very small region close to the interface.

The fundamental field incident from medium 1 is given by [9, 54]

$$\mathbf{E}_i^\omega(\mathbf{r}) = (E_i^s\hat{s} + E_i^p\hat{p}_{1-})\exp[i(px - q_1 z)]. \qquad (3.26)$$

The transmitted fundamental field in medium 2 is

$$\mathbf{E}_t^\omega(\mathbf{r}) = (E_i^s t_{12}^s \hat{s} + E_i^p t_{12}^p \hat{p}_{2-})\exp[i(px - q_2 z)], \tag{3.27}$$

where the Fresnel coefficient factors for s- and p-polarised fundamental beam are included and allow the change in direction of the wave. The minus sign for p-polarised light denotes the direction for downward propagating wave and plus sign is for upward propagating wave consistent with notation in Figure 3.4 [54]. The linear field in medium 2 close to $z = 0$ is given by

$$\mathbf{E}^\omega(x, z = 0^-) = (E_i^s t_{12}^s \hat{s} + E_i^p t_{12}^p \hat{p}_{2-})\exp(ipx) = \mathbf{e}_r^\omega |E_i|\exp(ipx), \tag{3.28}$$

with $|E_i|^2 = |E_i^s|^2 + |E_i^p|^2$ and $\mathbf{e}_r^\omega = [\hat{s}t_{12}^s \hat{s} + \hat{p}_{2-}t_{12}^p \hat{p}_{1-}].\hat{e}^{in}$. The unit vector $\hat{e}^{in}$ represent the chosen polarisation of the incident light.

Putting this expression into equation 3.25

$$\mathbf{P}^{2\omega}(\mathbf{r}) = \chi_s^{(2)}\mathbf{e}_r^\omega \mathbf{e}_r^\omega |E_i|^2\exp(i2px)\delta(z - \xi) = \wp\delta(z - \xi)\exp(i2px) \tag{3.29}$$

To calculate the upward-propagating second harmonic field that is generated by the nonlinear polarisation sheet two contributions are considered. First there is the directly generated upward propagating wave at $z = \xi$ and is indicated as $E_+(2\omega)$ in Figure 3.3(a). Second, contribution by part of the downward-propagating wave that is reflected upward at the interface $z = 0$ and is indicated by $E_-(2\omega)$. Combining the two contributions for the SH generated field in reflection, we have

$$\mathbf{E}^{2\omega}(\mathbf{r}, t) = \mathbf{E}^{2\omega}(\mathbf{r})\exp(-i2\omega t) + c.c., \tag{3.30}$$

where

$$\mathbf{E}^{2\omega}(\mathbf{r}) = \frac{2\pi i K_1^2}{Q_1}\mathbf{H}^o.\wp \, \exp[i(Px + Q_1 z)], \tag{3.31}$$

with

$$\mathbf{H}^o \equiv [\hat{S}(1 + R_{12}^s)\hat{S} + \hat{P}_{1+}(\hat{P}_{1+} + R_{12}^p)\hat{P}_{1-})] \tag{3.32}$$

The $\hat{S}\hat{S}$ and $\hat{P}_{1+}\hat{P}_{1+}$ in equation 3.32 are the directly generated upward waves at $z = \xi$ contributing to $E_+(2\omega)$. The other terms with a Fresnel reflection coefficient (R_{12}) as the

scaling factor are generated by the downward propagating wave that is reflected at the interface $(z = 0)$ and these contribute to $E_-(2\omega)$.

If we let the polarisation component of the SH beam that we choose to detect in reflection to be denoted by $\hat{e}^{out}$, we can write $\mathbf{e}^{2\omega} = \hat{e}^{out}.\mathbf{H}^o$. If medium 1 is dispersionless, $\theta_i = \theta_r$, where θ_i is the angle between the wave vector of the incident fundamental wave and the surface normal. Using $K_1^2 = 4\omega^2/c^2$ and the dispersionless condition, by defining $P(\omega)$ as the power incident through an area A, and $P_R(2\omega)$ as the corresponding SH power generated in reflection, we obtain [9],

$$P_R(2\omega) = \frac{32\pi^3\omega^2}{c^3 A}\sec^2\theta_i|\mathbf{e}_r^{2\omega}.\chi_s^{(2)} : \mathbf{e}_r^{\omega}\mathbf{e}_r^{\omega}|^2 P^2(\omega) \tag{3.33}$$

since $\theta_i = \theta_r$, and thus A is also the area normal to the Poynting vector of the SH beam.

Now we derive the corresponding expression for the SH power generated in transmission. Figure 3.3(b) shows the experimental geometry used to derive the SHG in transmission as reported by Mizrahi and Sipe [54]. There is no absorption of the incident fundamental beam and the SH signal is generated at the second interface with a polarization sheet at $z = \xi$. The blue lines indicate the SH fields which contributes to SH signal in transmission. The fundamental field that generates the SH polarisation is the field incident on the second interface plus the field reflected back from interface two into medium 2 (ω field at $z = 0^-$). No multiple reflections of the fundamental beam are considered. The linear field at $z = 0^-$ which lies in medium 2 is given by

$$\begin{aligned}\mathbf{E}^\omega(x, z = 0^-) &= [\hat{s}t_{12}^s(1 - r_{21}^s)E_{in}^s + (\hat{p}_{2+} - r_{21}^p\hat{p}_{2-})t_{12}^p E_{in}^p]\exp(ipx) \tag{3.34}\\ &= \mathbf{e}_t^\omega|E_{in}|\exp(ipx)\end{aligned}$$

where

$$\mathbf{e}_t^\omega = [\hat{s}t_{12}^s(1 - r_{21}^s)\hat{s} + (\hat{p}_{2+} - r_{21}^p\hat{p}_{2-})t_{12}^p\hat{p}_{1+}].\hat{e}^{in}$$

The vector $\mathbf{e}_t^\omega$ is the sum of the incident and reflected electric field vectors that is transmitted to interface two.

The second harmonic field radiated upward at 2ω in Figure 3.3(b) is given by

$$\mathbf{E}^{2\omega}(\mathbf{r}) = \frac{2\pi i K_1^2}{Q_1}\mathbf{H}^o.\wp \, \exp[i(Px + Q_1 z)], \qquad (3.35)$$

Here $\mathbf{H}^o$ is the same as in equation 3.32, and selecting the polarization $\hat{e}^{out}$, we have

$$
\begin{aligned}
\mathbf{E}^{2\omega}(\mathbf{r}) &= \frac{2\pi i K_1^2}{Q_1}\hat{e}^{out}.\mathbf{H}^o.\wp \, \exp[i(Px + Q_1 z)] \\
&= \frac{2\pi i K_1^2}{Q_1}\mathbf{e}_t^{2\omega}.\wp \, \exp[i(Px + Q_1 z)]
\end{aligned}
\qquad (3.36)
$$

Following the derivation of equation 3.33 the SH power generated in transmission is given by

$$P_T(2\omega) = \frac{32\pi^3\omega^2}{c^3 A}\sec^2\theta_i |\mathbf{e}_t^{2\omega}.\chi_s^{(2)} : \mathbf{e}_t^\omega \mathbf{e}_t^\omega|^2 P^2(\omega). \qquad (3.37)$$

The two equations 3.33 and 3.37 represent the SH power that can be measured in reflection and transmission respectively from surfaces of centrosymmetric media. The vectors $\mathbf{e}_r^{2\omega}$ and $\mathbf{e}_t^{2\omega}$ are the same but $\mathbf{e}_r^\omega$ and $\mathbf{e}_t^\omega$ are different.

3.2.3 Multiphoton Absorption

In this study samples are probed by high intensities in order to observe a measurable EFISH signal from the Si/SiO$_2$ interfaces. The optical properties of silicon can change drastically under intense laser irradiation therefore equations for low intensity irradiation cannot fully describe the transmittance and absorbance of light in silicon. Under intense fs laser irradiation (> 1 GW/cm^2), the probability of a material absorbing more than one photon before relaxing to ground state can be greatly enhanced [47]. If multiphoton absorption at high intensities in silicon is strong, the transmitted fundamental beam can be depleted in the Si leading to low beam transmission.

During multiphoton absorption electron-hole pairs in silicon are generated by the absorption of two or more photons, the probability of an electron to absorb at least two photons is increased at high intensities. In silicon multiphoton absorption such as two or three photon

absorption is strong in the mid- or far-infrared wavelength regions where two or three photons are simultaneously absorbed through virtual intermediate states in the indirect energy gap of 1.1 eV [55]. Multiphoton absorption can be greatly enhanced by the presence of intermediate resonances. At a fundamental wavelength of 800 nm (1.55 eV) three photon absorption can occur through resonance two photon absorption via the silicon direct bandgap of 3.1 eV.

The change in the nonlinear absorption coefficient is related to the imaginary part of the effective third order susceptibility tensor $\chi^{(3)}$. The functional form of $\chi^{(3)}$ depends on the symmetry and orientation of the crystal [56, 57]. Single photon, two, three and four photon absorption are proportional to the magnitude of the imaginary part of first, third, fifth and seventh order susceptibility tensors respectively. Since $\chi^{(n+2)} \lll \chi^{(n)}$, higher order multiphoton absorption coefficients are small to measure therefore high intensities are required to observe any transmission change.

The attenuation of the laser beam caused by two photon absorption can be represented by the differential equation [46, 58]

$$\frac{dI}{dz} = -\alpha I - \beta I^2 \tag{3.38}$$

where α is the linear absorption coefficient and β is the two photon absorption coefficient.

For a three photon absorption process, the intensity attenuation is given by

$$\frac{dI}{dz} = -\alpha I - \gamma I^3 \tag{3.39}$$

where γ is the three photon absorption coefficient.

The solution to equation 3.38 is given by

$$I(z) = \frac{\alpha I_o e^{-\alpha z}}{\alpha + \beta(1 - e^{-\alpha z})I_o}, \tag{3.40}$$

in the limit that β goes to zero equation 3.40 reduces to Beer-Lambert's law [58] of single photon absorption.

In more general cases if the nonlinear effects include higher order multiphoton absorption

processes equations 3.38 and 3.39 can be generalised to

$$\frac{dI}{dz} = -\alpha I - \beta I^2 - \gamma I^3 - \tau I^4 - ... \tag{3.41}$$

in which τ is the four photon absorption coefficient.

The investigation of multiphoton absorption in particular two photon absorption at different wavelengths for different materials has been reported in literature using the common z-scan technique [59, 60, 61, 62, 63, 64, 65, 66, 67]. Z-scan has been widely adopted as a simple single beam technique to obtain β and n_2 (nonlinear refractive index) with intensity variation achieved by scanning a sample through the focal region of a Gaussian beam [61]. The z-scan method provides a sensitive and straight-forward method for the determination of the sign and the values of the real and imaginary parts of $\chi^{(3)}$. The simplicity of both the experimental setup and the data analysis has allowed the z-scan method to become widely used by many research groups [68]. Measurements of β and n_2 are performed using the closed and open aperture z-scan technique respectively.

The incident laser is focussed on the sample and measure the transmitted light as the sample is scanned through the laser focus in the z-direction in an open aperture z-scan technique. According to Dinu et al. [69], for a Gaussian beam the transmitted light for open aperture technique, is given by

$$T_{\text{open}}(z) = 1 - \frac{1}{2\sqrt{2}} \frac{\beta I_o L_{\text{eff}}}{1 + (z/z_o)^2}, \tag{3.42}$$

where z is the longitudinal scan distance from the focal point with an on-axis intensity of I_o (inside the sample) and z_o is the confocal beam parameter; $L_{\text{eff}} = \alpha^{-1}(1 - e^{-\alpha L})$ is the effective optical path length, α is the linear absorption coefficient and L is the sample thickness.

In a closed aperture z-scan a circular aperture with transmissivity $S < 1$ is placed behind the sample, and the transmission is recorded as a function of z position of the sample. The measured transmitted intensity is sensitive to small changes caused by nonlinear effects on the sample such as self focusing and self defocussing [70]. For small absorptive and refractive
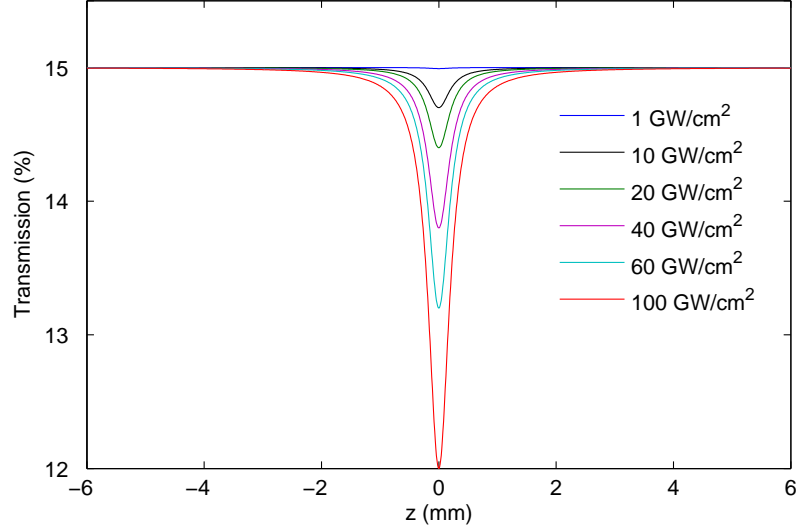
Figure 3.5: The plot of change in transmitted light as the Si membrane is scanned through the focus for different peak intensities in a typical open aperture z-scan experiment. The plots are according to equation 3.42.

changes the transmissivity is given by [68, 69]

$$T_{\text{closed}}(z) = 1 - \frac{8\pi}{\lambda\sqrt{2}} \frac{z/z_o(1-S)^{0.25} L_{\text{eff}} n_2 I_o}{(1+(z/z_o)^2)(9+(z/z_o)^2)} - \frac{1}{2\sqrt{2}} \frac{L_{\text{eff}} \beta I_o (3-(z/z_o)^2)}{(1+(z/z_o)^2)(9+(z/z_o)^2)}. \quad (3.43)$$

Figure 3.5 shows a plot of equation 3.42 at different peak incident intensities using typical parameters such as thickness and linear absorption coefficient of the Si membrane used in this study. The two photon absorption (β) coefficient was assumed constant at different peak intensities based on the value obtained from [70] at 800 nm. The simulation shows that the transmitted signal changes as the sample is scanned through the focus. The highest incident intensity on the sample correspond to $z = 0$ in which a minimum in transmission change is well pronounced. At this value of z there is high intensity at focus and the probability of absorbing two or more photons is enhanced. More incident light is absorbed leading to less light being transmitted by the sample. Far from $z = 0$, all graphs show the same transmission value independent of peak incident intensities. In this case the sample is far from focus and no multiphoton absorption occur therefore single photon absorption process dominates in this low intensity regime.

3.2.4   Nonlinear Refractive Index

In addition to multiphoton absorption at high intensities, the refractive index n of the material will start to depend on the incident intensity (I) according to the relationship $n = n_o + n_2 I$, where n_o is the linear refractive index of the material and n_2 is the nonlinear index of refraction [46, 59, 60, 68, 71]. The intensity dependent refractive index is the basic mechanism for many nonlinear effects [46], such as self-focusing, optical switching, self-phase modulation, spatial and temporal solitons [72, 73]. The intensity-dependent refractive index n_2 is related to the real part of the third order susceptibility tensor $\chi^{(3)}$ for centrosymmetric media such as silicon.

The total polarisation in a medium in which the nonlinear refractive index can be observed is given by

$$\mathbf{P} = \epsilon_{\mathbf{o}}(\chi^{(\mathbf{1})}.\mathbf{E} + \chi^{(\mathbf{3})}\vdots\mathbf{EEE}), \tag{3.44}$$

substituting equation 3.44 into equation 3.5, the dielectric displacement can be written as

$$\mathbf{D} = \epsilon_o[(1 + \chi^{(1)}) + \chi^{(3)}|\mathbf{E}|^{\mathbf{2}}]\mathbf{E} \tag{3.45}$$

$$= \epsilon_o\epsilon_r.\mathbf{E} \tag{3.46}$$

where $\epsilon_r = \left(1 + \chi^{(1)} + \chi^{(3)}|\mathbf{E}|^{\mathbf{2}}\right)$ is the relative dielectric permittivity of the material.

The refractive index is related to the dielectric permittivity through

$$n = \sqrt{\mathrm{Re}(\epsilon_r)}. \tag{3.47}$$

The changes to the refractive index caused by high intensities is much smaller than linear refractive index therefore

$$n = n_o + \frac{1}{2n_o}\mathrm{Re}\{\chi^{(3)}\}|\mathbf{E}|^{\mathbf{2}} \tag{3.48}$$

$$= n_o + n_2 I \tag{3.49}$$

where $n_o = \left(1 + \mathrm{Re}\{\chi^{(1)}\}\right)^{1/2}$, and $\mathbf{P}$, $\mathbf{E}$, n are frequency dependent terms. Equation 3.49

shows that the refractive index changes with the square of the applied electric field and this is called Kerr effect. In most nonresonant cases, the induced refractive index change is very small ($\leq 10^{-4} \sim 10^{-5}$) [46].

3.3   Electric Field Induced Second Harmonic Generation

SHG is symmetry forbidden in the bulk of cubic centrosymmetric or isotropic medium such as silicon within the electric dipole approximation. In the presence of electric fields the symmetry of crystals can be broken and SHG is enhanced as the bulk crystal become a source of SH signal [74]. There are three possible sources of electric fields in crystals. An electric field can be intrinsic to the system under investigation for example at the interface between two heterojunction semiconductors. The different band energies of the two materials create a depletion region at the interface which has intrinsic electric field. The intrinsic electric field is time independent. An electric field can be artificially induced in a crystal by applying external bias which can be varied and this can be used in the study of many semiconductor device structures. An electric field can be photoinduced in a crystal, at an interface or the surface by irradiating the material with laser pulses and free charges are generated in the material and a charge separation occurs. The separation of charges establish a quasi-static electric field.

The presence of an electric field allow SHG through a third order process called Electric Field Induced Second Harmonic (EFISH) generation. The third order nonlinear susceptibility $\chi^{(3)}$ is usually small therefore large external voltages and peak laser intensities are required to make EFISH observable [35]. In this study the EFISH generation reported is mainly from photoinduced electric fields established at the Si/SiO_2 interfaces and since this is not externally controlled it can be used as a sensitive technique of studying charge dynamics across the interface. The electric field induced by charge transfer can be large since the charge separation occur within few atomic layers and this provides a measurable SH signal.

In the absence of electric fields, the SH response from silicon arises from the surface of the crystal where symmetry is broken and higher order bulk quadrupole contributions to the nonlinear

polarisations and these are expressed as

$$\mathbf{P}_{NL}(2\omega) = \chi^{(2),SD}(2\omega;\omega,\omega) : \mathbf{E}(\omega)\mathbf{E}(\omega) + \chi^{(2),BQ}(2\omega;\omega,\omega) : \mathbf{E}(\omega)\mathbf{E}(\omega)i\mathbf{k}, \qquad (3.50)$$

where the surface dipole (SD) and the bulk quadrupole (BQ) nonlinear polarisations are given by the third- and fourth-rank tensor nonlinear susceptibilities which are $\chi^{(2),SD}$ and $\chi^{(2),BQ}$ respectively. $\mathbf{E}(\omega)$ and $\mathbf{k}$ are the amplitude and the wave vector of the pump radiation respectively [34, 74].

Another contribution of nonlinear polarisation on Si/SiO_2 interface originates from photoinduced interfacial electric field $E(\omega \approx 0)$ due to charge transfer from Si to SiO_2 upon irradiating the sample with intense laser pulses. The induced electric field allows an interfacial electric dipole contribution through a third order process given by [34]

$$\mathbf{P}^{BE}(2\omega) = \chi^{(3)}(2\omega;\omega,\omega,0) \vdots \mathbf{E}(\omega)\mathbf{E}(\omega)\mathbf{E}(\omega \approx 0). \qquad (3.51)$$

The total SHG intensity that can be measured as a result of the three different surface polarisations in reflection can be expressed as

$$I^{2\omega} \propto \left|(\mathbf{P}^{SD} + \mathbf{P}^{BQ} + \mathbf{P}^{BE})\right|^2. \qquad (3.52)$$

In general, the nonlinear polarisation vectors $\mathbf{P}^{SD}$, $\mathbf{P}^{BQ}$ and $\mathbf{P}^{BE}$ will give rise to interference effects because of their complex nature, and the cross terms depends on the phase shift between them [34]. When Si/SiO_2 interface is irradiated with sufficiently intense laser light electrons are excited from silicon valence band into the oxide conduction band and eventually trapped, a charge separation occurs. The charge separation alters the interfacial electric field at the interface and this leads to a time dependent interfacial electric field $E(t)$ giving rise to a time dependent EFISH signal. The time dependent EFISH signal from the Si/SiO_2 interface can
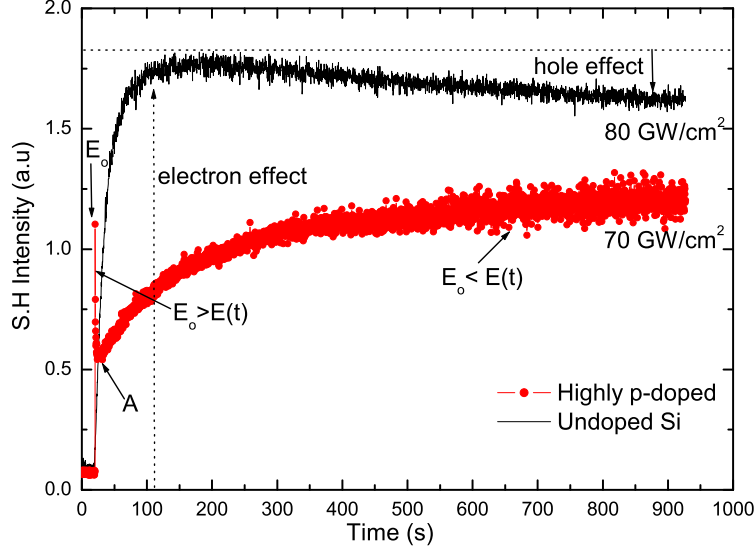
Figure 3.6: Typical temporal evolution of the EFISH signal measured in reflection for both bulk undoped and highly p-doped (< 0.01 Ωcm) Si(100) samples with native oxide as reproduced in our laboratory.

be described in general by [3, 75]

$$I^{2\omega}(t) = \left| \chi^{(2)} + \chi^{(3)} E(t) \right|^2 (I^\omega)^2 \tag{3.53}$$

$$= \left| \chi^{(2)}_{eff}(t) \right|^2 (I^\omega)^2, \tag{3.54}$$

where $\chi^{(2)}_{eff}(t) = \chi^{(2)} + \chi^{(3)}.\mathbf{E(t)}$ is the time dependent effective susceptibility tensor of the interface, I^ω and $I^{2\omega}$ are the intensities of the fundamental beam and EFISH signal respectively, $\chi^{(3)}$ is the third-order nonlinear susceptibility of silicon that governs the electric-field driven bulk dipole response, $\chi^{(2)}$ is the effective second order nonlinear susceptibility arising from other sources such as the surface and bulk quadrupole contributions, and $E(t)$ is the photoinduced interfacial electric field which arises from charge separation at the interface causing an electric field perpendicular to the sample surface [3, 9, 76]. Generally, contributions from the interfacial electric field due to charge transfer process dominates in EFISH measurements compared to $\chi^{(2)}$ processes.

Figure 3.6 show typical time dependent EFISH signals reproduced in our laboratory for bulk undoped and highly p-doped Si(100) with native oxide. The temporal evolution of the EFISH signal from the two samples increases upon irradiation showing different temporal behaviour at later times. The initial fast rise in the EFISH signals is associated with electron transfer from silicon to the oxide where some of the electrons are trapped. The trapped electrons establishes an electric field across the interface and its magnitude increases with irradiation time as more charges are trapped. The induced electric field enhances the SHG signal. The decline in the signal is due to hole transfer as indicated in Figure 3.6 for undoped sample and this establishes an opposing interfacial electric field to the one established by electrons therefore the effective electric field at the interface decreases with time and the SH signal also decreases. The initial EFISH signal in highly doped samples is due to a dc intrinsic electric field (E_o) at the interface caused by the doping effect. The initial decline is caused by electron transfer and the minimum marked by A corresponds to intrinsic and the photoinduced interfacial electric fields having the same magnitude, and therefore a switch in the direction of the net electric field. After the minimum both holes and electrons contribute to the EFISH trace shown in Figure 3.6.

Chapter 4

Experimental Setup and Methods

In the following chapter a brief summary of the commercial laser system used in this work is given. The relevant laser parameters are listed and a background free autocorrelator which was used to measure pulse duration of fs laser pulses is described. A description of two main experiments designed and implemented in this study is given. These experiments are SHG in transmission and pump-probe reflectivity measurements. A detailed report on the preparation and characterization of samples used in this study is outlined including the relevant properties of the samples used.

4.1 The Femtosecond Laser System

4.1.1 Laser Design

Figure 4.1 shows the layout of the optical components and beam path for the Ti:Sapphire oscillator (Spectra Physics, 3941-M3S, Tsunami) of the fs laser used in this work. The pump beam from a frequency doubled Nd:YVO$_4$ laser (Spectra Physics, Millenia V) with 5.5 W continuous wave maximum power output at a wavelength of 532 nm enters through the input Brewster window and guided by the mirrors P$_1$ and P$_2$ into the active medium, a Ti:Sapphire rod [77]. M$_2$ and M$_3$, are curved dichroic mirrors which are highly transmittive for the pump
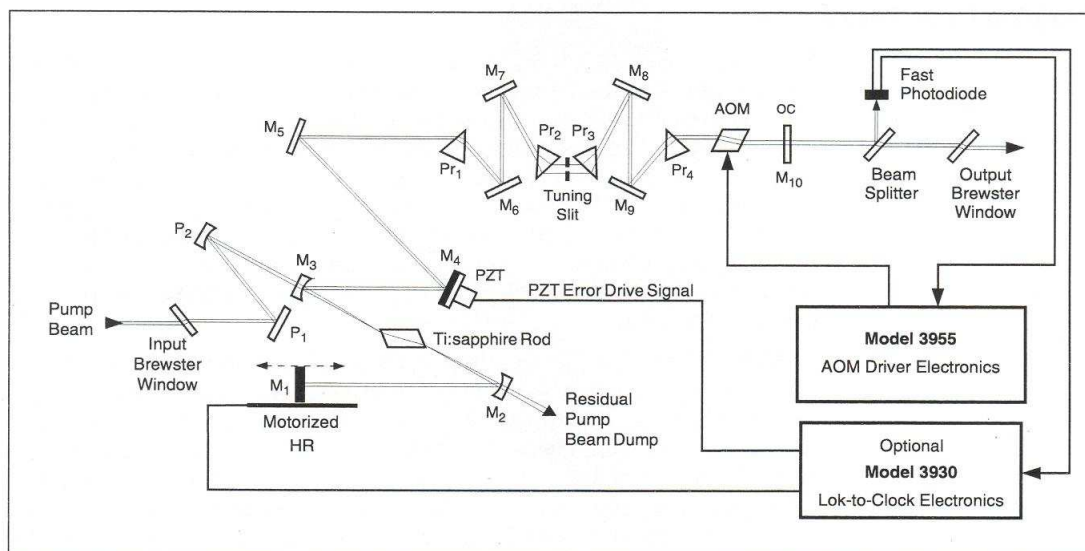
Figure 4.1: A typical layout of Tsunami model 3941-M3S fs laser showing optical components and the beam path.

beam and highly reflective for the laser frequency [77]. Extra pump beam which is not absorbed in the crystal is dumped behind mirror M_2. M_1 is a highly reflective mirror at the Ti:Sapphire wavelength and forms one end of the oscillator cavity. The prisms Pr_1 to Pr_4 form a prism set used to compensate for positive group velocity dispersion. A tuning slit is used for wavelength tuning. The laser output exits the cavity through mirror M_{10} which forms the output coupler (OC). Part of the output beam after OC is channelled to a photodiode detector connected to an acousto-optical modulator (AOM) which is electronically controlled to start and stabilize modelocking. The electronics (model 3930) is for adjusting the oscillator cavity length thereby changing the repetition rate of the emitted laser pulses. It is optional and is not available in our setup. Mirrors M_4 to M_9 are highly reflective at the Ti:Sapphire wavelength and form part of a folded cavity to increase cavity length while fitting all optical components of the laser in a small housing.

4.1.2 Laser Parameters

Some of the laser parameters which are important include the pulse duration, repetition rate, average output power and output spectrum. The pulse duration, repetition rate and output power of the Ti:Sapphire laser are used to calculate the maximum peak intensities incident on the samples.

The pulse duration of the fs laser is much shorter than the response time of modern electronic detectors therefore it is impossible to measure the pulse duration directly. An autocorrelation technique is used as an indirect method which use the same pulses to measure the pulse length. Figure 4.2 shows the experimental set up for the background free intensity autocorrelator used to measure the pulse duration of the fs laser. A beam splitter is used to split an incoming pulse
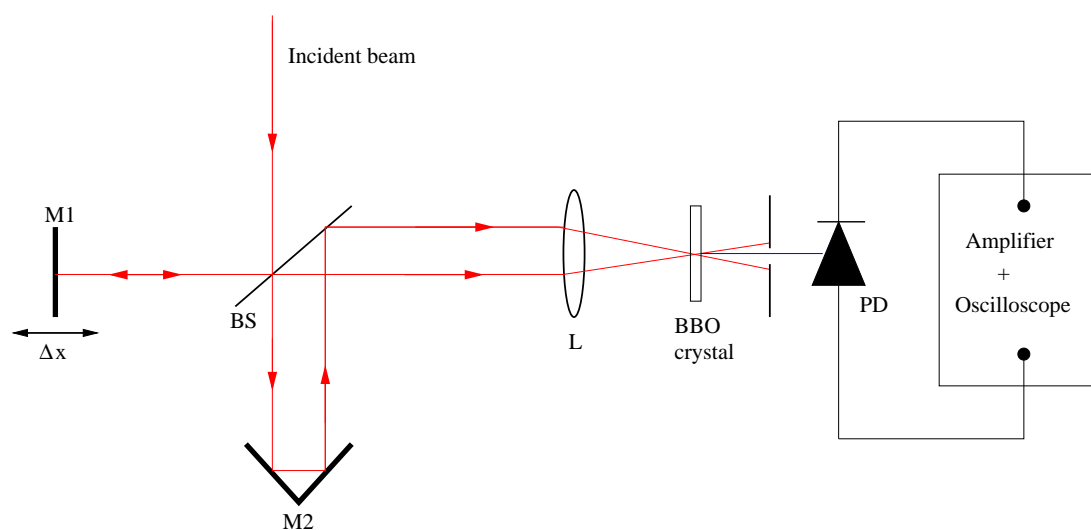
Figure 4.2: The experimental configuration for the background free autocorrelator used to measure the pulse duration of the fs laser. M1: movable mirror, M2: two gold coated mirrors at 45° to each other, BS: beam splitter, L: focusing lens, PD: AlGaAs photodiode.

into two replica which are focussed into a nonlinear medium in this case a BBO crystal. Only the SH light generated from the two overlapping pulses propagates in the forward direction is measured without incident background by the photodiode as shown in Figure 4.2. The temporal overlap between the pulses is achieved by adjusting the optical path length between the two pulses mechanically via the variable delay line shown by movable mirror M1 at a typical speed of 5 μm/s. If the delay time is made small the pulses combine in the nonlinear

crystal and the generated SH signal measured by the photodiode is maximum. If the relative time delay is increased, the mixing product becomes weaker and the signal on the photodiode decreases. The intensity dependence of the autocorrelation signal on the temporal delay is
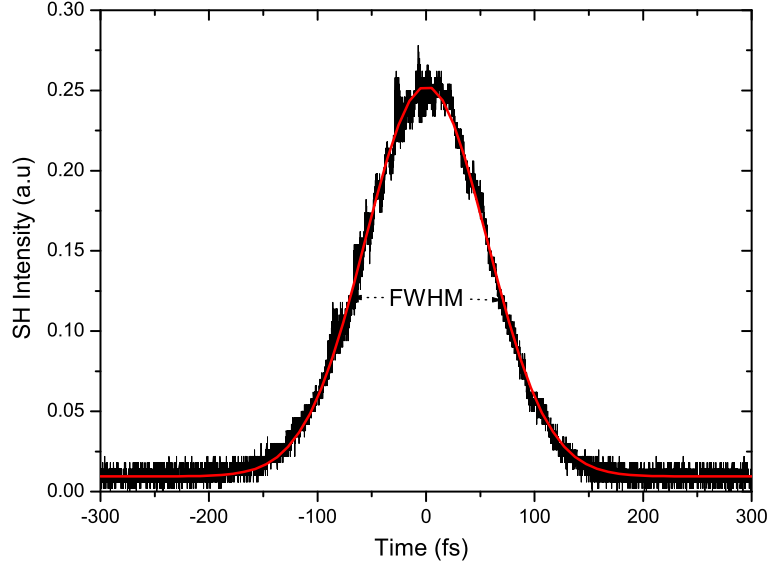
Figure 4.3: The background free autocorrelation trace obtained after moving mirror M1, solid line is data fitting according to a Gaussian pulse.

given by

$$I_{ac}(\tau) = \int_{-\infty}^{\infty} I(t)I(t+\tau)dt. \tag{4.1}$$

Unlike in interferometric autocorrelators the signal measured by the photodetector vanishes for long time delays.

The temporal pulse width is described in terms of the full width at half maximum (FWHM) of the intensity envelope. The intensity is proportional to the square of the electric field, and the temporal pulse width at FWHM, τ_p, is related to the electric field pulse width τ by

$$\tau_p = \sqrt{\ln 2}.\tau. \tag{4.2}$$

The measured autocorrelation trace is shown in Figure 4.3. The pulse width of the trace in Figure 4.3 is much larger than the value listed in Table 4.1, which can be due to pulse

Table 4.1: Summary of the laser parameters for the laser system used in this study.

Maximum average power	P_{av}	840 mW
Repetition rate	f_{rep}	80 MHz
Maximum pulse energy	E_p	10 nJ
Minimum pulse duration	τ_p	75 ± 5 fs
Maximum pulse power	P_{max}	130 kW
Center wavelength	λ	800 nm
Spectral width	$\delta\lambda$	(12.4 ± 0.5)nm
Time-bandwidth product	$\tau_p.\delta\nu$	0.44 ± 0.04
Maximum pump power	P_{pump}	5.5 W
Pump wavelength	λ_{pump}	532 nm
Polarisation		vertical
Radial mode		$\approx \mathrm{TEM}_{00}$

broadening caused by the optical components outside the laser system.
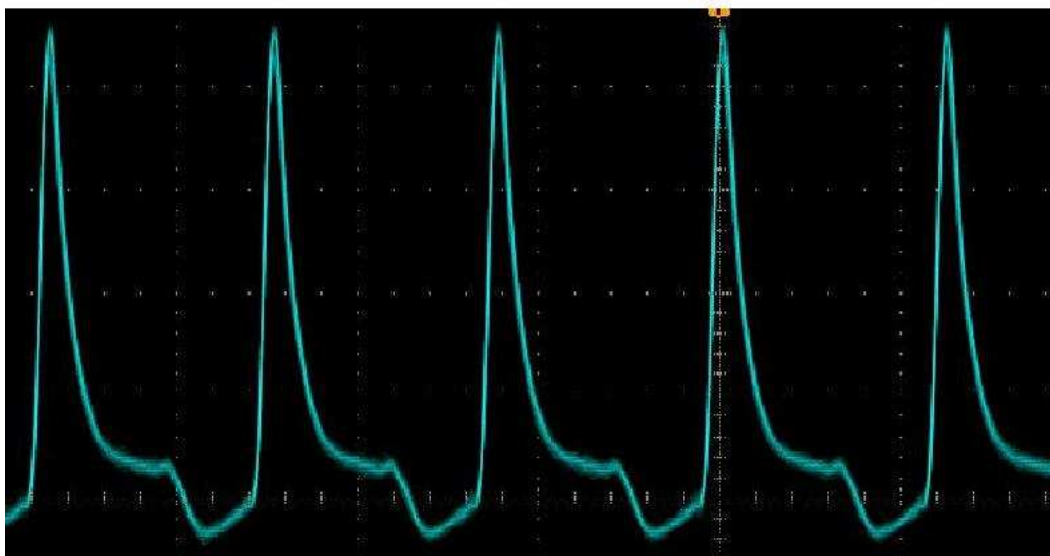
Figure 4.4: The pulse train of a fs laser as observed from oscilloscope screen. The time base was set at 10 ns per division.

The pulse repetition rate was measured with a simple pulse train detector connected to an oscilloscope (Tektronix DP002012) and the results are shown in Figure 4.4. The period of the pulses was found to be $\sim$ 12.5 ns which translates to 80 MHz repetition rate. The output spectrum of the fs laser was measured by an Ocean optics spectrometer (HR400) with a CCD

array detector equipped with Ocean Optics software which provides a readout on the computer. The spectrum is displayed on the computer screen to regularly check laser stability throughout the experiment when operating in modelocked regime. When the laser is out of modelocking the spectrum suddenly changes from the usual wide spectrum to a very narrow unstable spectrum. The average output power of the laser was measured by a power meter (Coherent field master 33-0506-000) with detector sensor (LM-3). Table 4.1 shows all laser parameters, most of the parameters were characterised in our laboratory by previous researchers [77, 78].

4.2   Experimental Setup for SHG Measurements

Figure 4.5 shows the experimental setup for SHG measurements. The output from the Ti:Sapphire oscillator tuned to 800 nm output wavelength passes through the $\lambda/2$-retarder plate (B. Halle Nachfl. GmbH, Berlin, Germany) after being guided by two gold mirrors (Edmund Optics, USA, protective coating, 1/4 wave surface accuracy at 632,8 nm). The retarder plate is used to vary the incident average power of the laser. The first polarizer (Halbo Optics, Chelmsford, UK) after the retarder plate is used to select the incident polarization. The red filter (Edmund Optics, < 1 % transmission for wavelengths < 570 nm and < 90 % transmission for wavelengths < 620 nm) blocks most of the SH signal generated in the optics before the incident light interacts with the sample. The achromat lens 1 (Edmund Optics, focal length f $= 35$ mm, near infrared (NIR) antireflection coated) is used to tightly focus the incident beam on the sample to generate high intensities of up to 100 GW/cm^2.

The sample is mounted on a computer controlled three-dimensional stage (Newport, Irvine, CA, USA) that allows azimuthal angle rotation and translational movements of the sample. Lens 2 (Edmund Optics, double convex, f $= 125$ mm, visible-NIR antireflection coated) in branch B of the set up is used to collect the SH and fundamental signals transmitted through the sample. The blue filter (Schott AG, Mainz, Germany, BG-39, short-pass filter > 60 % transmission for wavelengths between 350 nm and 590 nm and < 0.01 % transmission for > 700 nm wavelengths) blocks the fundamental beam and allows the generated SH to pass through and detected by sensitive photomultiplier tube (Hamamatsu Photonics, Japan, H6780-

03 series) equipped with a high speed amplifier (Hamamatsu Photonics, C5594) connected to a lock-in-amplifier (Ithaco Inc. NY, USA, Dynatrac Model 393) which further amplifies signals from the PMT by averaging over the 80 MHz signal in combination with a 500 Hz light chopper (Thorlabs MC1000A) which increases the signal to noise ratio.
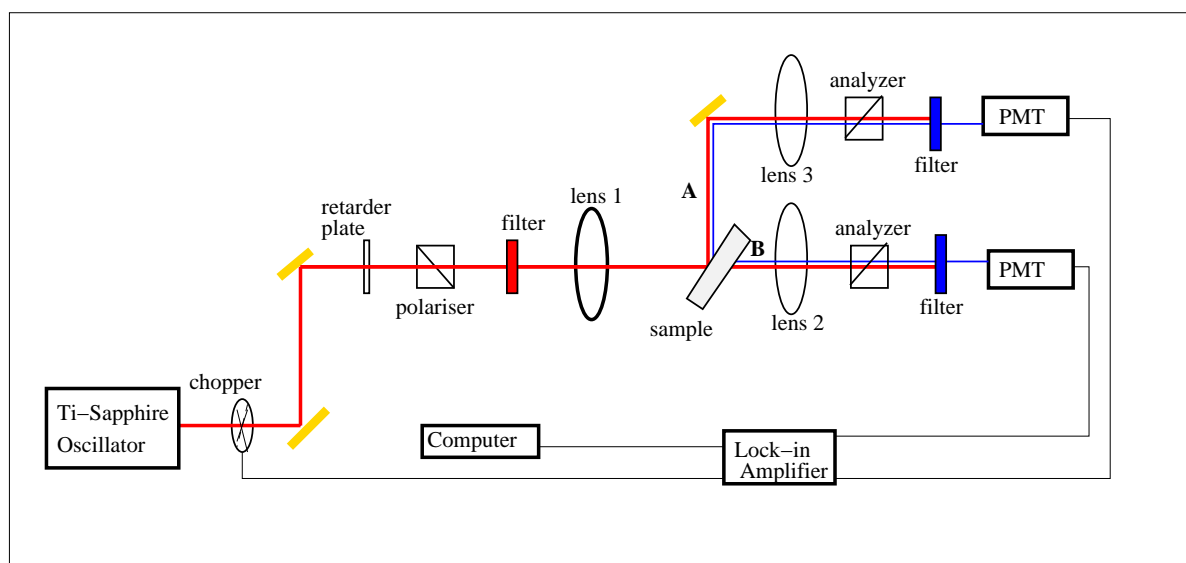
Figure 4.5: A sketch diagram showing the experimental setup used for SHG measurements from Si membranes.

The SH signals were computer recorded with a temporal resolution of 0.2 s. Data acquisition was achieved by a computer equipped with National Instruments Labview Programme.

The SHG experiments can be performed in all the four polarisation combinations in excitation and detection that is p-p, p-s, s-p and s-s (p - parallel to the incident plane, s - perpendicular to the incident plane). For time dependent SHG measurements carried in this study the p-p polarisation combination was used. The following experiments were carried out using the experimental set up shown in Figure 4.5:

(i) Time-dependent SHG measurements in reflection from Si membrane: A single PMT was used and only branch A shown in Figure 4.5 was used.

(ii) Time-dependent SHG measurements in transmission from Si membrane: Only branch B of Figure 4.5 was used and the PMT is identical to one used in (i).

(iii) Angular dependence of SHG in transmission: Branch B of the experimental setup was used while the angle of incidence measured from sample normal is varied by a computer controlled stepper motor and the SH signal is detected by the PMT.

4.3   Experimental Setup for Pump-probe Reflectivity Measurements

Figure 4.6 shows the pump-probe experimental setup designed to measure time dependent reflectivity of Si sample (n-type Si(111) with native oxide, dopant - phosphorus, doping concentration 4-8 Ωcm) using a focussed pump beam. Light from a modelocked Ti-Sapphire oscillator is split by a beam splitter in the ratio 1:9. The pump beam is much stronger than the probe beam. The pump beam is tightly focussed onto the sample by a NIR lens with 35
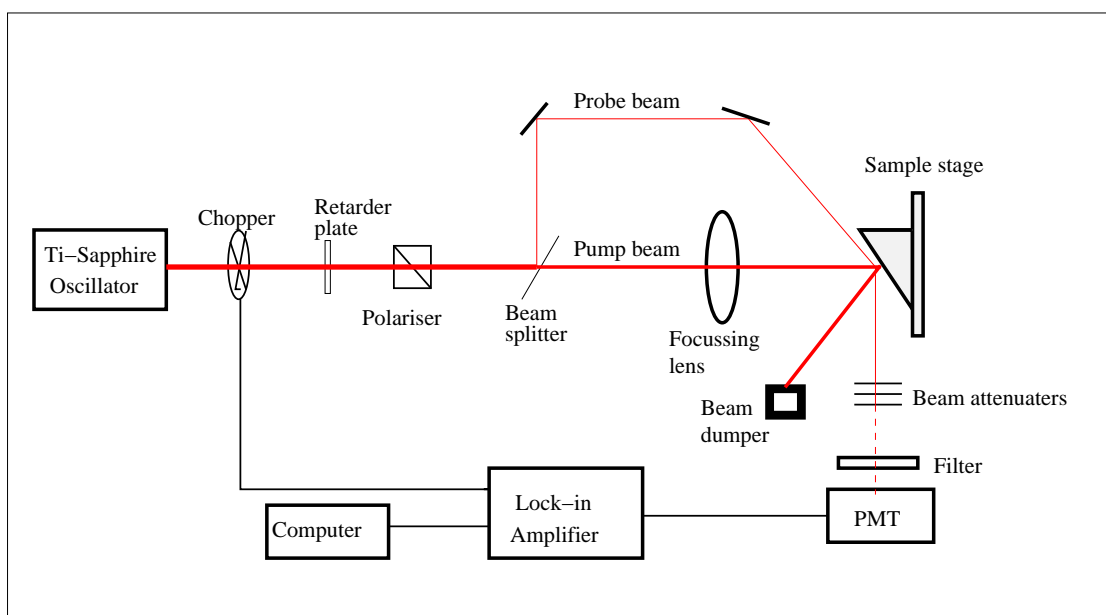
Figure 4.6: A schematic diagram of the experimental setup for time dependent pump-probe reflectivity measurements.

mm focal length at an angle of $\sim 20°$ to the sample normal. The probe pulse is guided to the sample by two mirrors so that the probe beam spot is exactly on top of the pump beam on the sample. The spot size of the probe pulse is adjusted to ensure that there is spatial overlap with

pump beam spot and this is achieved by inserting an aperture in the probe beam path close to the sample. It is not critical that the pump and probe pulse overlap temporally and there is no delay in either pulse. The pump beam reflected from the sample is dumped using a beam dumper and the probe pulse is attenuated by a series of beam attenuators before detection by the PMT. The attenuaters are inserted to protect the PMT from the probe beam. A filter which blocks any stray second harmonic signal generated by the pump pulse on the sample is placed in front of the PMT. Computer data acquisition was achieved by connecting the PMT to a lock-in-amplifier gated with a 500 Hz light chopper. The experiment was performed with the input and detection pump and probe beams all p-polarised.

4.4   Sample Preparation and Characterisation

In this section a description of sample preparation used in this study is given for both as-purchased bulk n-type silicon and p-type silicon membranes. All samples used are natively oxidized Si with (100) and (111) surface orientation. The manufactured samples were characterised by Atomic Force Microscopy (AFM), spectrophotometer and the fs laser. The fs laser was used in the nonlinear characterisation of the membranes. The angular dependence of the SH in transmission for Si membranes is reported as one of characterisation techniques.

4.4.1   Bulk Silicon

Bulk Si wafers (n-type, orientation: $\langle 111 \rangle$, dopant: phosphorus, doping resistivity (concentration) 4 - 8 Ωcm (5.5×10^{14} - 1.1×10^{15} cm^{-3})) used for pump-probe measurements were degreased by sonicating in organic solvents (methanol, acetone, trichloroethylene, acetone, methanol) in the listed sequence and rinsing with deionized water. The samples were immersed for few minutes in diluted hydrofluoric acid (40 %) to remove natural oxide from the wafers. After cleaning, samples were left in dark conditions (room temperature and atmospheric pressure) for at least 48 hours to allow the growth of natural oxide to reach equilibrium. After the ambient exposure a uniform ultrathin natural oxide layer is formed which is approximately less than 5 nm in thickness [2].

4.4.2   Free Standing Si Membranes

Free standing single crystalline silicon membranes were fabricated from bulk silicon using chemical etching process. The bulk silicon sample used was 400 μm in thickness, polished on both sides, with orientation $\langle 100 \rangle$, and moderately p-doped with resistivity of 0.05 - 0.5 Ωcm which corresponds to doping concentrations of 3.2×10^{16}- 6.5×10^{17} cm^{-3} . A low stress silicon nitride layer was deposited by plasma enhanced chemical vapour deposition process on both sides of the wafer to act as a mask against the etching solution. One side of the wafer surface was patterned in an array of squares (4 mm by 4 mm) of exposed silicon while the other side was completely masked. The patterned wafer was immersed in a tetramethylammonium hydroxide (TMAH) etching bath under clean room conditions. The etching bath temperature was regulated around 60°C and continuously renewed mechanically. The wafer was rotated regularly to minimize roughness on the exposed areas. After $\sim$ 72 hours in the slow etching bath the desired thickness of the remaining silicon membrane was reached. The etching process was terminated and the silicon nitride mask was chemically removed.
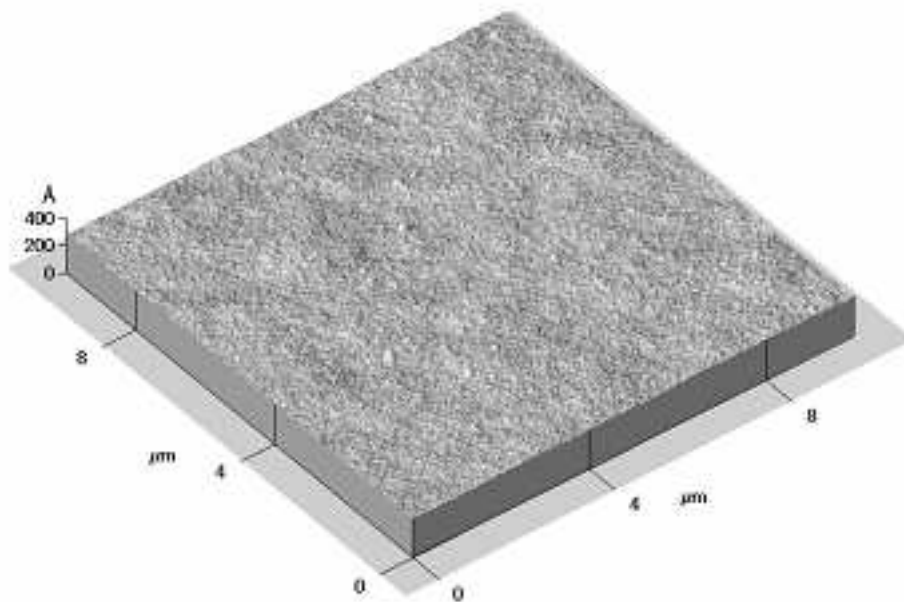
Figure 4.7: AFM image showing surface profile of a Si membrane after termination of the chemical etching process.

Surface profile analysis showed that the etching process produced sharp edges on each square membrane. The membrane thicknesses vary slightly from one membrane to the other but an average of 10 μm was achieved by the deep etching process. Figure 4.7 shows the surface morphology of silicon after chemical etching process. The surface roughness was measured by AFM and was found to be in the order of 12 Å. The low surface roughness for the fabricated membranes is necessary in experiments for SHG in reflection and transmission to reduce scattered light on focus. It has been reported that surface roughness can affect the SHG yield as a result of non-uniform oxide formation as well as scattering effects [9, 19, 20, 38, 79, 80]. Further etching of the Si membrane to produce thinner membranes below 10 μm was not possible using the method described above because of difficulty to control the etching process at very small thicknesses.

Free standing silicon membranes of less than 10 μm in thickness were produced from laser crystallized silicon on glass by selectively etching the glass using concentrated hydrofluoric acid (40 %) while the top thin silicon was protected by a photoresist. Free standing membranes between 400 nm to 2 μm were produced by this process. Figure 4.8 shows the transmission spectrum of all the membranes that were fabricated. The Si membranes transmit light down to 400 nm, but bulk silicon ($>$ 200 μm in thickness) does not transmit in the region 400 nm - 850 nm. Thinner membranes transmit more light compared to thicker membranes. The magnitude of the transmitted light at 800 nm increases as the membrane thickness decreases.

In this study only 10 μm free standing membranes were used as samples for SHG measurements because they are easy to handle and can be chemically cleaned several times to grow new native oxide layers. Thinner membranes were fragile, difficult to handle and could be easily damaged by laser irradiation during experiments.

4.4.3   Nonlinear Characterisation of Si Membranes

Figure 4.9 shows a schematic diagram of the experimental set up used to characterise the 10 μm membranes. To investigate the variation of transmitted power in nonlinear regime high intensities on the sample are required and this was achieved by use of focussed light. A NIR
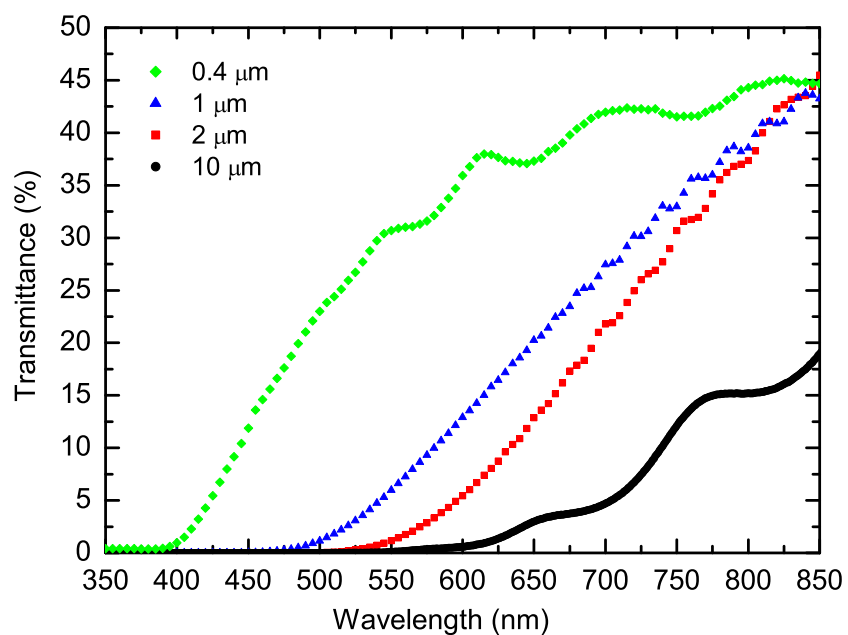
Figure 4.8: The transmission spectrum of free standing Si membranes of different thicknesses prepared at IPHT, Jena laboratory.
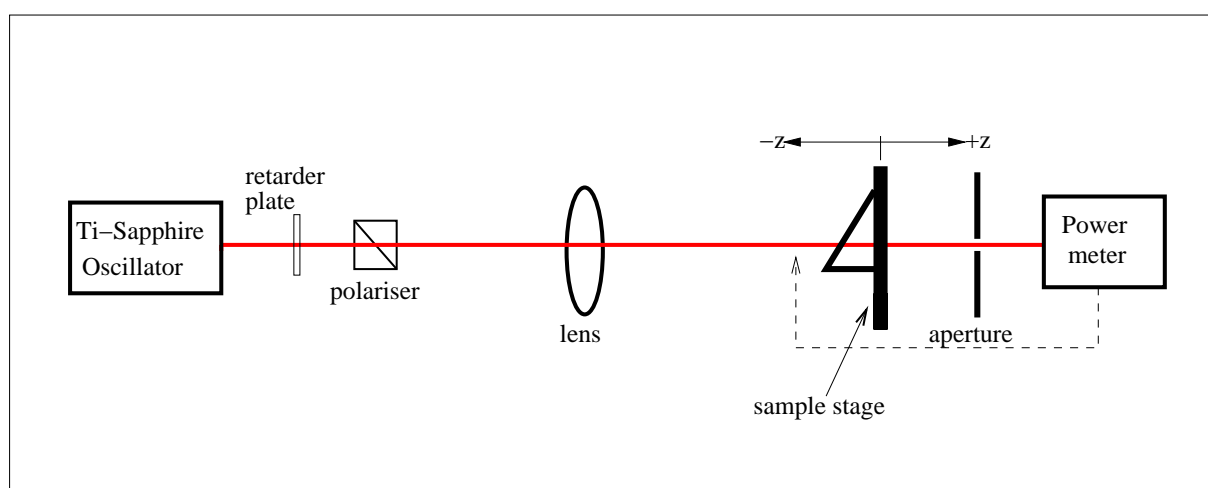
Figure 4.9: A schematic diagram showing the experimental setup to characterise Si membranes using fs laser.

(f = 3.5 cm) focusing lens was used to tightly focus the laser beam on the sample. A power meter (Coherent field master 33-0506-000) with detector sensor (LM-3) capable of measuring high powers was used to measure the incident power before the lens and the transmitted power after the sample. The laser focus remained unshifted on the sample as the incident power was increased while the corresponding transmitted power is measured.

To investigate nonlinear absorption and refractive index changes in the sample, the incident power of the laser was fixed while the sample was scanned through the focus by moving the sample left and right of the focus in an open aperture z-scan experiment. At each chosen value of z, positive and negative (right and left of the focus), the corresponding transmitted power was measured. All the transmitted power was captured by the detector as z is changed in the absence of any aperture. To investigate changes in nonlinear refractive index an aperture with transmissivity of about 50 % was placed after the sample and the procedure for z-scan experiment was repeated.

4.4.4   SHG Angular Dependence in Transmission

The SHG angular dependence in transmission was investigated using the experimental set up shown in Figure 4.5 in which branch B was used in a p-p polarisation combination. The angle of incidence was changed by a stepper motor connected to the computer by rotating the sample while the SHG in transmission was detected and recorded at each angle. The automated data acquisition using the stepper motor was suitable for incident angle less than 30°. At these angles there was no beam clipping on the edges of the membrane. Higher incident angles were achieved by manually rotating the sample to reach angles up to about 60° and the SHG in transmission was recorded at each chosen angle of incidence. A virgin spot on the membrane was used and the laser focus on the sample was optimized at each chosen angle of incidence.

Chapter 5

Experimental Results

In this chapter the experimental results are presented. The samples were prepared as described in Section 4.4. The experimental results obtained using the z-scan technique to characterize and calculate nonlinear coefficients of the Si membrane are reported. The temporal evolution of the SH response measured in transmission and reflection at different incident laser powers for the membrane are presented and described. The SH yields in transmission and reflection geometries were measured at different laser powers and the results for the two detection geometries were compared. Lastly, time dependent pump-probe reflectivity measurements performed at different laser powers using bulk n-type Si(111) are also reported.

5.1   Characterisation of Si Membranes

The transmission change of the incident light was investigated at different incident laser intensities. Z-scan technique was used to investigate transmission change as the sample is scanned through the laser focus at normal incidence for fixed incident laser power. The effect of changing the angle of incidence on the SHG yield measured in transmission from the Si membrane is also reported as part of the characterisation technique.

5.1.1   Nonlinear Optical Characterisation

Figure 5.1 shows the change in transmittance, reflectance and absorbance of the Si membrane when irradiated with different incident laser powers. The modelocked fs laser was focussed on the front surface of the sample and the change in transmitted and reflected fundamental laser light was measured at different incident laser intensities which was achieved by varying the laser power. The transmitted and reflected light from the sample was measured by the
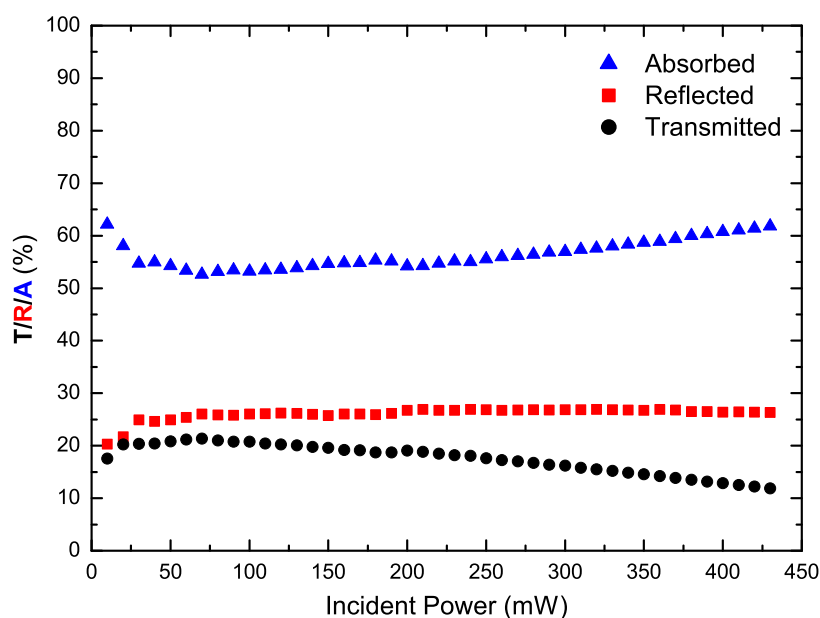
Figure 5.1: A graph of transmittance (T), reflectance (R) and absorbance (A) of a Si membrane measured at different incident laser powers.

power meter which averages the power of the light falling on the detector. Each data point corresponds to the power measured after exposing the sample for the same time duration to ensure that time dependence does not influence the results. Furthermore the power meter is not sensitive to small changes caused by exposing the sample for longer time. The values of absorbance plotted in Figure 5.1 were calculated by neglecting scattered light on the sample. As the incident intensity increases the magnitude of transmitted light decreases and the light absorbed by the material increases as shown in Figure 5.1. The reflected light at different input

powers remains almost constant. Both the sample and the focus remain unchanged throughout the experiment.
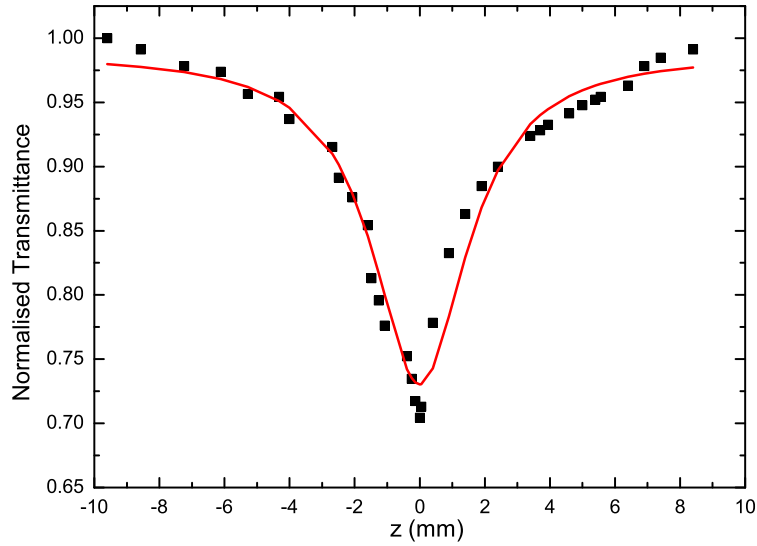
Figure 5.2: An open aperture z-scan ($S = 1$) result showing the change in transmittance as the sample is scanned through the laser focus with a maximum intensity of 90 GW/cm^2. The solid line is a fitting curve according to equation 3.42.

Figure 5.2 shows the change in transmitted signal as the sample is scanned through the focus of the laser beam using the open aperture z-scan technique (see Section 3.2.3). The transmitted signal shows a pronounced minimum at z = 0. At z = 0 the intensity of the incident beam is maximum. As the distance between the sample and focus increases (towards the right and left sides) the transmittance of the sample increases. For large distances of the sample from focus, the magnitude of the transmitted light is almost constant.

Figure 5.3 was obtained when the aperture was partially closed to transmissivity of approximately 50 % ($S \approx 0.5$). Figure 5.3 shows that when the sample is far away from focus ($z \approx \pm 5$), the transmittance change is very small. When the sample is close to the focus there is an increase in transmittance to reach a maximum value at $z \approx -2$. There is a decrease in transmittance from a maximum value which occurs at $z \approx -3$ to a minimum value which occurs at $z \approx 3$.
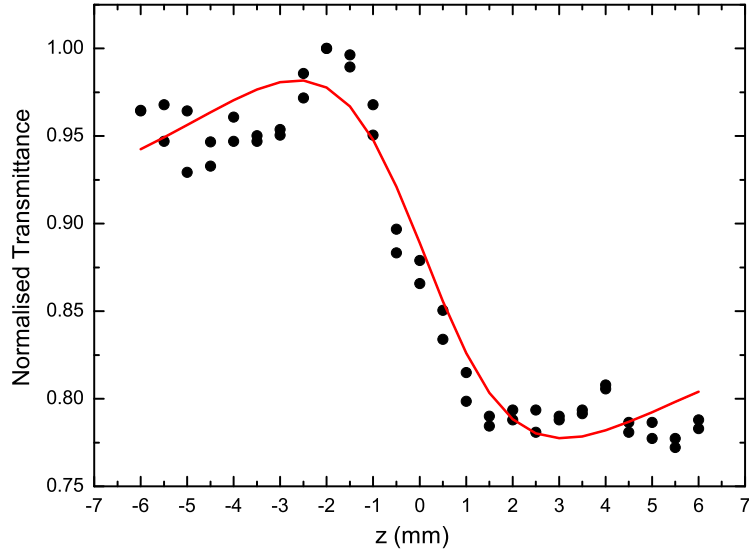
Figure 5.3: The change in transmittance measured from a Si membrane by z-scan experiment obtained from a closed aperture ($S \approx 0.5$) technique when the maximum laser intensity is about 90 GW/cm^2. The solid line is a fitting curve according to equation 3.43.

5.1.2 SHG Angular Dependence in Transmission

Figure 5.4 (inset and main graph) shows the SH intensity measured in transmission from a Si membrane for different incident angles. All measurements were performed in p-p polarization combination at an average incident intensity of $\sim$ 20 GW/cm^2. At each chosen angle of incidence the SH signal was optimized by manually changing the focus to get the maximum signal in transmission. The inset in Figure 5.4 shows the results of computer automated data acquisition up to 30°. The automated results show that there is a smooth increase in the SH signal as the angle increases. The results shown in inset agrees with results obtained by manually positioning the sample shown by a red solid line on Figure 5.4. The SH signal increases with angle of incidence. The results show a trend similar to that of the angular dependence in reflection demonstrated by Bloembergen et al [10], confirming that the nonlinear susceptibility tensor at Si/SiO_2 interface has the expected angular dependence characteristics.
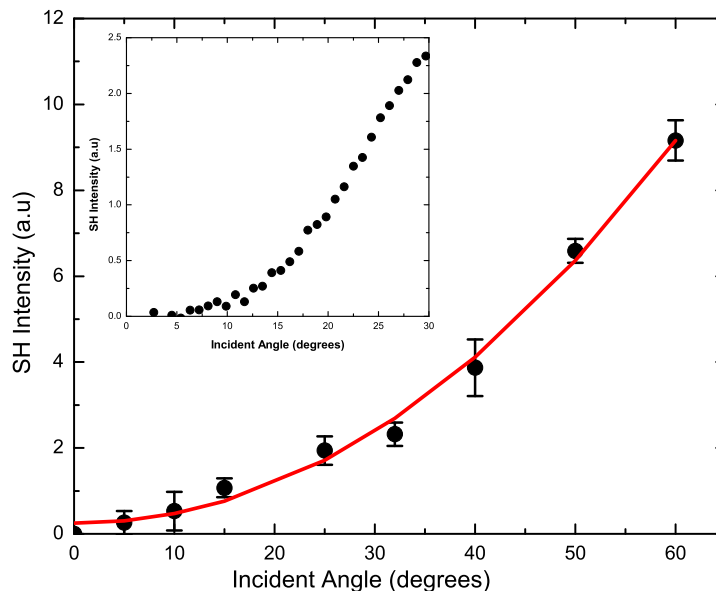
Figure 5.4: Variation of the SH intensity with incident angle measured in transmission for a Si membrane, inset shows more data points for angles less than 30°.

5.2 SH Response from Si/SiO$_2$ Interfaces of a Si Membrane

In this section we present results obtained from Si/SiO$_2$ interfaces of the Si membrane. The time dependent SH signals measured in transmission and reflection are reported. The SH temporal response in transmission and reflection was obtained by probing the same etched interface of the membrane to avoid interface related effects that might arise due to the fabrication process. The reflection measurements were obtained when the etched surface of the membrane was facing the incident laser beam corresponding to interface one in Figure 6.8. Transmission measurements were recorded when the etched surface of the membrane was on the back of the sample corresponding to interface two in Figure 6.8 on the exit of the incident beam. The laser was focussed on interface one for reflection measurements and on interface two for transmission measurements in order to maximise the respective SH signals. This is consistent with our experimental observations in the laboratory which showed that a maximum SH signal is measured in reflection by focusing on the first interface while a corresponding weak SH signal is detected in transmission. The results were recorded one after the other at $\sim 40°$

angle of incidence for different incident laser powers.

5.2.1   Time Dependent SH Response in Reflection
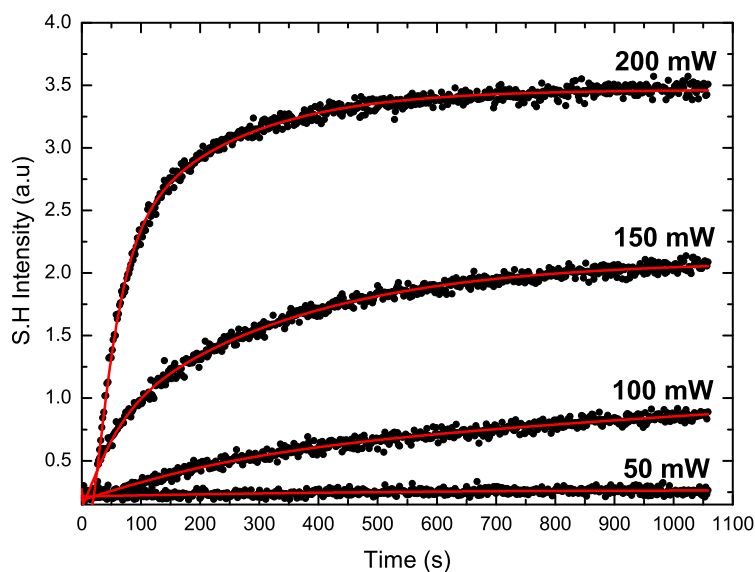
Figure 5.5: The time dependent SH signals from the etched Si(100)/SiO$_2$ interface of the membrane measured in reflection for different incident laser powers. The solid lines are data fittings according to equation 6.20.

Figure 5.5 shows the temporal SH response from Si/SiO$_2$ interface of a silicon membrane measured in reflection at different incident laser powers. The laser focus on the sample was optimised to measure maximum SH signal in reflection. Each time dependent curve was recorded from a virgin spot on the sample. The SH signals rise after the onset of laser irradiation with rates depending on the incident laser power. The SH signal rises throughout beam exposure time of ~ 1000 seconds for low incident powers. For higher powers it is clear that there is a fast rise in the SH signal immediately after the onset of laser irradiation and gradually slows down before the signal reaches a steady state.

The SH response from the membrane measured in reflection is attributed to a well known phenomenon of EFISH and the results are consistent with well established results from other

researchers [20, 36, 41, 81]. The observed SH temporal evolution can be numerically reproduced by two exponential functions according to equation 6.20 shown by solid lines. The temporal SH response measurements for laser powers > 200 mW were difficult to obtain since the membrane was easily damaged by high incident intensities and long exposure to laser beam.

5.2.2   Time Dependent SH Response in Transmission

Figure 5.6 shows the temporal evolution of the SH signal from Si/SiO$_2$ interface/s of Si membrane measured in transmission. The SH response was recorded at different incident laser powers and each curve was obtained from a virgin spot. The temporal SH response in transmission is measured for the first time in this study.
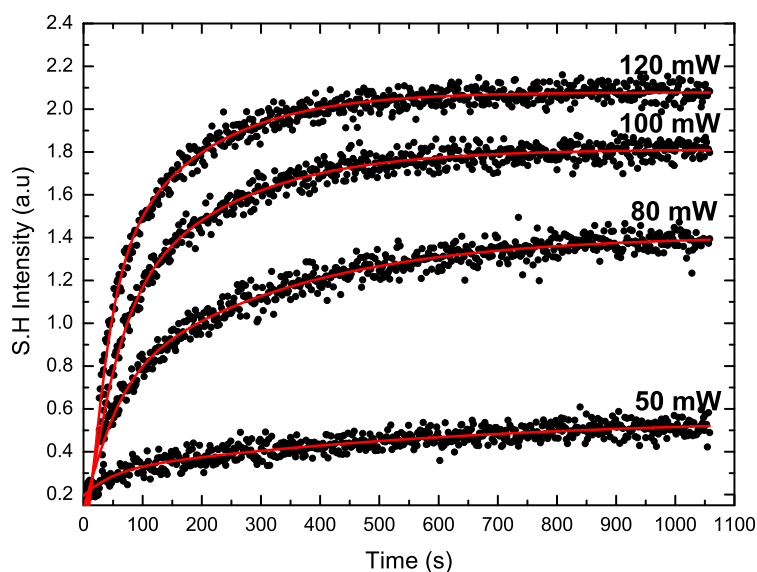
Figure 5.6: The time dependent SH signals from the etched Si(100)/SiO$_2$ interface of the membrane measured in transmission for different incident laser powers. The solid lines are data fittings according to equation 6.20.

The results show an increase in the SH signal response after onset of irradiation. The SH response shows an initial fast rise which slows down and reaches a steady-state value after several minutes of irradiation. The temporal behaviour of the SH signals measured in transmission is similar to time dependent SH measurements for reflection shown in Figure 5.5, therefore the results were numerically fitted with the same equation 6.20 shown by the solid red lines. Differences in the traces shown in Figures 5.5 and 5.6 such as rise times, the magnitude of the SH yield and steady state values at the same incident powers are evident.

5.3   Second Harmonic Yield Measurements

Figure 5.7 shows a set of SH yield measurements performed on different virgin spots of the membrane at various incident laser powers for both transmission and reflection detection geometries. The SH yield was recorded after two minutes of pre-irradiation to allow a built up of a measurable signal from the PMT. Five values were recorded in a one minute interval and averaged for both transmission and reflection. The transmission and reflection measurements were obtained after optimizing the position of the focus to record maximum SH signal in each case.

The bold lines are data fittings to investigate the dependence of SH signal yield on incident laser power/intensity. The experimental data show a dependence on P^x where P is the incident laser power and $1.5 \leq x \leq 3.0$. The values of x tend to be lower for transmission measurements ($1.5 \leq x \leq 1.6$) and higher for reflection measurements ($2.0 \leq x \leq 3.0$). All the graphs show that the SH yield measured in transmission is always higher than SH yield measured in reflection for the incident laser powers used in this investigation. A measurable SH yield could be recorded at low incident powers (from ~ 20 mW) in transmission geometry compared to reflection geometry in which a measurable signal could only be obtained at much higher incident powers (from ~ 50 mW).
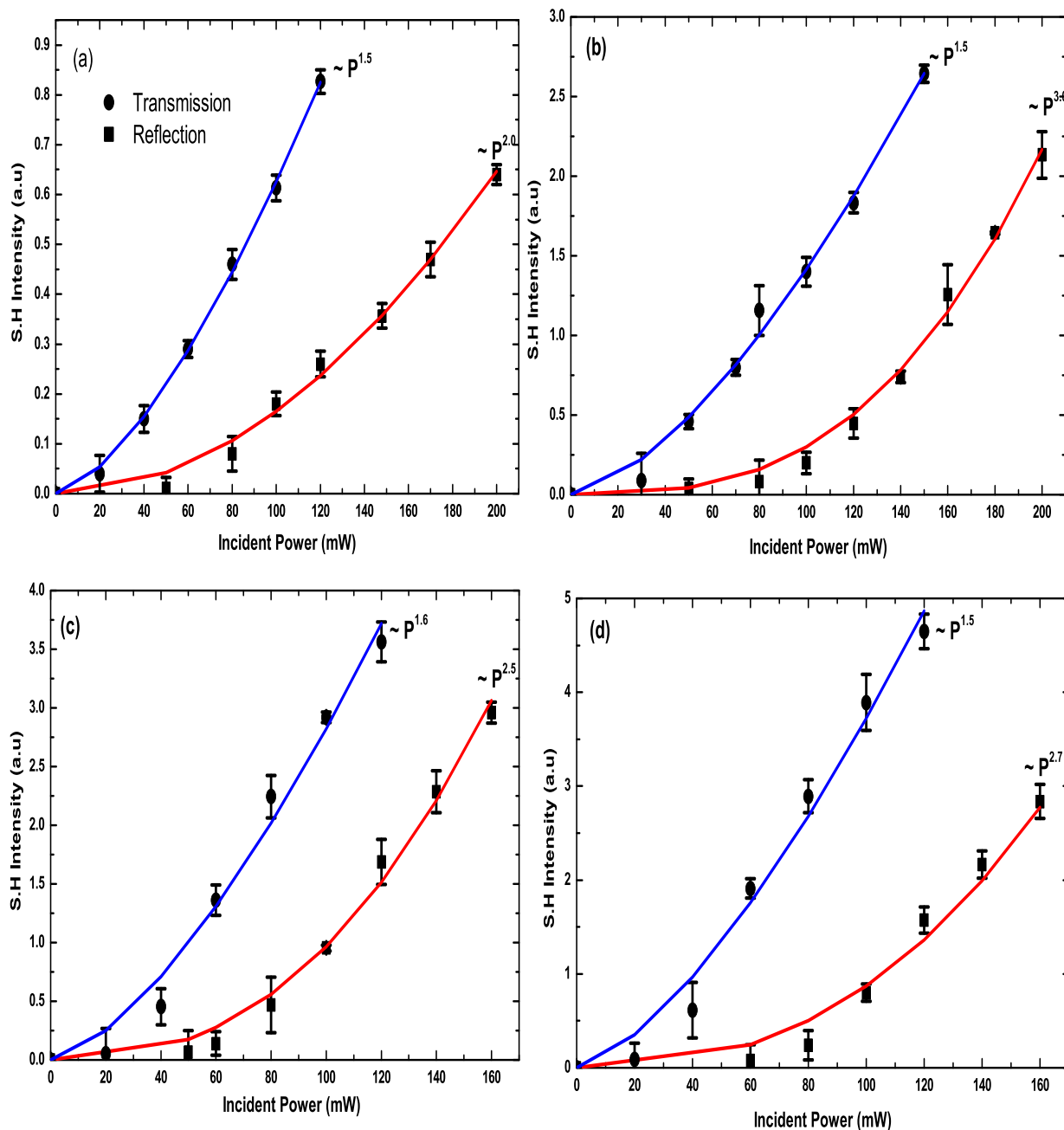
Figure 5.7: A comparison of the SH yield measured in transmission (blue) and reflection (red), from the etched Si(100)/SiO$_2$ interface of the membrane from different spots. All measurements were performed at an incident angle of 40°. The solid lines are data fittings in which the dependence on laser power is indicated by P^x on the graphs.

5.4   Time Dependent Reflectivity Measurements

Figure 5.8 shows a time dependent pump-probe reflectivity signal observed when n-type Si(111) with native oxide is irradiated with pump power of 300 mW at 800 nm incident wavelength. The pump and probe beams were incident at $\sim 20°$ and $40°$ to the sample normal respectively. The pump and probe beams were stationary that is no time delay between the pump and probe pulses. Firstly the probe beam is reflected from the sample in the absence of the pump beam and the reflected signal is recorded for approximately 120 seconds to be used as reference signal which is represented by R in our results. It was observed that the probe signal recorded in the absence of the pump beam remained constant during the irradiation period. Subsequently the pump beam is unblocked to irradiate the probed spot and the reflected probe beam is recorded over several minutes in the presence of the pump beam. The pump and probe beam spots are aligned to overlap spatially on the sample.
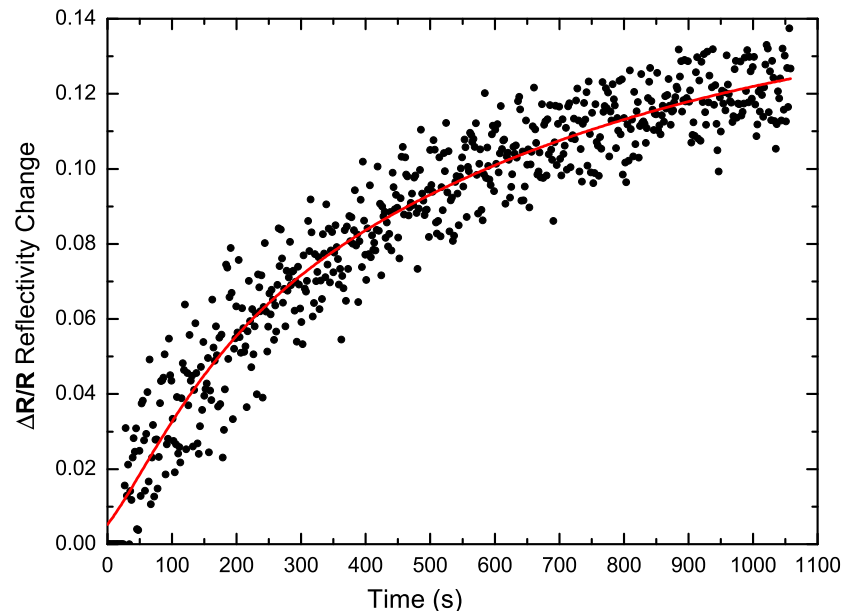
Figure 5.8: Typical time dependent reflectivity response from n-type Si(111)/SiO$_2$ interface measured over 1100 seconds (~ 18 minutes) of irradiation using pump-probe technique at a pump power of 300 mW for an incident wavelength of 800 nm. The red line is a fitting using a bi-exponential function.

Figure 5.8 shows the time dependent reflectivity response when the sample is irradiated with a focussed pump beam while the reflectivity of a weak probe beam is monitored. The plot is of $\Delta R/R$ where R is the reflectivity in the absence of pump beam (reference) and $\Delta R = R(t) - R$, $R(t)$ is the time dependent reflected signal at any time t during irradiation in the presence of both pump and probe beams. As the duration of pump beam exposure on the sample increases the change in reflectivity increases as shown in Figure 5.8.
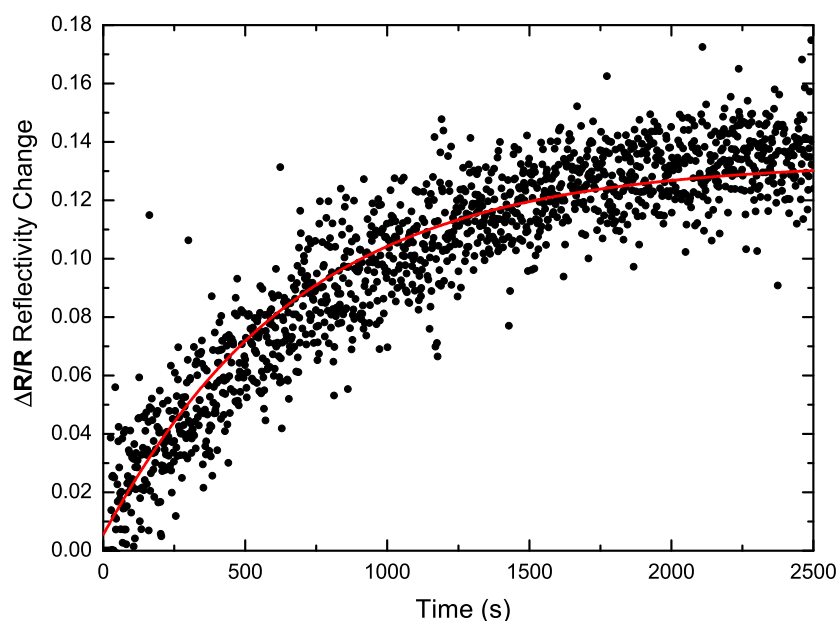
Figure 5.9: Time dependent reflectivity response measured for 2500 s ($\sim$ 40 minutes) of irradiation of the n-type Si(111)/SiO$_2$ interface with pump power of $\sim$ 300 mW. The red line is a fitting using a bi-exponential function.

Figure 5.9 shows the change in reflectivity when the sample is exposed to the pump beam for a longer time twice the exposure time shown in Figure 5.8. The results show that the change in reflectivity will eventually reach a steady-state if the sample is irradiated for a long time. The change in reflectivity reaches a steady-state around $\sim$ 2000 seconds of irradiation. The rate of increase of the reflectivity and the time it takes for the signal to reach a steady-state depends on how well the pump beam and probe beam spots overlap on the sample. If the probe beam spot size is on the center of the pump spot in the region of maximum pump intensity the

change in reflectivity is much faster and reaches steady-state earlier.
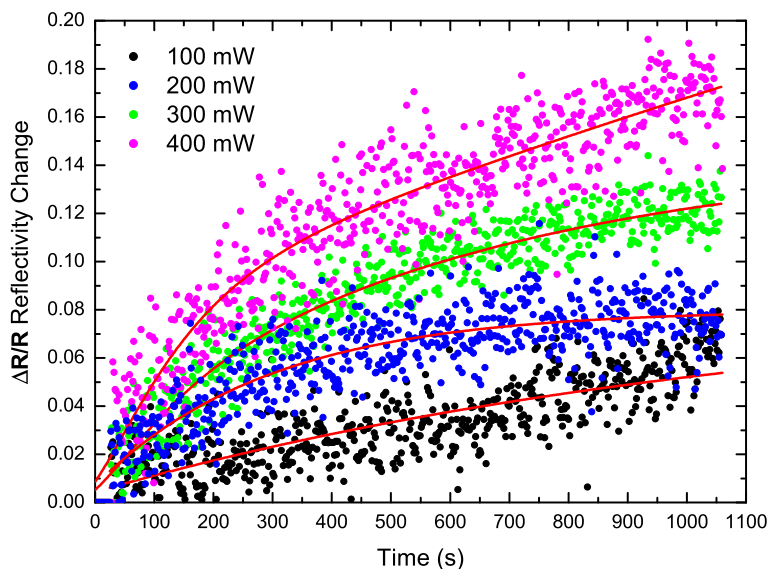
Figure 5.10: The temporal evolution of reflectivity for n-type $Si(111)/SiO_2$ interface measured at different pump powers at a fixed wavelength of 800 nm.

The change in reflectivity was also investigated for different pump powers incident on the sample as shown in Figure 5.10. A pronounced increase in the reflectivity was observed at high pump powers ($\geq$ 100 mW) as shown in Figure 5.10. At low pump powers $<$ 100 mW, no measurable change in reflectivity was observed for the sample investigated in this study. The results at different incident powers were limited by the laser power output. The average incident power could not be increased above 400 mW (chopped), therefore measurements above this value could not be recorded.

The time dependent pump probe reflectivity results shown in Figures 5.8, 5.9 and 5.10 were obtained when the fundamental laser wavelength was fixed at 800 nm. Figure 5.11 shows the time dependent reflectivity response of the sample at a fixed wavelength of 770 nm. The results were similar to those obtained at 800 nm. Differences in the increase rate could be due to other factors such as alignment. A similar time dependent reflectivity response was observed at different wavelengths near 800 nm. The time dependent reflectivity measurements
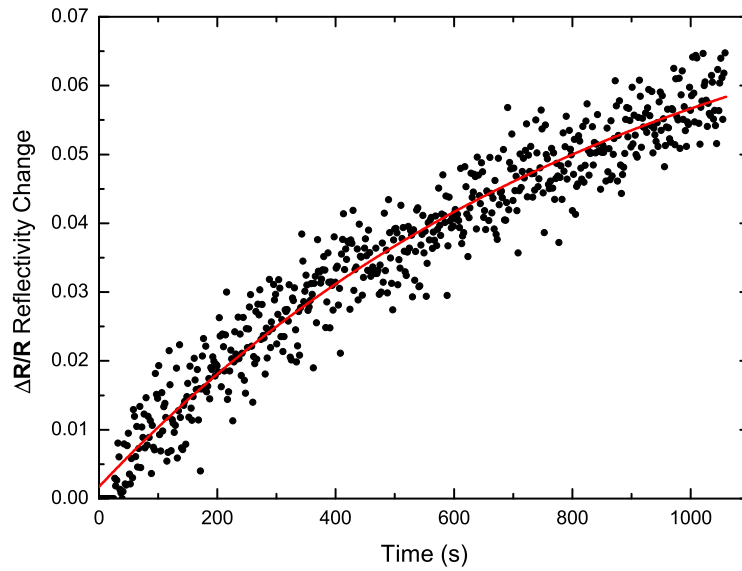
Figure 5.11: The temporal evolution of reflectivity for n-type $Si(111)/SiO_2$ interface measured at ~ 300 mW of pump power at a wavelength of 770 nm. The red line is a fitting using a bi-exponential function.

are reported for the first time and the interpretation is provided in the next chapter.

Chapter 6

Discussion

In the following chapter the experimental findings are discussed and the physical interpretation of the results obtained in this study are given and explained. Firstly, we explain the nonlinear characterisation of the membranes in which the results of z-scan measurements and discussion of self-focussing are presented. A physical model for SHG in transmission and reflection for the membrane is presented which is later used to interpret results obtained. Time dependent SH response measured in reflection and in transmission is discussed and analysed. SH yield measurements for transmission and reflection geometries are compared and discussed. Lastly, we provide interpretations of time dependent pump-probe reflectivity measurements.

6.1   Characterisation of Si Membranes

6.1.1   Nonlinear Optical Characterisation

The transmittance of the Si membrane decreases considerably (from 20 % to $\sim$ 12 %) with increase in incident laser power as shown in Figure 5.1. The increase in incident laser power increases the intensity of focussed light on the sample. The absorbance of the sample was found to increase with incident laser power. The results shown in Figure 5.1 confirm that nonlinear effects such as multiphoton absorption cannot be neglected when Si membranes are

irradiated with high intensity laser beams. In low intensity CW irradiation the transmittance and absorbance should be constant when the sample is irradiated with different laser powers. In the low intensity regime a single electron-hole pair is generated by absorbing one photon. At high incident intensities a single electron-hole pair is generated by absorbing more than one photon. The number of photons absorbed increases with incident intensity. This has an effect of depleting the incident beam as more photons are absorbed in bulk material as evident in Figure 5.1.

The minimum transmission value shown in Figure 5.2 corresponds to high intensity on the sample. In addition to single photon absorption, the decrease in transmittance or increase in absorbance shown in Figures 5.1 and 5.2 is attributed to multiphoton absorption such as two-, three- or four-photon processes [55]. For 1.55 eV laser photons used in this study, two photon absorption (TPA) occur via an intermediate virtual energy level to reach the Si direct band gap energy level of 3.1 eV. Three photon absorption is enhanced by a two photon resonance and the energy of three photons (4.65 eV) is sufficient to promote electrons to the SiO_2 conduction band where they are subsequently trapped. The effective absorption coefficient in Si will increase from α (single photon absorption) to α_{eff} given by $\alpha + \beta I + \gamma I^2$ for multiphoton absorption process. We assumed that the highest multiphoton process in which electron-hole pairs are generated is the three photon absorption.

Figure 5.3 shows that when the sample is far away (negative z) from focus, nonlinear effects are negligible because of the low intensity on the sample. The transmitted intensity measured at the aperture is unaltered. As the sample moves closer, just in front of the focus, the increase in beam intensity causes self-focusing in the sample. The sample acts as a thin lens which tends to collimate the beam leading to a smaller beam at the aperture and an increase in transmittance is measured after the aperture [82]. If the sample is at the focus ($z = 0$) it is equivalent to placing a thin lens at the focus and this does not alter the transmitted intensity. The change in transmission at $z = 0$ will be largely due to strong multiphoton absorption due to high intensity at focus. If the scan continues and the sample crosses the focal plane, to the right (positive z) self-defocussing occurs [61]. The beam is expanded due to nonlinear refraction and this causes a decrease in the transmitted intensity at the aperture. Far past

the focus both the nonlinear refraction and nonlinear absorption effects are again negligible therefore the intensity at the aperture remains unaltered.

Using the sample thickness of Si membrane, and the linear absorption coefficient of Si and the curve fittings shown in Figures 5.2 and 5.3 the TPA coefficient was obtained $\beta = 9.7 \pm 1.2$ cm/GW and the nonlinear refractive index $n_2 = (1.7 \pm 1.5) \times 10^{-4}$ cm^2/GW. In our calculations we assumed that the TPA is much stronger than higher order multiphoton absorption processes and Fresnel losses were incorporated in calculating peak intensity inside the sample. Results published recently by Bristow and coworkers [70] showed that $\beta = 2.1 \pm 0.4$ cm/GW and $n_2 = (4.7 \pm 2.0) \times 10^{-5}$ cm^2/GW, for $\lambda = 1220$ nm using 200 fs laser pulses at 1 kHz repetition rate. The sample used was a double sided polished crystalline Si(001) and 125 μm in thickness. Reitze et. al. [83] obtained the values of TPA as 15 cm/GW $< \beta <$ 36 cm/GW $\pm$ 6 cm/GW for a two photon energy range 551 nm $< \lambda <$ 620 nm. The differences in our calculated values of β and n_2 with the published results is expected since the values are wavelength dependent.

6.1.2 Effects of Self-focussing on Membranes

One of the nonlinear process that can significantly affect the interpretation of our results is the effect of self-focussing. The intensity on the sample is calculated by using beam spot size on the sample which depends on how tightly the beam is focussed. In these measurements the beams were focussed on different interfaces to obtain the maximum SH signals in each detection geometry. In transmission the beam is focussed after propagating in bulk Si unlike in reflection. It is possible that the beam spot sizes can be different for each detection geometry. Smaller beam spot sizes will lead to high intensities on the sample. We suggest that high intensities on the second interface are only possible when the beam spot size is much smaller for transmission measurements compared at the first interface for reflection measurements. This situation can physically occur if the Si membrane can induce an intensity dependent positive lens as the beam propagates in bulk Si which tend to focus the incident beam tighter than at the first interface.

The effect caused by self-focussing which causes a photoinduced lens can couple the artificial

lens used in the experiment to tightly focus the beam on/near the second interface to a smaller beam spot size than the one caused by artificial lens alone. The photoinduced lens is a nonlinear process and occurs through self-focussing. This can give rise to more intensity probing the second interface which can give rise to more SH signal in transmission than in reflection. In the next paragraph we discuss whether self-focussing in Si membranes is practically possible, if so the process can easily explain results of SH measurements in transmission and reflection.

Self modelocking in Ti:sapphire lasers is based on the principle of self-focussing. The Ti:sapphire crystal rod used is typically 10 mm in length in order to observe effects of self-focussing [84]. We argue that self-focussing is less likely in Si membranes used in this study since the samples are very thin (~ 0.01 mm). Furthermore the results of z-scan measurements carried out in this study showed that the nonlinear refractive index is approximately in the order of 10^{-4} cm^2/GW. The highest intensity employed for SHG in transmission is say about 30 GW/cm^2, this will change the refractive index of silicon from 3.675 to about 3.678. We suggest that this value is too small to cause any self-focussing or self-lensing effects.

Using the value of n_2 obtained in this study we can calculate the focal length induced by the nonlinear lens using the formula [47],

$$f = \frac{n_o \omega_o^2}{4 n_2 I_o L},\tag{6.1}$$

where n_o is the linear refractive index, ω_o the beam spot radius on the sample, I_o the peak incident intensity (~ 100 GW/cm^2), n_2 the nonlinear refractive index ($(1.7 \pm 1.5) \times 10^{-4}$ cm^2/GW) and L is the interaction length of the incident light with the medium. The induced focal length calculated is about 190 μm. The focal length induced is greater than the sample thickness, therefore there is no self-focussing that can be caused by the nonlinear lens within the medium.

To investigate the effect of self-focussing experimentally, the incident beam spot sizes for transmission and reflection SHG were measured using the z-scan method. The z-scan method used is the same as the one described above, the only difference is that instead of measuring the fundamental beam the SH power generated by the sample is measured during the scanning
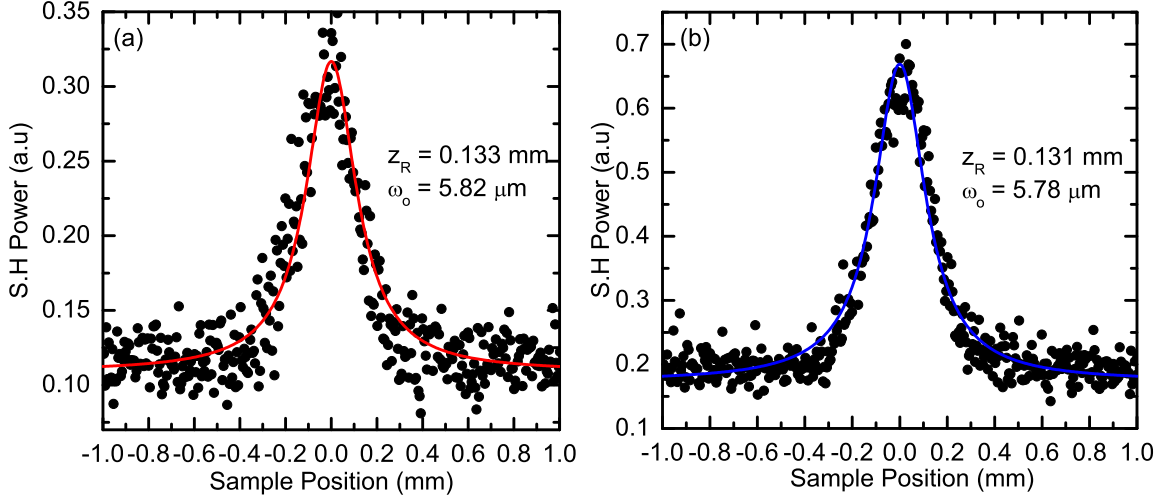
Figure 6.1: The variation of SH power with the sample position through the focus measured in (a) reflection and (b) in transmission at 150 mW and 100 mW incident laser powers respectively. The fitting solid curves are according to equation 6.2.

process. The SH power was measured in reflection and in transmission while the sample position was varied, the results are shown in Figures 6.1(a) and (b) respectively. If we assume a Gaussian pulse of the fundamental beam, the data was fitted using the formula of SH power along the sample position $P_{2\omega}(z)$ given by

$$P_{2\omega}(z) = \frac{z_R K}{z_R^2 + z^2} \tag{6.2}$$

where $K = 2\gamma P_\omega^2 \cos\theta/\pi$, γ is the efficiency of the SHG and P_ω is the beam fundamental power [77, 78]. The Rayleigh length z_R is given by $z_R = \pi\omega_o^2/\lambda$, where ω_o is the minimum beam radius or spot size at $z = 0$ [58]. The values for the Rayleigh length and beam spot size where extracted by data fitting of Figure 6.1 using equation 6.2. The Rayleigh length and the beam spot size (radius) on the first interface (in reflection) were obtained as $z_R = 0.133$ mm and $\omega_o = 5.8$ μm respectively. The Rayleigh length and the beam spot size on the second interface (in transmission) were $z_R = 0.131$ mm and $\omega_o = 5.8$ μm respectively. The SHG z-scan results show clearly that the beam spot sizes in reflection and transmission at interface one and two are the same. Therefore we can conclude that the sample is too thin to cause any significant

self-focussing. In the presence of self-focussing the beam spot size extracted from transmission SHG should be much less than the value obtained in reflection. We therefore rule out effects of self-focussing in our SH measurements to be presented in later sections.

6.2 The Mechanism of EFISH at Si/SiO$_2$ Interfaces of Si Membranes

Figure 6.2 shows the band diagram of a Si membrane with native SiO$_2$ on both sides in the absence of any laser irradiation. Silicon has an indirect band gap of 1.1 eV and a direct band gap of 3.1 eV [76] which are clearly marked in Figure 6.2. The band offset of the Si valence band and SiO$_2$ conduction band is about 4.3 eV and from the Si conduction band to SiO$_2$ valence band [81] is 5.7 eV. SiO$_2$ has a band gap of $\sim$ 8.9 eV. The Si membrane consists of two similar Si/SiO$_2$ interfaces as shown in Figure 6.2.
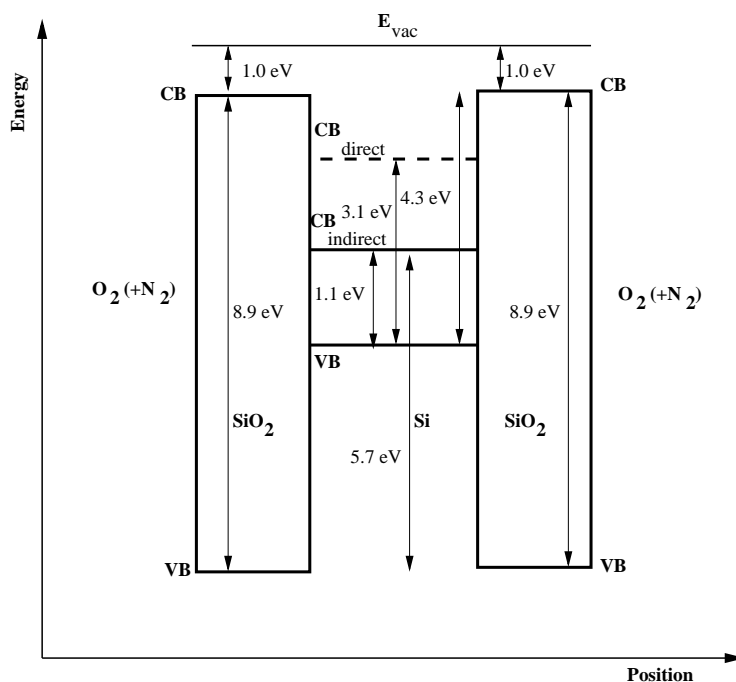
Figure 6.2: The band diagram of Si/SiO$_2$ interfaces of a Si membrane in the absence of any irradiation, CB: conduction band, VB: valence band and E$_{vac}$: vacuum energy level.

Figure 6.3 shows the band diagram of Si membrane when irradiated with intense near infrared

fs laser photons of 1.55 eV energy. The laser was focussed on the first interface of the membrane in order to measure maximum SH signals in reflection. The red arrows in Figure 6.3 show that electrons can be excited from Si valence band to the SiO$_2$ conduction band by absorbing three photons. Direct electronic excitation of the SiO$_2$ layer is negligible due to its large band gap of 8.9 eV. Figure 6.3 shows electron charge transfer from the Si valence band to the SiO$_2$ conduction band at interface one and none at interface two. In practice for $\sim 10~\mu$m Si membrane there will be some charge transfer at both interfaces on irradiation, but experiment has shown that focussing the incident beam on interface one maximises the SH in reflection and minimises the SH in transmission. This corresponds approximately to the model of Figure 6.3. Since the SH signal generated at interface two does not contribute to the SH signal measured in reflection as described in Section 6.3, it is sufficient to consider only charge transfer at interface one as model for SHG in reflection.
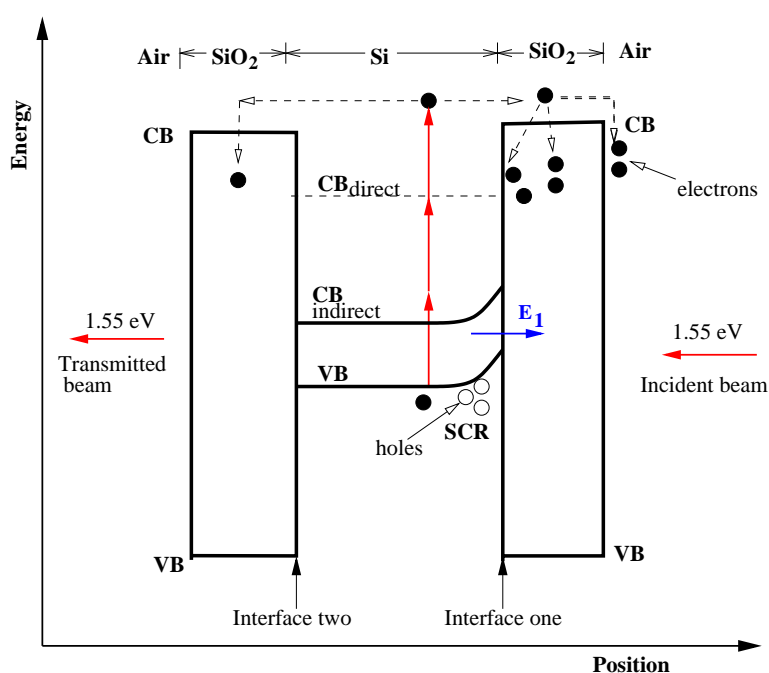
Figure 6.3: Schematic energy band diagram of Si membrane with native Si/SiO$_2$ on both sides when the laser is focussed near the first interface for reflection SH measurements, SCR: space charge region.

Laser irradiation of the sample generates electron-hole pairs in the Si region [38]. Some of the excited electrons acquire enough energy through three photon absorption process (red arrows in Figure 6.3) to overcome the 4.3 eV barrier between the Si valence band and the SiO$_2$

conduction band [81] to be trapped at the Si/SiO$_2$ first interface, in the first ultrathin SiO$_2$ layer or at the SiO$_2$/air interface [3, 36, 81]. Some electrons quickly recombine with holes in the Si valence band and this occurs on picosecond time scales shorter than the repetition rate (12.5 ns) of the incident laser therefore recombination occur between pulses [76]. The incident laser pulses have two purposes, that is creation of charge traps in the oxide and multiphoton transfer of electrons from Si to SiO$_2$ to populate both photoinduced and native trap sites. The generation of trap sites caused by the laser is irreversible [85] and locally confined to the laser beam spot size on the sample [86].

The trapped charges in SiO$_2$ stay longer than the electron-hole recombination times and the laser pulse train at 80 MHz cause a built up of electrons in the oxide. The build-up of trapped electrons establishes a quasi static or slowly varying interfacial electric field E_1 (shown by blue arrow in Figure 6.3) pointing from Si to SiO$_2$. The photoinjection of electrons into the oxide causes a non-equilibrium distribution of local charges and a space charge region (SCR) is established near the first Si/SiO$_2$ interface as shown in Figure 6.3 leading to band bending. Only carriers that are trapped in the oxide between pulses will contribute to the slowly varying electric field at the interface [76]. The interfacial electric field increases during continuous irradiation and this changes the effective interfacial susceptibility tensor according to equation 3.54. The increase in the SH signal upon irradiating the sample is directly related to the time dependent interfacial electric field as shown in equation 3.54.

Figure 6.4 shows the band diagram of Si membrane with a strong charge transfer at the second interface of the membrane. This will be the case in practice if the laser beam is focussed on the second interface. As the contribution of any SH generated at the first interface to the SH signal measured in transmission is zero (see Section 6.3) it is sufficient to consider only the charge transfer at interface two to explain SH in transmission.

The SH signal measured in transmission is caused by electron transfer after absorbing three photons of incident light (shown by red arrows in Figure 6.4) from silicon into the SiO$_2$ conduction band at the second interface followed by electron trapping. The photoinjection of electrons to the oxide establishes an interfacial electric field (E_2, shown by blue arrow in Figure 6.4) at the second interface and this in turn alters the nonlinear susceptibility tensor at the interface
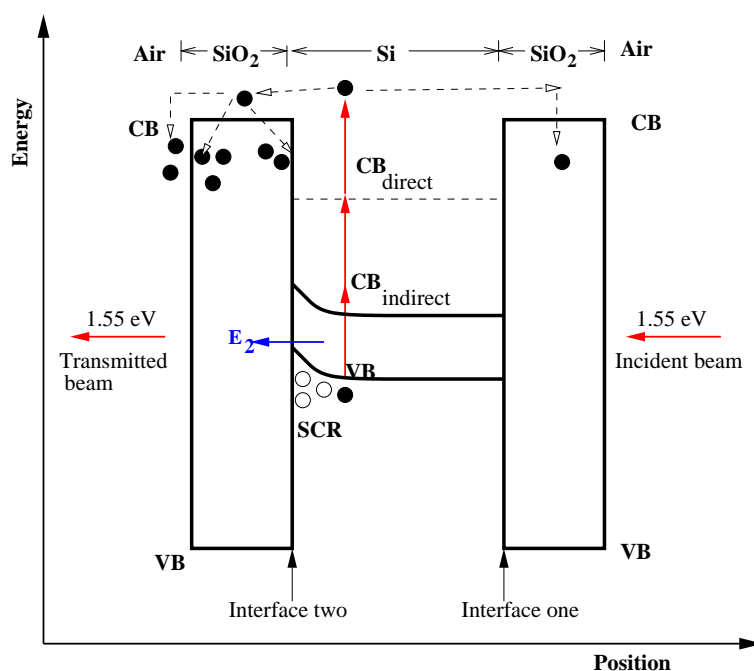
Figure 6.4: Schematic energy band diagram of Si membrane with native Si/SiO$_2$ on both sides when the laser is focussed on the second interface to measure the SH signal in transmission VB: valence band, CB: conduction band, SCR: space charge region.

which has a direct effect to the measured SH signals in transmission. A space charge region occurs at interface two.

At high incident intensities, in addition to electron transfer, hole transfer process (four photon process) which is not shown on Figures 6.3 and 6.4 also occurs establishing an opposing interfacial electric field to the one established by the electrons. The reason why hole transfer is not shown in Figures 6.3 and 6.4 is that it was observed that the Si membrane could not sustain high incident laser intensities where hole transfer can occur as they were easily damaged. Therefore the SH response in transmission and reflection is dominated by electron transfer process for the incident intensities used in this study.

Holes and electrons undergo different trapping and detrapping dynamics. Holes are reported to be heavier and less mobile than electrons in SiO$_2$ [39, 75]. Hole traps have several orders of magnitude greater trapping cross-section and are more abundant in SiO$_2$, particularly thermally grown [75]. Hole injection into SiO$_2$ has an energy barrier of 5.7 eV [75, 76] and requires a four-photon process to be injected into the oxide for the near infrared fs laser pulses therefore

higher intensities are required for hole transfer compared to electron processes. Hole transfer processes are slower because holes are less mobile compared to electrons. The magnitude of the electric field established as a result of hole transfer is much smaller than that of electron transfer because hole effects require four photons compared to a three photon process for electrons. Hole transfer establishes an opposing electric field whose direction is from SiO_2 to Si opposite to the one established by electrons whose direction is from Si to SiO_2.

6.3 Origin of EFISH Signal in Transmission and Reflection

The Si membrane can be described as a system with three distinct regions that are (i) the thin SiO_2 layers with their SiO_2/air interfaces, (ii) the two Si/SiO_2 interfaces on each side of the membrane and (iii) bulk Si between the Si/SiO_2 interfaces.

The effective susceptibility tensor for EFISH generation has two terms as shown in equation 3.53. The $\chi^{(2)}$ term is zero in the bulk centrosymmetric Si and only non-zero at the Si/SiO_2 interface where symmetry is broken. The $\chi^{(3)}$ term is not symmetry forbidden in the bulk Si, but it is multiplied by the time dependent interfacial electric field $E(t)$ induced by charge transfer from Si to SiO_2 upon irradiation. The $\chi^{(3)}E(t)$ term is non zero in the Si as deep as the interfacial electric field penetrates in Si from the interfaces shown in Figure 6.8. Therefore in the absence of interfacial electric field at the Si/SiO_2 interface, SHG occurs in few atomic or surface monolayers [48, 87] because of symmetry breaking at the surface. This SH signal is very small.

In the presence of interfacial electric field the SH signal is enhanced by EFISH originating from the Si/SiO_2 interface and the volume of Si penetrated by the interfacial electric field indicated in Figure 6.8. Although the interfacial electric field can penetrate into Si and the oxide, SHG only occurs in Si since $\left|\chi^{(3)}\right|$ is $\approx 10^4$ times smaller in SiO_2 than in Si therefore EFISH from Si/SiO_2 is dominated by the near-interface electric field in Si [36] rather than the oxide. The other reason to support this claim is that spectroscopy measurements from Si/SiO_2 interface showed the existence of energetic positions of SH resonances which matches with the lowest direct energy gaps in silicon [17, 33, 88, 89] implying that the SH signal originates

from Si atomic layers close to the interface rather than the SiO_2 layer. The SiO_2/air interface contributes in the establishment of the interfacial electric field since the presence of oxygen assists in the trapping of electrons according to Shamir et. al. [90].

The extent to which the photoinduced electric field penetrates in Si can be estimated using the Debye Screening Length formula [32, 91]

$$L_D = \sqrt{\frac{\epsilon_s KT}{q^2 N_D}}, \tag{6.3}$$

where K is the Boltzman constant, T the temperature, ϵ_s relative permeability of silicon, N_D doping concentration. Using the value for the doping concentration of sample used in this study ($\sim 6.5 \times 10^{17}$ cm^{-3}), the penetration depth of the interfacial electric field was obtained as ~ 5 nm. The value is consistent with calculations reported by Lim et. al.. [32]. According to Cernusca et. al.. [85] the photoinduced electric field only penetrates few atomic layers or surface monolayers within skin depth into Si (5 nm). Therefore the measured SH signals originates within 5 nm into Si layers at each interface with no bulk contribution.

Figure 6.5 shows a plot of the penetration depth for different wavelengths in silicon. The penetration depth at the fundamental wavelength of 800 nm is about 12 μm according to optical constants provided in [1] (not shown in Figure 6.5). At SH wavelength (400 nm), the penetration depth in Si is approximately 100 nm shown by dotted line in Figure 6.5. The SH light generated at the first interface of the membrane will be completely absorbed within an interaction length of ~ 100 nm in Si. The thickness of the Si membrane is much greater than the penetration depth of the SH light therefore any SH generated from the first interface is completely absorbed in bulk Si and will not be transmitted to interface two for detection. Using the optical properties of Si we can conclude that there is no SH contribution from the first interface that can be detected in transmission. A similar argument can be used to state that there is no SH contribution from the second interface that can be detected in reflection. Additionally, even when the penetration depth of the interfacial electric field would be deeper than 100 nm which is not true in our case (say approximately penetrating the whole membrane) the measured SH light is limited to that generated within 100 nm from the Si/SiO_2 interface.
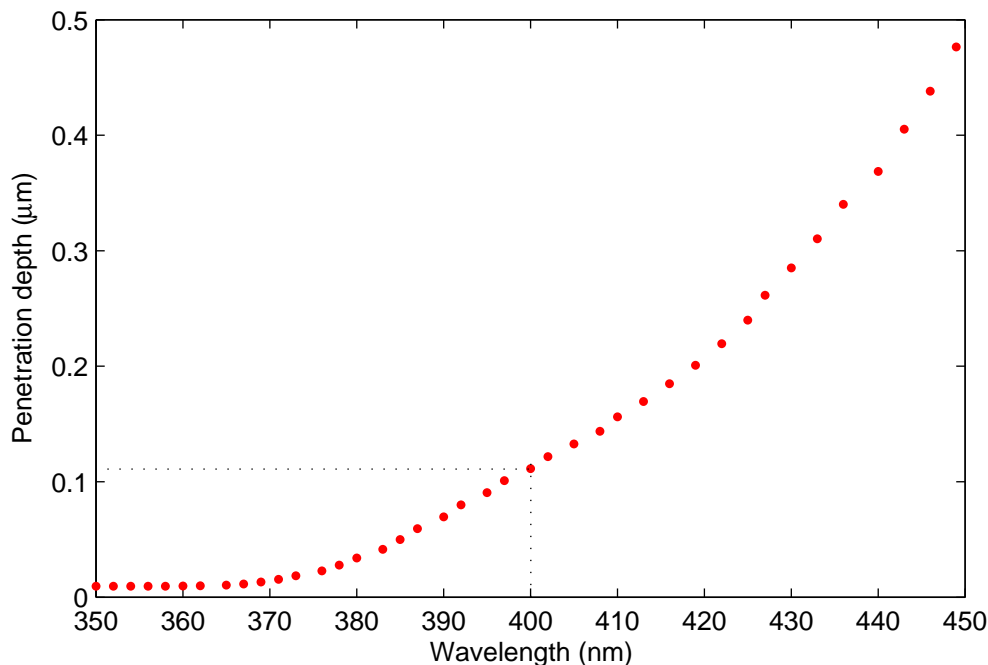
Figure 6.5: A plot of how the penetration depth in Si varies with incident wavelength. Optical data was retrieved from [1].

Experimental data shown in Figure 6.6 confirms that the SH signal measured in transmission originates from the second interface. The laser focus was scanned through the Si membrane while the SH intensity was recorded one after the other in reflection and transmission. It was observed that the peak of SH intensity measured in transmission is shifted relative to the peak of SH intensity measured in reflection as shown in Figure 6.6. The differences in the two peaks support the argument that SH signals measured in reflection originate from the first Si/SiO_2 interface and SH signals measured in transmission originate from the second interface if one assumes that the maximum SH signal occurs if the focus of the beam is centered at the Si/SiO_2 interfaces. The spacing between the two Si/SiO_2 interfaces is equal to the thickness of the membrane. The distance between the two peaks should in theory be of the same order as that of the thickness of the membrane, but high accuracy cannot be expected in practice given the width of the peaks in the measurement. Taking that into account the peak to peak distance in Figure 6.6 of ~ 60 μm is comparable to the membrane thickness of ~ 10 μm. The spatial resolution is too low to resolve 10 μm given the broad peaks.
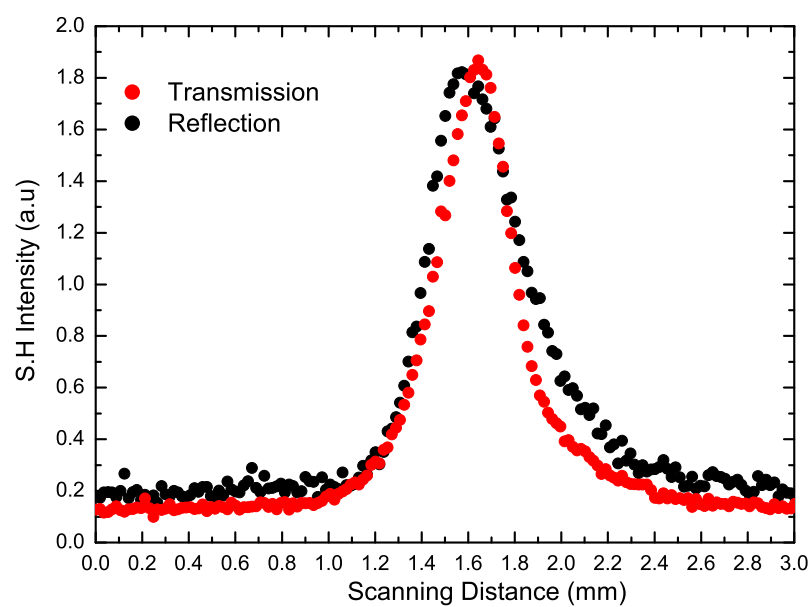
Figure 6.6: Variation of the SH intensity measured in reflection and in transmission as the laser focus is scanned through the Si membrane. The incident laser powers for transmission and reflection measurements were 100 mW and 300 mW respectively.

The following is a list of statements useful to understand SHG in transmission and reflection from Si membranes.

(i) Each fs laser pulse sees the Si/SiO_2 interface as prepared by the preceding pulses. Since the time interval between the laser pulses is not long enough for the charge carriers that were transferred and trapped in the oxide by the last laser pulse to return to the Si, the train of laser pulses contributes to the built-up of an interfacial electric field. For each subsequent laser pulse the photoinduced electric field strength changes by a small amount. Therefore the effective susceptibility tensor of the interface changes with time.

(ii) The SH signal in transmission and reflection originates from two similar but independent interfaces with the first interface contributing to SHG in reflection and the second interface give rise to SHG in transmission.

(iii) The processes such as charge transfer from Si to SiO_2, the change to the interfacial electric field, and photoinduced trap generation by each pulse occurs within the pulse duration.

(iv) The photoinduced electric field breaks the inversion symmetry of the crystal in the region where the interfacial electric field is induced (5 nm) and SHG is allowed in that region through the electric dipole mechanism [27]. The penetration depth of the interfacial electric field at each interface is the same since it is intensity independent but depends mainly on the doping concentration of the sample.

(v) The photoinduced interfacial electric field does not extend along the sample surface (x-direction) as shown in Figure 6.8 but is localized around the fundamental beam spot size and penetrates into the sample along the z-direction. The direction is from Si to SiO_2 at both interfaces as shown by arrows labelled $\mathbf{E}_1$ and $\mathbf{E}_2$ in Figure 6.8. The electric field strength across the interface is assumed uniform like in a capacitor.

(vi) The magnitude of the induced interfacial electric field at each interface contributes significantly to the measured SH signal by changing the effective susceptibility tensors at each interface. At the first interface the incident photons interact with the first interface. Electrons in Si absorb three photons simultaneously from incident photons to acquire

energy which is sufficient to promote them into the SiO_2 conduction band. The physical interpretation is that the electrons acquire sufficient kinetic energy (4.5 eV) to be excited into SiO_2 from Si. The photoinduced charge separation established the interfacial electric field. The same process occur at the second interface.

(vii) At the same incident intensity at the two interfaces the laser beam sees the same atomic arrangement at the first and second interfaces of the membrane therefore the corresponding tensor components of the nonlinear susceptibility tensors $\chi^{(2)}$ and $\chi^{(3)}$ at the two interfaces are equal in magnitude. However the magnitudes and directions of the fundamental electric field and the induced polarisation have to be analysed thoroughly as done in the following Section 6.4.

6.4   SHG Model Applied to Si Membranes

In this section we apply the general model described in Section 3.2.2 to Si membranes used in this study. We derive the equations for only p-polarised light and explain why the model is suitable to apply to Si membranes.

Figure 6.7 indicates the magnitude of the laser power at different positions as percentage of the incident power calculated from Fresnel equations obtained from [92] wavelength of 800 nm and incident angle of $40°$. Part of the incident beam is reflected at the first interface and a fraction propagates in bulk material to be transmitted and reflected at the second interface. A fraction of the beam is absorbed during propagation in bulk material. Multiple reflections can occur due to the thickness of the membrane. Any reflective or transmittive effects caused by the oxide layer are neglected since its thickness is very small (< 5 nm) and the SiO_2 is transparent to both the fundamental and SH signal therefore it can be replaced by air as indicated in Figure 6.7. We assume that there are no reflective or absorptive phenomena associated with surface roughness, damage, or anomalies at the interface.

The transmitted light from the first interface is partly absorbed according to Beer-Lambert's law under conditions of single photon absorption as the light propagates in bulk silicon. The
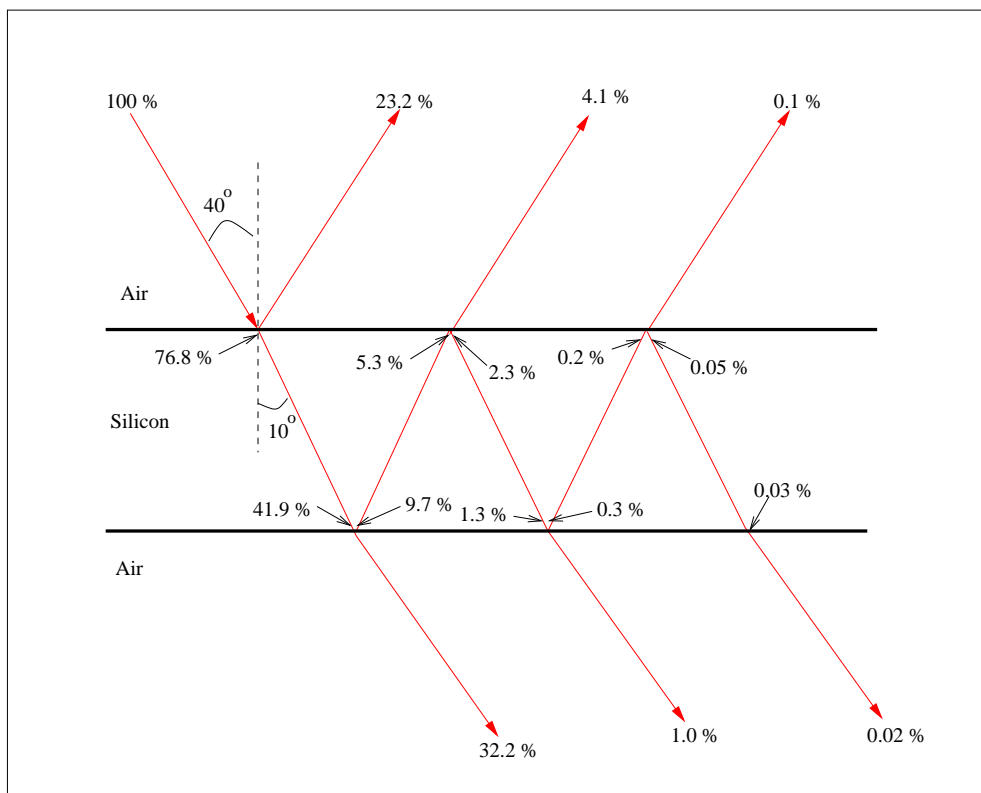
Figure 6.7: A sketch diagram of the Si membrane showing multiple reflections of the incident beam, the magnitude of the laser power at each marked stage is shown. The incident angle was chosen as 40° and the wavelength of 800 nm for p-polarised light.

fraction of the light that is absorbed depends on the wavelength of incident light. The linear absorption coefficient α is related to the wavelength by the formula $\alpha = 4\pi k/\lambda$, where k is the extinction coefficient at each wavelength. Figure 6.7 clearly shows that the first pass of the fundamental laser beam is much stronger than other higher order passes. We neglect effects of higher order passes in EFISH calculations since they are much weaker compared to the first pass therefore their intensities are not sufficient to induce any nonlinear effects on the interfaces.

Figure 6.8 shows the beam geometry on a Si membrane when a laser beam is incident at an angle θ_i, part of the beam is reflected at the first interface at an angle θ_r, and a fraction is transmitted into the bulk Si to exit the membrane at angle θ_o on the second interface. The SH signal can be generated within the penetration depth of induced electric fields at each interface marked $\mathbf{E}_1$ and $\mathbf{E}_2$. The two interfaces of the silicon membrane are assumed to be the same and EFISH signal evolves close to the interfaces, any contributions to SHG by higher order terms from bulk are neglected since they are very small compared to EFISH signal. The EFISH signal that can be measured in reflection is generated at the first interface. This is consistent with EFISH measurements reported in literature performed on bulk Si samples [3, 36, 41, 42, 75, 76, 93].

In Section 3.2.2 we gave a general summary of the model for SHG in reflection and transmission as proposed by Mizrahi and Sipe [54]. The following explains why the model described in Section 3.2.2 is suitable for application to Si membrane samples used in this study.

- The SH signals from the Si membrane are generated from Si/SiO_2 interfaces only with no bulk contribution from the whole Si membrane.

- The SH signals generated in each detection geometry are independent of each other since the SH signals generated from the interfaces is absorbed within a short penetration depth in Si as described in Section 6.3.

- The SH signal in reflection is measured in the same direction as $\hat{\mathbf{k}}_r$ and originates from the first interface only.

- The SH signal measured in transmission is along $\hat{\mathbf{k}}_t$ and is generated at the second
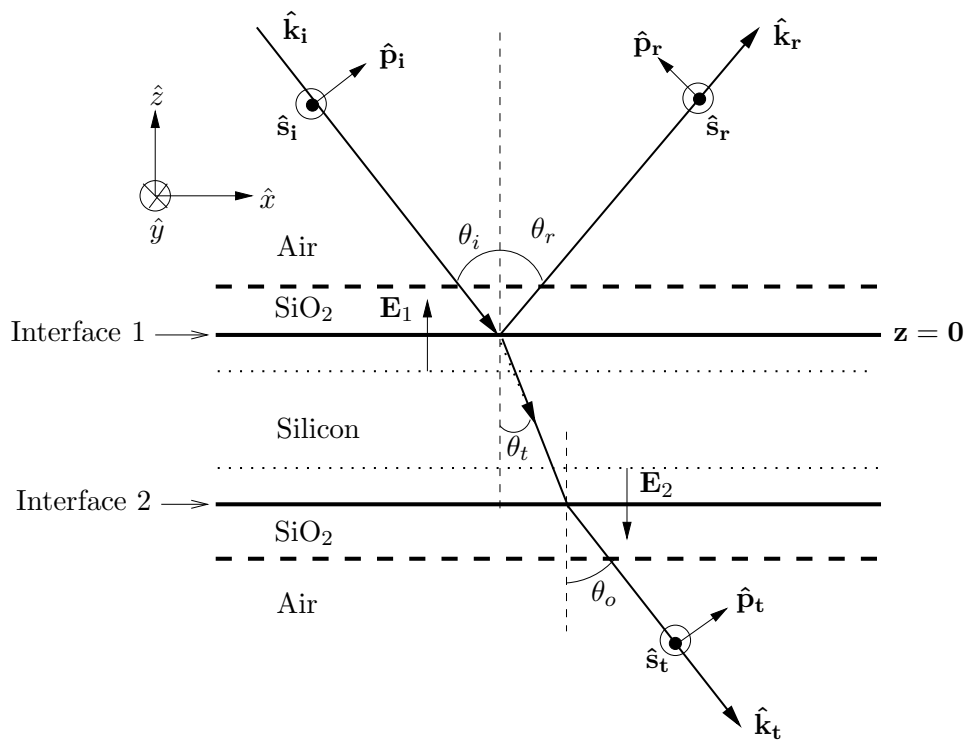
Figure 6.8: A schematic representation of a laser beam incident on a Si membrane part of the beam is reflected at the first interface, and transmitted in bulk substrate to exit at interface two. The interfacial electric fields $\mathbf{E}_1$ and $\mathbf{E}_2$ across each Si/SiO$_2$ interface are indicated.

interface.

- Only a single propagation of the fundamental beam is considered since any higher order reflections are much weaker to induce SHG due to strong absorption therefore we neglect multiple reflections as well consistent with the model derived in Section 6.4.

- In the absence of any charge transfer across the Si/SiO$_2$ interface the surface susceptibility tensor is given by $\chi_s^{(2)}$, the charge transfer changes the tensor due to the presence of the interfacial electric field so that the effective second order susceptibility tensor is given by $\chi_{eff}^{(2)} = \chi_s^{(2)} + \chi^{(3)}.\mathbf{E(t)}$

The fundamental beam incident on Si membrane was p-polarised and the SH light detected in reflection and transmission geometries were chosen to be p-polarised. To derive the expressions for the SH power detected in each geometry we consider p-polarised contributions and drop all s-polarised contributions for all equations derived in Section 3.2.2. We start by deriving the SH power measured in reflection geometry.

The incident light on the sample from medium 1 (for simplicity we regard medium 1 as air since the SiO$_2$ is very thin) is p-polarised therefore the unit vector $\hat{e}^{in} = \hat{p}_{1-}$. We rewrite equation 3.27 as

$$
\begin{aligned}
\mathbf{E}_r^\omega(x, z = 0^-) &= (\hat{p}_{2-}t_{12}^p\hat{p}_{1-}).\hat{e}^{in}|E_{in}|\exp(ipx) \\
&= (\hat{p}_{2-}t_{12}^p\hat{p}_{1-}).\left(\frac{E_{in}}{E_{in}}\hat{p}_{1-}\right)|E_{in}|\exp(ipx) \\
&= \mathbf{e}_r^\omega|E_{in}|\exp(ipx)
\end{aligned}
\tag{6.4}
$$

where $\mathbf{e}_r^\omega = \hat{p}_{2-}t_{12}^p$.

We rewrite the vector $\mathbf{H}^o$ for p-polarised in reflection as

$$
\mathbf{H}^o = \hat{p}_{1+}\hat{p}_{1+} - \hat{p}_{1+}R_{12}^p\hat{p}_{1-}
\tag{6.5}
$$

where the minus sign allow the change in direction of the p-polarised light after reflection at

$z = 0$. The detection of the SH light $\hat{e}^{out} = \hat{p}_{1+}$. The vector

$$
\begin{aligned}
\mathbf{e}_r^{2\omega} &= \hat{e}^{out}.\mathbf{H}^o & (6.6) \\
&= \hat{p}_{1+}.(\hat{p}_{1+}\hat{p}_{1+} - \hat{p}_{1+}R_{12}^p\hat{p}_{1-}) \\
&= \hat{p}_{1+} - R_{12}^p\hat{p}_{1-}.
\end{aligned}
$$

Substituting equation 6.5 and 6.7 into equation 3.33 the SH power that can be measured in reflection can be written as

$$
P_R(2\omega) = \frac{32\pi^3\omega^2}{c^3 A}\sec^2\theta_i \left|(\hat{p}_{1+} - R_{12}^p\hat{p}_{1-}).\chi_s^{(2)} : (\hat{p}_{2-}t_{12}^p)(\hat{p}_{2-}t_{12}^p)\right|^2 P^2(\omega), \qquad (6.7)
$$

in which we consider only the surface SHG without the EFISH contribution therefore the use of $\chi_s^{(2)}$ instead of $\chi_{eff}^{(2)}$.

The incident light is in the x-z plane and the s-polarised light is in the y-plane. At an incident angle θ_i the p-polarised light in medium 1 can be written as

$$
\hat{p}_{1+} = \cos\theta_i(-\hat{x}) + \sin\theta_i\hat{z}
$$

and

$$
\hat{p}_{1-} = \cos\theta_i\hat{x} + \sin\theta_i\hat{z}
$$

$$
\mathbf{e}_r^{2\omega} = \hat{p}_{1+} - R_{12}^p\hat{p}_{1-} = (-R_{12}^p - 1)\cos\theta_i\hat{x} + (1 - R_{12}^p)\sin\theta_i\hat{z} \qquad (6.8)
$$

If the angle of refraction of the fundamental beam at the interface is θ_t we define $\hat{p}_{2-}$ in medium 2 as

$$
\hat{p}_{2-} = \cos\theta_t\hat{x} + \sin\theta_t\hat{z}
$$

The vector $\mathbf{e}_r^\omega$ is written as

$$
\mathbf{e}_r^\omega = \hat{p}_{2-}t_{12}^p = t_{12}^p\cos\theta_t\hat{x} + t_{12}^p\sin\theta_t\hat{z} \qquad (6.9)
$$

Now

$$\mathbf{e}_r^{2\omega} \cdot \chi_s^{(2)} : \mathbf{e}_r^\omega \mathbf{e}_r^\omega = \Gamma_r = [(-R_{12}^p - 1)\cos\theta_i \hat{x} + (1 - R_{12}^p)\sin\theta_i \hat{z}] \cdot \chi_s^{(2)} : [t_{12}^p \cos\theta_t \hat{x} + t_{12}^p \sin\theta_t \hat{z}]^2 . \tag{6.10}$$

For simplicity we drop the subscript "s" of the components of $\chi_s^{(2)}$. The above equation can be expanded as

$$
\begin{aligned}
\Gamma_r &= (-R_{12}^p - 1)\cos\theta_i \chi_{xxx}^{(2)} (t_{12}^p \cos\theta_t)^2 \\
&+ 2(-R_{12}^p - 1)\cos\theta_i \chi_{xxz}^{(2)} (t_{12}^p \cos\theta_t)(t_{12}^p \sin\theta_t) \\
&+ (-R_{12}^p - 1)\cos\theta_i \chi_{xzz}^{(2)} (t_{12}^p \sin\theta_t)^2 \\
&+ 2(1 - R_{12}^p)\sin\theta_i \chi_{zxz}^{(2)} (t_{12}^p \cos\theta_t)(t_{12}^p \sin\theta_t) \\
&+ (1 - R_{12}^p)\sin\theta_i \chi_{zzz}^{(2)} (t_{12}^p \sin\theta_t)^2 \\
&+ (1 - R_{12}^p)\sin\theta_i \chi_{zxx}^{(2)} (t_{12}^p \cos\theta_t)^2 ,
\end{aligned}
\tag{6.11}
$$

where $\chi_{xxx}^{(2)}$ to $\chi_{zxx}^{(2)}$ are the time independent components of the second order susceptibility tensor of Si.

The Si(100) surface orientation used in this study has a C_{4v} symmetry and the second order surface tensor is given by [52, 94], therefore

$$\chi_{xxx}^{(2)} = \chi_{zxz}^{(2)} = \chi_{xzz}^{(2)} = 0, \qquad \chi_{xxz}^{(2)} = d_{15}, \quad \chi_{zxx}^{(2)} = d_{31} \quad \text{and} \quad \chi_{zzz}^{(2)} = d_{33}.$$

The equation for Γ_r is reduced to

$$
\begin{aligned}
\Gamma_r &= 2(-R_{12}^p - 1)\cos\theta_i d_{15} (t_{12}^p \cos\theta_t)(t_{12}^p \sin\theta_t) \\
&+ (1 - R_{12}^p)\sin\theta_i d_{31} (t_{12}^p \cos\theta_t)^2 \\
&+ (1 - R_{12}^p)\sin\theta_i d_{33} (t_{12}^p \sin\theta_t)^2
\end{aligned}
\tag{6.12}
$$

The SH power generated in reflection can be written as

$$P_R(2\omega) = \frac{32\pi^3 \omega^2}{c^3 A} \sec^2\theta_i |\Gamma_r|^2 P^2(\omega). \tag{6.13}$$

Now we discuss the SH power generated in transmission for p-polarised light only. According to Mizrahi and Sipe [54] the vector $\mathbf{e}^{2\omega}$ is similar for transmission and reflection therefore $\mathbf{e}_r^{2\omega} = \mathbf{e}_t^{2\omega}$. The electric field at $z = 0^-$ for p-polarised incident light in transmission is given by

$$
\begin{aligned}
E^\omega(x, z = 0^-) &= [(\hat{p}_{2+}t_{12}^p - \hat{p}_{2-}r_{21}^p t_{12}^p)\exp(-\alpha z/2)E_{in}^p]\exp(ipx) & (6.14)\\
&= [(\hat{p}_{2+} - r_{21}^p \hat{p}_{2-})t_{12}^p\exp(-\alpha z/2))]\,\hat{p}_{1+}.\hat{p}_{1+}\frac{E_{in}^p}{|E_{in}|}|E_{in}|\exp(ipx)\\
&= [(\hat{p}_{2+} - r_{21}^p \hat{p}_{2-})t_{12}^p\exp(-\alpha z/2)]\,\hat{p}_{1+}.\hat{e}_{in}|E_{in}|\exp(ipx)\\
&= \mathbf{e}_t^\omega|E_{in}|\exp(ipx)
\end{aligned}
$$

where $\mathbf{e}_t^\omega = [(\hat{p}_{2+} - r_{21}^p \hat{p}_{2-})t_{12}^p\exp(-\alpha z/2)]\hat{p}_{1+}.\hat{e}^{in}$, and $\exp(-\alpha z/2)$ is the scaling factor due to absorption of the fundamental beam in medium 2, α is the absorption coefficient and z is the interaction length of the incident beam and the medium. The above equation is the sum of the transmitted fundamental beam to the second surface and a contribution of the fundamental reflected beam from the second interface. Consider the expression

$$
\mathbf{e}_t^{2\omega}.\chi^{(2)} : \mathbf{e}_t^\omega\mathbf{e}_t^\omega = \Gamma_t
$$

in the absence of the absorption factor $\exp(-\alpha z/2)$ will be

$$
\Gamma_t = (\hat{p}_{1+} - R_{12}^p\hat{p}_{1-}).\chi^{(2)} : [(\hat{p}_{2+} - r_{21}^p\hat{p}_{2-})t_{12}^p]^2 \tag{6.15}
$$

$$
\Gamma_t = [(-R_{12}^p - 1)\cos\theta_i\hat{x} + (1 - R_{12}^p)\sin\theta_i\hat{z}].\chi^{(2)} : [(-r_{21}^p - 1)t_{12}^p\cos\theta_t\hat{x} + (1 - r_{21}^p)t_{12}^p\sin\theta_t\hat{z}]^2
$$
$$
\tag{6.16}
$$

$$
\begin{aligned}
\Gamma_t \;=\; & (-R_{12}^p - 1)\cos\theta_i \chi_{xxx}^{(2)}((-r_{21}^p - 1)t_{12}^p\cos\theta_t)^2 && (6.17)\\
+\; & 2(-R_{12}^p - 1)\cos\theta_i \chi_{xxz}^{(2)}((-r_{21}^p - 1)t_{12}^p\cos\theta_t)((1 - r_{21}^p)t_{12}^p\sin\theta_t)\\
+\; & (1 - R_{12}^p)\sin\theta_i \chi_{zxx}^{(2)}((-r_{21}^p - 1)t_{12}^p\cos\theta_t)^2\\
+\; & 2(1 - R_{12}^p)\sin\theta_i \chi_{zxz}^{(2)}((-r_{21}^p - 1)t_{12}^p\cos\theta_t)((1 - r_{21}^p)t_{12}^p\sin\theta_t)\\
+\; & (1 - R_{12}^p)\sin\theta_i \chi_{zzz}^{(2)}((1 - r_{21}^p)t_{12}^p\sin\theta_t)^2\\
+\; & (-R_{12}^p - 1)\cos\theta_i \chi_{xzz}^{(2)}((1 - r_{21}^p)t_{12}^p\sin\theta_t)^2
\end{aligned}
$$

Considering nonzero tensor from surface susceptibility tensor of Si(100) Γ_t becomes

$$
\begin{aligned}
\Gamma_t \;=\; & 2(-R_{12}^p - 1)\cos\theta_i d_{15}((-r_{21}^p - 1)t_{12}^p\cos\theta_t)((1 - r_{21}^p)t_{12}^p\sin\theta_t) && (6.18)\\
+\; & (1 - R_{12}^p)\sin\theta_i d_{31}((-r_{21}^p - 1)t_{12}^p\cos\theta_t)^2\\
+\; & (1 - R_{12}^p)\sin\theta_i d_{33}((1 - r_{21}^p)t_{12}^p\sin\theta_t)^2
\end{aligned}
$$

The SH power in transmission can be expressed as

$$
P_T(2\omega) = \frac{32\pi^3\omega^2}{c^3 A}\sec^2\theta_i \exp(-2\alpha z)\,|\Gamma_t|^2\,P^2(\omega). \tag{6.19}
$$

The SH power in reflection and transmission depends on the Fresnel factors and the electric field vectors responsible for inducing SH signal at each interface.

6.5 Time Dependent SH Response in Transmission and Reflection

In this section we discuss time dependent EFISH measurements performed in reflection and transmission using free standing Si membrane.

6.5.1 Time Dependent SH Response in Reflection

Figure 5.5 shows time dependent SH response measured in reflection from a Si membrane at different incident laser powers. The time dependent traces from Si/SiO_2 interface shown in Figure 5.5 reproduce results reported by other researchers using bulk Si samples [2, 3, 36, 41, 42, 75, 76, 95]. The SH response curves are interpreted consistently as arising from EFISH process. The high intensities incident on the sample allow nonlinear processes such as multiphoton absorption to occur near the Si/SiO_2 first interface and induce charge transfer which establishes an interfacial electric field. For each SH response trace the incident intensity is constant throughout beam exposure therefore the time dependence arises from transfer of charges which subsequently alter the effective interfacial susceptibility tensor. The SH responses are therefore a direct measure of charge transfer and the change in the susceptibility tensor. The rise in SH signal upon irradiation is as a result of the increase in the interfacial electric field established by electron transfer process.

According to Mihaychuk et. al. [36], the time dependent SH response curves in Figure 5.5 can be numerically reproduced by a bi-exponential function

$$I^{2\omega}(t) \propto [1 + a_1 \exp(-t/\tau_1) + a_2 \exp(-t/\tau_2)]^2 \qquad (6.20)$$

where a_1, $a_2 < 0$ and τ_1, τ_2 are time constants. Equation 6.20 is a superposition of two processes which are electron injection into the oxide layer (process one) with time constant τ_1 and electron trap generation (process two) with time constant τ_2 [36, 41]. Electron injection or trap ionization is a reversible process while the trap generation process is irreversible [85]. The time constants depends on the incident peak intensity as well as the density of available trap

sites in the sample [36, 85]. The SH responses shown in Figure 5.5 are dominated by electron transfer across the interface according to previously published results [41, 42, 76]. Hole transfer across the interface will induce an opposing electric field at the interface and cause a decline in the temporal SH response curves. Higher peak intensities (> 45 GW/cm^2 [41]) are needed to observe hole transfer. In the experiments presented here the effects of hole transfer were not observed therefore it is assumed to be negligible in the interpretation of the results.

Table 6.1: The time constants τ_1 and τ_2 as extracted from the numerical data fit in Figure 5.5 using equation 6.20.

Incident Power (mW)	Intensity (GW/cm^2)	Time constant τ_1 (s)	Time constant τ_2 (s)
50	22	~ 1100	~ 12100
100	44	338 ± 68	1573 ± 92
150	68	42 ± 2	287 ± 7
200	88	30.1 ± 0.5	183 ± 5

The incident powers indicated in Tables 6.1 and 6.2 are used for reference with Figures 5.5 and 5.6 respectively. The incident powers correspond to the average powers measured before the incident light interacts with the sample (relative power: 100 %). The intensities are calculated using 100 % of the incident intensities for Table 6.1 which corresponds to the actual intensity probing interface one for SHG in reflection. The intensities in Table 6.2 are calculated using $\sim$ 42 % of the incident intensities which we assume to correspond to the local intensity probing interface two for SHG in transmission. The incident intensities are calculated using the peak pulse powers and the value for beam waist on the sample extracted in Figure 6.1 as peak pulse power divided by area of focussed beam spot on the sample. The peak pulse power is calculated as average power/(repetition rate $\times$ pulse duration), values as listed in Table 4.1. The Gaussian property of the focussed beam and the angle of incidence at each interface are taken into account.

The time constants for Figure 5.5 are shown in Table 6.1 for different incident intensities/laser powers. The time constants τ_1 and τ_2 are dependent on the incident laser intensity I and follow the power law $1/\tau_i \propto I^{n_i}$. The value n indicates the number of photons required for multiphoton injection of electrons from Si to SiO$_2$. Figure 6.9 shows the relationship of the time constants and incident intensity on a double logarithmic plot. The extracted values of n_i
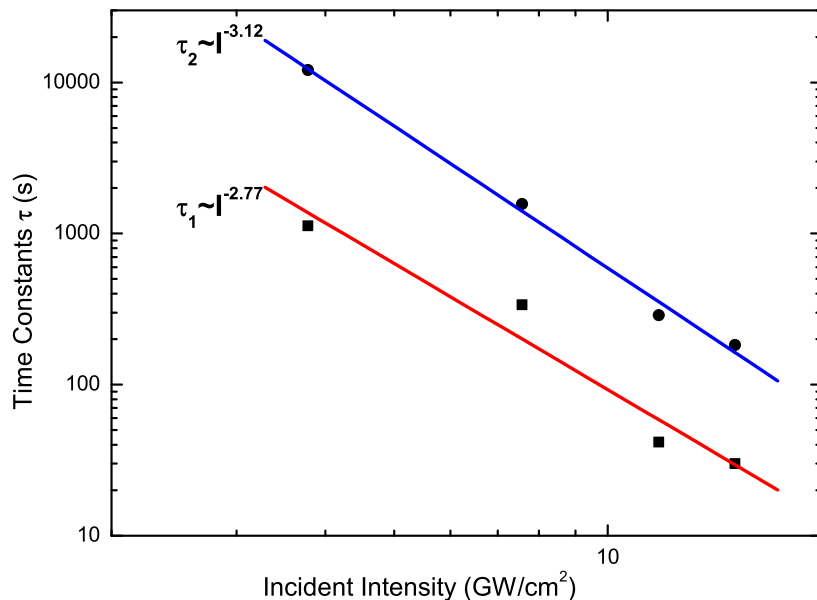
Figure 6.9: The relationship between time constants and incident intensity on a double loga-rithmic plot for SH response in reflection as extracted from numerical data fit of Figure 5.5.

shown on Figure 6.9 are $n_1 = 2.8 \pm 0.4$ and $n_2 = 3.1 \pm 0.2$. The values are in good agreement with literature values obtained from other researchers such as $n_1 = 2.8 \pm 0.2$, and $n_2 = 2.5 \pm 0.3$ [36, 75], and Scheidt et. al. [41] obtained $n_1 = 2.9$ and $n_2 = 2.5$. The results confirm that charge injection and trapping in our SH response for reflection measurements occur through a third-order nonlinear process in which three photons are required to inject electrons from silicon to the oxide. Clearly the SH response measured in reflection is dominated by nonlinear absorption of three photons to inject electrons into the oxide.

6.5.2   Time Dependent SH Response in Transmission

The SH signal in transmission measured from Si membranes is observed for the first time in this study. The SH response in transmission is found to be time dependent as illustrated by results of Figure 5.6. The time evolution is qualitatively similar to that of reflection measurements. There are apparent differences such as rise time and SH yield but the signals show a similar trend of increasing over several minutes of irradiation and reaches a steady state at later times. The time dependent SH response in transmission can therefore be explained in a similar way as the SH response in reflection using a well established EFISH picture as described in Section 6.5.1.

The temporal evolution of the SH signal measured in transmission is attributed to multiphoton injection of electrons from silicon into the SiO_2 conduction band at the second interface followed by electron trapping in the SiO_2 of the second interface. The photoinjection of electrons to the oxide establishes an interfacial electric field at the second interface and this in turn increases the effective nonlinear susceptibility tensor at the interface which is directly measured by SH signals in transmission. The SH signals measured in transmission reaches a steady state after irradiating the sample for several minutes with high incident laser powers. The steady state indicates that the rate of populating or ionizing trap sites is equal to the detrapping rate of charges from trap sites to recombine with holes. As before it is assumed that hole dynamics do not play a significant role in our results. Figure 5.6 curves are a convolution of a fast process of electron injection into trap sites and a slower process of trap generation, as described by equation 6.20, similar to SH response curves in reflection.

Table 6.2: The time constants τ_1 and τ_2 as extracted from the numerical data fit in Figure 5.6 using equation 6.20.

| Incident Power (mW)	Intensity (GW/cm^2)	Time constant τ_1 (s)	Time constant τ_2 (s)
50	11	97 $\pm$ 23	549 $\pm$ 98
80	18	41 $\pm$ 12	282 $\pm$ 15
100	22	17.6$\pm$ 0.6	150 $\pm$ 4
120	28	14.6 $\pm$ 0.7	117 $\pm$ 3
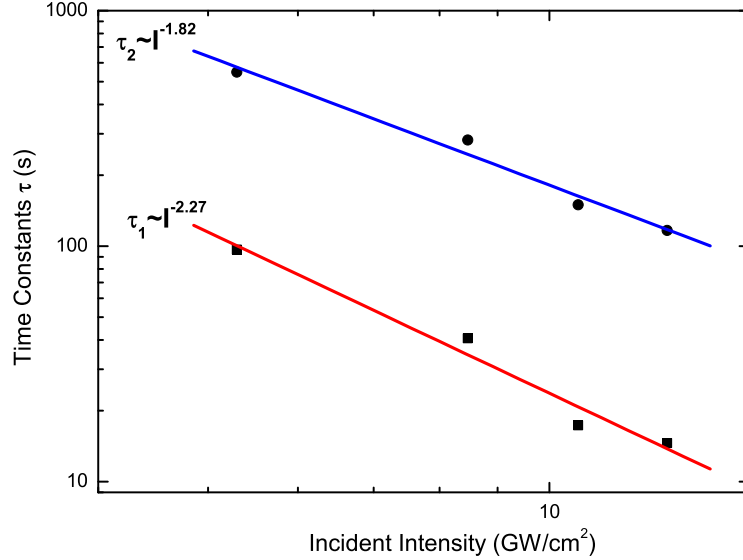
Figure 6.10: The relationship between time constants and incident intensity on a double logarithmic plot for SH response in transmission as extracted from numerical data fit of Figure 5.6.

Table 6.2 shows time constants for SH response in transmission for different incident intensities as extracted from numerical data fit of Figure 5.6. The intensities shown are calculated by assuming that all the fundamental beam that reaches interface two contributes to SH signals in transmission. The time constants are much smaller than those obtained in reflection. Figure 6.10 shows a plot of the time constants and incident intensities from Table 6.2 on a double logarithmic scale. The values of n_i were extracted as $n_1 = 2.3 \pm 0.3$ and $n_2 = 1.8 \pm 0.2$. The time constants should depict a third order power law since the SH response measured in transmission is explained by the EFISH process. The values are lower than literature values for EFISH measurements in reflection and results for reflection SH response shown in Section 6.5.1. If the experimental error is taken into consideration then the value of n_1 can take a maximum value of 2.6, which can explain that three photons are required to inject electrons from Si to the oxide and this is consistent with well established EFISH processes. We suggest that the deviation from third order intensity dependence for n_2 to a second order intensity dependence is due to cascaded one- and two photon electron excitation which occur in silicon [3, 77]. This is likely since the fundamental incident laser beam has to propagate a longer

distance in bulk silicon in order to measure the SH signals in transmission. It is likely that any second or higher order processes that will take place in the Si layer, such as multiphoton absorption, self focussing and change in reflectivity as described in Section 3.2 will cause an increasing attenuation of the transmitted fundamental intensity as the laser power increases. This will reduce the values of n_1 and n_2.

6.6 SH Yield in Transmission and Reflection

Figure 5.7 (a)-(d) shows the SH yield measurements in transmission and reflection geometries at different incident laser powers. All the four graphs show that the SH signal measured in transmission is higher than in reflection. Figure 6.11 shows a comparison of the SH response measured in transmission and reflection at the same incident laser power of 100 mW. The SH signal measured in transmission is always higher than the SH signal in reflection throughout beam exposure. The SH signal in transmission rises faster and quickly reaches a steady-state value compared to the signal measured in reflection.

The transmitted power of the fundamental laser beam to the second interface is lower compared to the incident power at the first interface due to absorption in bulk Si. The beam spot sizes at the first and second interfaces are the same as described in Section 6.1.2 therefore the incident intensity on second interface is less than on the first interface. By applying the well known EFISH equation 3.54 available in literature [2, 41, 93, 96, 97, 98], the SH signal in reflection can be written as

$$I_R^{2\omega}(t) \propto \left| \chi_s^{(2)} + \chi^{(3)} E_1(t) \right|^2 (I_1^\omega)^2, \tag{6.21}$$

where $E_1(t)$ is the interfacial electric field at interface one and I_1^ω is the incident intensity at interface one. The time dependent SH signal in transmission can be written as

$$I_T^{2\omega}(t) \propto \left| \chi_s^{(2)} + \chi^{(3)} E_2(t) \right|^2 (a I_1^\omega)^2, \tag{6.22}$$

where $E_2(t)$ is the interfacial electric field at interface two and a is the absorption factor which is less than one. Here we assume that the fundamental beam intensity incident on the
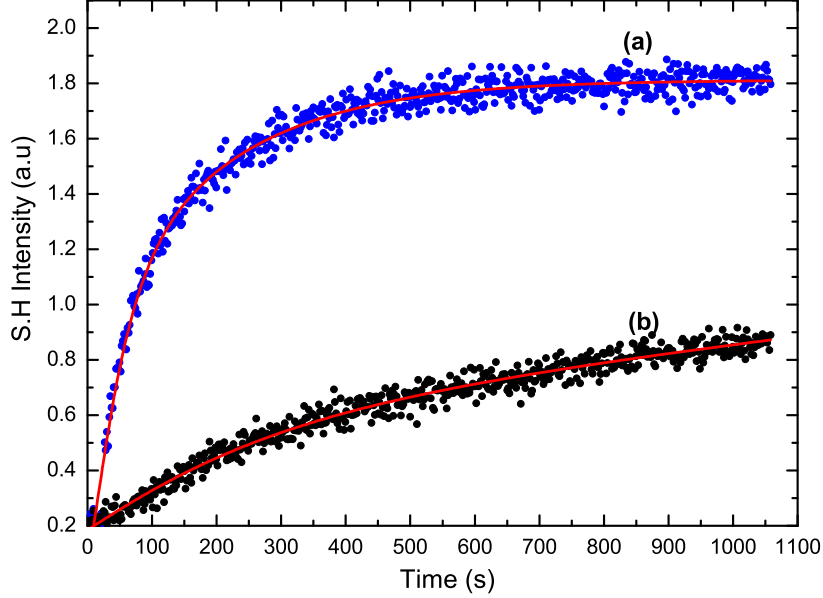
Figure 6.11: A comparison of the time dependent SH response measured in (a) transmission and (b) reflection at the same incident power of 100 mW.

first and second interfaces contributes to SH signals measured in reflection and transmission respectively. From the time dependent traces measured in transmission and reflection shown in Figures 5.5 and 5.6 it is likely that $E_2(t) > E_1(t)$.

The SH signal yield measured in transmission is approximately three times greater than the SH yield measured in reflection using experimental data of Figure 5.7. To explain the experimental results for the SH yield in the two detection geometries (Figure 5.7) we apply the SH model described in Section 6.4. The model applies to the membranes since the incident intensity that reaches interface two is sufficient to induce SHG as shown from the results obtained in this study. The ratio of SH powers in transmission and reflection can be found by dividing equations 6.13 and 6.19 such that

$$\text{Ratio} = \frac{P_T(2\omega)}{P_R(2\omega)} = \frac{|\Gamma_t|^2 e^{-2\alpha z}}{|\Gamma_r|^2} \tag{6.23}$$

The expressions for Γ_t and Γ_r were derived in Section 6.4 using the surface second order

susceptibility tensor of Si(100). The factor $e^{-2\alpha z}$ accounts for the component of the incident light that is absorbed in bulk Si during propagation in the medium to the second interface. For a thick, absorbing media all the fundamental beam can be completely absorbed in bulk material therefore no light will interact with the second interface and no SH signal can be detected in transmission.

In the absence of any charge transfer across the Si/SiO$_2$ interface SHG occurs from surface atoms were symmetry is broken. As a first step and proof of principle we consider only surface SHG in the absence of the interfacial electric field. We apply the model developed in this study and the known surface second order susceptibility tensor of Si(100) to compare the magnitude of the SH signals measured in transmission and reflection. We start with a simple case in which we assume that the three non-zero surface second order tensor components are equal that is $d_{15} = d_{31} = d_{33}$. Figure 6.12 shows a plot of the simple case for SH power in transmission and reflection with incident angle of the fundamental beam. The dotted curve indicated (b) represent the SH signal in transmission when absorption of the fundamental beam in bulk Si is considered. From the plots of Figure 6.12 (at 40° angle of incidence) the SH power in transmission is higher than in reflection in the presence or absence of absorption of the fundamental beam.

If the values for surface second order tensor components of Si(100) are different this can give rise to a dramatic change in the SH power measured in transmission or reflection. According to Hollering et. al. [94] the relative magnitude of the surface tensor elements of Si(100) are $d_{15} = 46$, $d_{31} = 14$ and $d_{33} = 1$. Using these values the SH power in transmission and reflection were plotted against the incident angle as shown in Figure 6.13. The depletion of the incident beam due to absorption was taken into account for SHG in transmission. Clearly, the SH power in transmission is greater than in reflection for most of the incident angles despite the depletion of the incident beam. The SH signal in transmission is about four times greater than the SH signals in reflection at 40° angle of incidence. The results of Figure 6.13 derived from the model developed in this study confirm that the SH power in transmission is greater than the SH power in reflection for surface SHG in the absence of charge transfer. The results of Figure 6.13 is the first powerful step to confirm results obtained in this study.
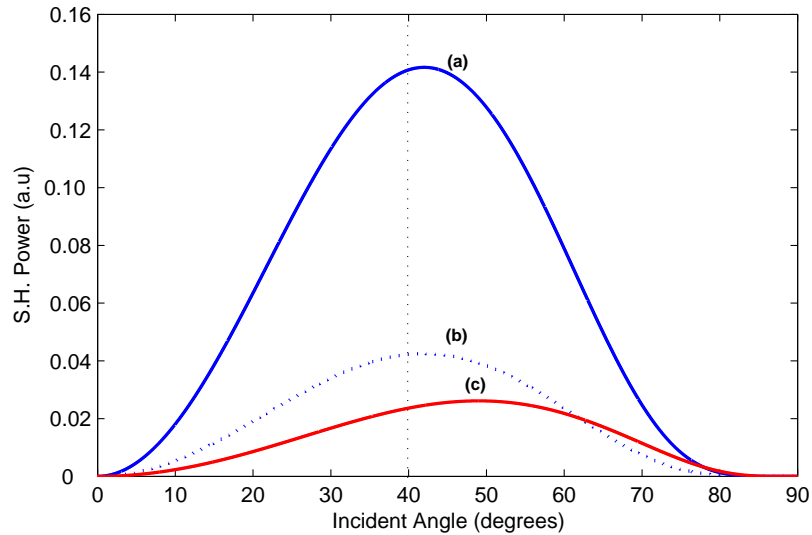
Figure 6.12: The plots of SH power versus the incident angle (a) in transmission without absorption of incident beam (b) in transmission with absorption of incident beam included (c) in reflection. The tensor components were assumed to have the same value that is $d_{15} = d_{31} = d_{33} = 1$.
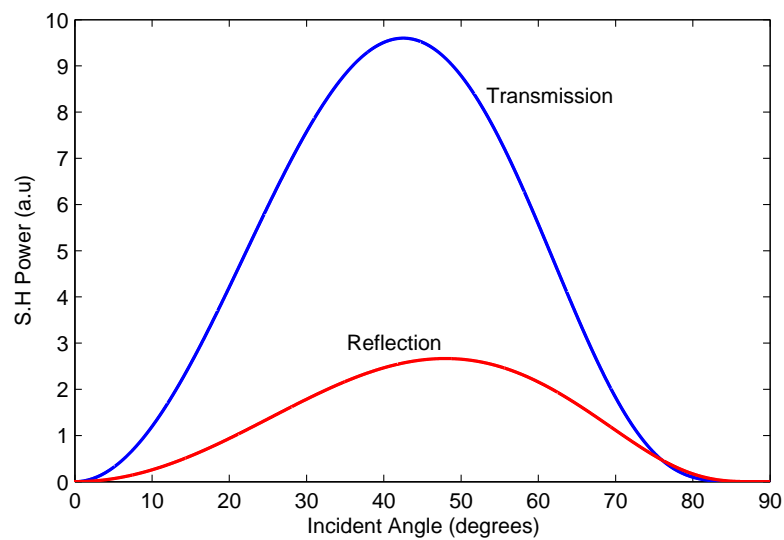
Figure 6.13: Variation of the SH power in reflection and transmission in the presence of absorption of the fundamental beam for relative magnitudes of surface tensor values $d_{15} = 46$, $d_{31} = 14$ and $d_{33} = 1$.

We propose two suggestions for the SHG measurements in the presence of interfacial electric field across the interface. In the presence of sufficient charge transfer across the Si/SiO$_2$ interface an interfacial electric field is established and the SHG is allowed through the EFISH process. The interfacial electric field is orthogonal to the sample surface in the z-direction as described in Section 6.3. We suggest that since the interfacial electric field is time dependent this will give rise to temporal behaviour of the SH signals measured in the two detection geometries without altering the relative magnitudes of the tensor components d_{15}, d_{31} and d_{33}. We assume that any additional symmetry breaking induced by the presence of the interfacial electric field is negligible compared to existing surface symmetry breaking. This implies that throughout beam exposure the SH signal measured in transmission will be higher than in reflection as shown in Figure 6.11. This proposal will be consistent with the results obtained in this study.

The second possibility is to assume that the presence of the interfacial electric field introduce additional symmetry breaking particularly in the direction of the interfacial electric field (z-axis). The effective surface susceptibility tensor can be written as $\chi_{eff}^{(2)} = \chi_s^{(2)} + \chi^{(3)}E(t)$. The $\chi^{(3)}E(t)$ term dominates and the effective second order susceptibility tensor ($\chi_{eff}^{(2)}$) will have more than three non-zero terms. All the effective second order tensor components will have a non-zero value except one tensor component such as $\chi_{xxx}^{(2)} = d_{11}$. The complexity of the term $\chi^{(3)}E(t)$ and the unavailability of tensor components of this term in literature make direct simulations such as plots shown in Figure 6.13 impossible. We can only infer that since our results clearly shows a high SH signal in transmission therefore there exists at least three non-zero tensor components of $\chi_{eff}^{(2)}$ introduced by the presence of the interfacial electric field which make the SH signal in transmission to be higher than in reflection regardless of how complex the susceptibility tensors might appear.

The experimental results do agree qualitatively with simulations based on our model if we apply the second order tensor components, as valid in the absence of the interfacial electric field. We propose that the presence of the interfacial electric field introduces the temporal behaviour in SH signals and additional symmetry breaking, but the latter does not significantly alter the ratio between the SH signal measured in transmission and in reflection. The discussion

presented in this section shows that the results obtained experimentally are consistent with the model for SHG from Si/SiO_2 interfaces, particularly in our case where the fundamental beam is absorbed in bulk Si. The SH signal in transmission is greater than in reflection because of the electric field vectors which generates the SH polarisation in each detection geometry. In reflection only the transmitted fundamental electric field vector into medium 2 contributes to measured SH signals in reflection. In transmission the sum of the incident and reflected electric field vectors on the second interface contributes to SHG in transmission. The magnitude of the total electric field vector for SHG in transmission is therefore greater than total electric field vector for reflection SHG. We suggest that the fast rise of SH signals measured in transmission compared to SH signals in reflection is a corollary of the high SH signals in transmission.

6.7 Time Dependent Reflectivity Measurements

In the following section we discuss experimental results of time dependent reflectivity measurements performed in this study by employing single colour pump-probe technique. The results are reported for the first time in this study. The time dependent reflectivity measured in reflection from bulk n-type Si(111) with native oxide was observed from a weak probe beam. The reflected signal increased with irradiation time of several minutes as shown by results presented in Section 5.4.

The strong pump beam is used to induce nonlinear effects such as charge transfer across the interface through multiphoton absorption of pump photons. The weak probe beam is not focussed on the sample therefore it does not induce any nonlinear effects. The probe beam monitors the small change in reflectivity caused by the interfacial electric field. Both the pump and probe beam spots overlap spatially on the sample.

Most of the research on pump-probe experiments reported in literature [99, 100, 101, 102, 103] are based on time resolved measurements using ultrashort pulses to monitor the change in reflectivity on picosecond time scales. The incident intensities were reported to be lower than the damage threshold of the material to avoid generation of ablation plumes due to fast ionization processes and this will effectively affect the reflectivity of the material as a result

of a creation of plasma mirror and scattering effects [104]. This is formed when free electrons or holes are produced by the pump pulse without the heating of the lattice [13, 104]. At high intensities above the damage threshold the lifetime of the increased reflectivity is in the order of nanoseconds which can be due to structural changes as fast amorphization or melting followed by recrystallization [104].

Most of the time-resolved measurements below the damage threshold showed that the reflectivity of the material decreases with time on picosecond time scales after excitation with a short pulse [100]. This is explained by the generation of free carriers upon irradiating the material with an above band gap ultrashort pulse which subsequently increases the reflectivity of the material. The relaxation of charge carriers during recombination after excitation was reported to be the main contributor in the decrease of the reflectivity over several picoseconds. Although time resolved reflectivity measurements are understood to occur on short time scales in this work we observed a new phenomenon in which the change in reflectivity of $Si(111)/SiO_2$ interface was observed to occur on longer time scales of typically several minutes after onset of irradiating with a continuous train of ultrashort fs laser pulse. Time resolved reflectivity measurements were obtained by delaying either the pump or probe beam and scanning over several delay times. Both the pump and probe beams are stationary (no delay and do not move spatially) for reflectivity measurements presented in this study.

Figure 5.8 shows the change in reflectivity with time. The signal increases slowly with time after several minutes of irradiation. It was observed that if the sample is exposed to the pump beam for a longer time the signal will eventually reach a steady-state as shown in Figure 5.9. The change in reflectivity was only observed in the presence of a focussed pump beam. We suggest that the magnitude of the change in reflectivity and the time the signal takes to reach a steady state depends on the overlap of the pump and probe beams on the sample. If the probe beam is smaller than the pump beam and lies exactly on top of the probe beam the signal should increase faster and reach a steady state much quicker, however the pump beam spot size should be small in order to generate high intensities that are capable of inducing nonlinear effects which are sufficient to be detected by the probe beam.

The observed temporal behaviour of the reflectivity of the material can be caused by ther-

mal effects which can increase the temperature of the material and this in turn affects the reflectivity. It can also be caused by the change in the refractive index of the material upon irradiation caused by charge transfer across the interface. The relative change in reflectivity can be written as [105]

$$\frac{\Delta R}{R} = \frac{1}{R}\frac{\partial R}{\partial T}\Delta T + \frac{1}{R}\frac{\partial R}{\partial n}\Delta n. \tag{6.24}$$

The first term in equation 6.24 represents thermal effects and is negligible in experiments carried out in this study. It has been established that fs lasers with 10 nJ pulse energy and pulse duration (fs) shorter than electron-lattice relaxation times (ps) used in this study cannot cause a significant change of temperature which can activate modification of the interface [85]. Heat transfer from carriers to the lattice occurs on sub-picosecond scale [106], therefore there is fast diffusion of heat into the bulk material before the next pulse arrives on the material. This is most likely since the repetition rate of the laser employed (12 ns) is greater than the time scales of heat diffusion into the lattice. Any incoming pulse will see almost the same material with the same thermal properties as other preceding pulses.

Any long time accumulation of heat caused by the laser which can alter the optical properties of silicon are negligible. The reason is that silicon has good thermal conductivity (149 $\mathrm{Wm^{-1}K^{-1}}$) compared with e.g. aluminium (237 $\mathrm{Wm^{-1}K^{-1}}$) and wood (0.12 $\mathrm{Wm^{-1}K^{-1}}$) [107]. Furthermore, the samples investigated in this study are always in contact with a large aluminium sample holder and any generated heat is transferred to the aluminium holder and will be dissipated. According to Dadap et. al. [108], the temperature rise due to heating caused by fs laser irradiation on Si samples takes few microseconds to reach steady state and the change in temperature was about 7 K. Therefore the increase in the reflectivity of the material which take several minutes to rise cannot be attributed to thermal effects.

Under intense irradiation charge transfer across the $\mathrm{Si/SiO_2}$ interface cause a built-up of a quasi-static ($\omega \approx 0$) interfacial electric field. The photoinduced electric field across the interface changes with time during irradiation and can be denoted by $\mathbf{E}_{int}(t)$. The net electric field produced by the incident light of frequency ω together with the induced dc interfacial electric field can be written as

$$\mathbf{E} = \mathbf{E}_{int}(t) + \mathbf{E}_o\cos(\omega t) \tag{6.25}$$

where $\mathbf{E}_o$ is the amplitude of the incident light wave. For materials exhibiting a non-negligible Kerr effect the third order term $\chi^{(3)}$ is significant with no even orders due to inversion symmetry of the Kerr medium. A complex equation for $\mathbf{P}$ is obtained when equation 6.25 is substituted into equation 3.9. For the dc Kerr effect we can neglect all terms except the linear terms and those in $\chi^{(3)}|\mathbf{E}_{int}(t)|^2\mathbf{E}_o$ [46] then

$$\mathbf{P} \approx \varepsilon_o \left(\chi^{(1)} + 3\chi^{(3)}|\mathbf{E}_{int}(t)|^2 \right) \mathbf{E}_o \cos(\omega t). \tag{6.26}$$

Using the same procedure shown in Section 3.2.4 to derive the nonlinear refractive index, the effective refractive index of the material becomes time dependent due to the time dependent interfacial electric field

$$n(t) = n_o + \kappa \ \mathrm{Re}\{\chi^{(3)}\}|\mathbf{E}_{int}(t)|^2, \tag{6.27}$$

where κ is a constant. The second term in equation 6.27 is Δn which represent the nonlinear change in the refractive index due to the induced electric field.

The reflectivity of the Si/SiO$_2$ system changes because the index of refraction changes. Since the interfacial electric field built-up varies slowly compared to the frequency of the light the optical properties of the material in the region where the electric field is established change according to electro-optic effect as shown in equation 6.27. The change in the refractive index is linearly proportional to the third order susceptibility tensor and the square of the induced electric field. The interfacial electric field is perpendicular to the sample surface or interface and only the refractive index along the direction of the induced electric field changes. For p-polarised probe light, as used in the measurement, the index of refraction of silicon will change with the growing interfacial field due to the Kerr effect and this increases the reflectivity of the interface according to Fresnel equations.

We suggest that the main contribution to change in reflectivity in the observed traces is the change in the refractive index of the material during irradiation caused by the induced electric field, therefore the second term in equation 6.24 cannot be neglected. It is unlikely that the trapped charges in the oxide can change the optical properties of the oxide significantly to cause any observable effects. However, we suggest that the changes are mainly caused by

silicon layers close to the interface since the oxide is optically transparent to the pump and probe beams. The oxide can therefore make a static contribution to the reflectivity which cannot be detected by the experiment [100]. The time dependence in the reflectivity of the $Si(111)/SiO_2$ system is very similar to the time dependence of the EFISH signals. This strongly suggests that the change in the reflectivity is related to charge transfer across the interface and the induced interfacial electric field.
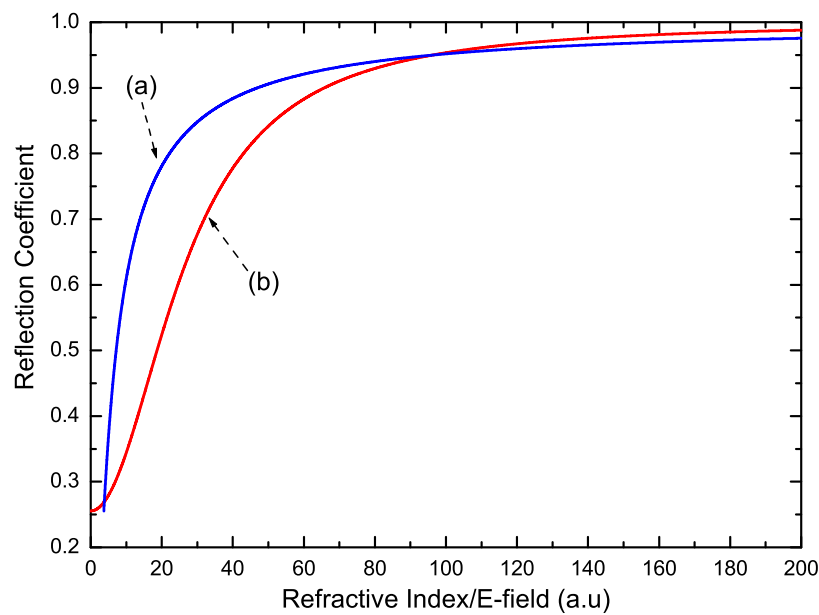
Figure 6.14: The variation of reflection coefficient for p-polarised incident light with (a) refractive index and (b) the interfacial electric field.

Figure 6.14 shows the change in the reflection coefficient with the interfacial electric field and the refractive index of Si. The graph was plotted by assuming an arbitrary increase in the electric field and calculate the corresponding change in the refractive index according to equation 6.27. The reflection coefficient was calculated using the Fresnel equation of reflectance for p-polarised light obtained from [92]. The reflection coefficient plotted in Figure 6.14 shows a nonlinear trend with an increase in the magnitude of the electric field and refractive index. For very small changes in the electric field and the refractive index the relationship with the reflection coefficient can be approximated as linear. This approximation is valid since in our

experiments the change in reflectivity of the material is very small ($\sim$ 12 % after 2500 seconds of irradiation, see Figure 5.9) suggesting that the induced interfacial electric field does not change by a large margin. Therefore, in this regime the experimental data in Figure 5.10 can be fitted using equation 6.20 which was used for EFISH process since in principle, the two processes EFISH and time dependent reflectivity are both linearly dependent on the interfacial electric field caused by the same effect of charge transfer from Si and subsequent trapping in the oxide. If this is done the time constants extracted from Figure 5.10 are given in Table 6.3.

Table 6.3: The time constants τ_1 and τ_2 as extracted from the numerical data fit in Figure 5.10 using equation 6.20.

Incident Power (mW)	Intensity (GW/cm^2)	Time constant τ_1 (s)	Time constant τ_2 (s)
100	40	2835	–
200	80	908	67287
300	120	240	16391
400	160	150	6400

The time constants for time dependent reflectivity shown in Table 6.3 are much larger than those of the time dependent SHG shown in Table 6.1 although the two processes arise from the same phenomena. This is expected since the two processes (reflectivity and SHG) are different and the measurement techniques are also different. This shows that the change in the reflectivity of the material caused by the built-up of interfacial electric field is much slower and smaller compared to the corresponding change in SH signals. However, although the time scales can be different the time constants of the two processes should reveal the same power law as described in Section 6.5.1. The values for n_i, were extracted by plotting the time constants shown in Table 6.3 against the intensity on a double logarithmic plot. The values of n_i are $n_1 = 2.2 \pm 0.3$ and $n_2 = 3.4 \pm 0.1$. The value for n_2 shows that the time dependent reflectivity process is a third order process and charge transfer requires three photons to inject electrons to the oxide. This is in agreement with EFISH process reported in this study as described in Section 6.5.1. The value of n_1 describe a third order process as well.

The time dependent reflectivity arises from the photoinduced electric field caused by charge transfer across the interface. The change in reflectivity observed is much smaller than the SH effects induced by interfacial electric field through EFISH process. We suggest that the
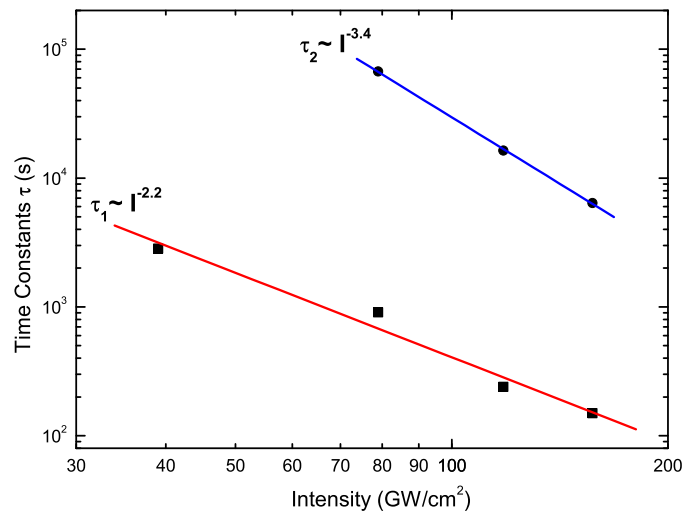
Figure 6.15: The relationship between time constants and incident intensity on a double logarithmic plot for time dependent reflectivity measurements as extracted from numerical data fit of Figure 5.10.

change in reflectivity occurs via the Kerr effect in which the refractive index is proportional to the local intensity of the light on the sample. The Kerr effect becomes time dependent according to equation 6.27. According to literature [46] the Kerr effect is reported to be very small in most nonresonant cases ($\sim 10^{-5}$) since this occurs through the third order process hence high intensities below damage threshold are required to observe a measurable change. In time-resolved measurements reported by Cheville and coworkers [100] using GaAs with oxide layers, the small change (decrease) in reflectivity on picosecond time scales was assigned to an electro-optic contribution in the space charge region due to photoinjected carriers into the oxide. The time dependent reflectivity traces were well pronounced for n-type Si(111) compared to other silicon samples of different orientation and doping type. In EFISH measurements it is well established that Si(111) gives a much stronger SH signal compared to Si(100). This is explained by the difference in atomic configurations of the two sample orientations [11].

Chapter 7

Summary and Conclusion

Electric field induced second harmonic generation as well as pump-probe reflectivity measurements have been demonstrated in this study using near infrared femtosecond laser pulses on native Si/SiO_2 interfaces of moderately p-doped free standing single crystalline Si membranes and bulk n-type Si(111) samples. SHG in transmission from Si membrane is reported for the first time in this study as well as time dependent reflectivity measurements from Si(111) which were observed by use of the pump-probe technique.

There are four main results which are summarised in this chapter and these are: (i) The time dependent second harmonic response in reflection from Si/SiO_2 interfaces of Si membrane were recorded and analysed to compare with previously published results in literature. (ii) The temporal SH response in transmission from Si/SiO_2 interfaces of Si membrane were measured and compared with temporal SH response measured in reflection. (iii) Second harmonic yield measurements in reflection and transmission from Si/SiO_2 interfaces of the membrane were measured at different incident laser powers. The magnitude of the SH signals measured in reflection and in transmission were analysed and compared. (iv) Pump-probe reflectivity measurements from Si/SiO_2 interface of bulk n-type Si(111) were recorded at different incident laser powers and were found to change with time after irradiating the sample with sufficient laser intensities.

The time dependent SH response measured in reflection from Si membrane reproduced similar temporal traces reported in literature. The time dependent SH response is due to the EFISH process, in which electrons are injected by multiphoton absorption of photons into the oxide where some electrons can be trapped. The transfer of electrons establishes a quasi-static interfacial electric field which enhances the SH signal significantly. The traces are dominated by electron transfer based on previously published results. Hole transfer is considered negligible due to low incident intensities employed in this study. The time constants for electron injection and trap generation processes for EFISH measurements in reflection were extracted by fitting the experimental data using a well established numerical model. Using the power law ($1/\tau_i \propto I^{n_i}$), the values $n_1 = 2.8 \pm 0.4$ and $n_2 = 3.1 \pm 0.2$ were obtained. The values of n_1 and n_2 reproduced previously published results and this shows that the photoinjection of charge carriers into the oxide and trap generation process is dominated by three photon process for SH response in reflection.

The SH responses measured in transmission were observed to increase with time during irradiation and reach a steady-state after long time irradiation. The time dependent SH response in transmission qualitatively resembled SH response traces in reflection with deviations in rise time and magnitude of SH response measured. The traces for SH response measured in transmission showed that the measured SH signal originates from charge transfer process at the Si/SiO_2 interface. Therefore the temporal evolution is explained using a well established picture of EFISH process similar to SH measurements in reflection. Using the power law, values of n_i were obtained as $n_1 = 2.3 \pm 0.3$ and $n_2 = 1.8 \pm 0.2$ which shows a third order intensity dependence for the value of n_1. We suggest that the deviation from a pure third order process is caused by other nonlinear processes such as multiphoton absorption, self-focussing and nonlinear change in refractive index which may attenuate or modify the properties of the transmitted beam as it propagates in bulk Si especially when the incident intensity increases. Cascaded one- or two-photon processes which occur in bulk Si can contribute to the deviation.

The magnitude of the SH yield in reflection and transmission was measured at different incident laser powers using a single interface of the membrane. The magnitude of SH signals for the two detection geometries was analysed and compared at each incident laser power. The results

showed that the magnitude of SH signal in transmission is higher than expected and were approximately three times greater than SH yield measured in reflection. It was observed that at low incident laser intensities an EFISH signal could be measured in transmission while there is no measurable SH signal in reflection for the same intensities.

A physical model was developed to explain the results or time dependent SH response and SH yield measurements obtained in transmission and reflection. The first step was to establish the origin of EFISH signals in each detection geometry. Any SH signals measured were generated in silicon by Si atoms close to Si/SiO_2 interface in the region where the interfacial electric field penetrates. The SH signals measured in reflection were found to originate from the first Si/SiO_2 interface of the membrane facing the incident laser beam. The SH signals measured in transmission were found to originate from the second Si/SiO_2 interface on the exit of the incident beam from the membrane. The SH signal generated at interface one is completely absorbed in bulk Si within 100 nm penetration length therefore the SH signals measured in transmission are independent of interface one and bulk silicon contributions.

A model was developed to explain why the magnitude of the SH yield measured in transmission is higher than in reflection geometry. The fundamental electric field vector generating SH in transmission is larger than in the case of SH in reflection. The sum of the incident electric field vector and reflected electric field vector at the second interface generates SH in transmission while in reflection only the transmitted electric field vector at the first interface contributes to SH signals in reflection.

The time constants for the electron injection and trap generation processes extracted from the SH response curves were significantly smaller for the SH response in transmission than for reflection measurements. This indicates that the processes which contributes to the built-up of the interfacial electric field which enhances the SHG are much faster for SHG in transmission than in reflection. We propose that the differences in the time constants are correlated to the low SH signals in reflection from the first interface compared to high SH signals from the transmission geometry. A larger fundamental electric field vector at the second interface causes both a higher SH signal in transmission and a faster built-up of the interfacial electric field.

A pump-probe technique was employed to study the time dependent reflectivity of n-type Si(111)/SiO$_2$ interface. The time dependent reflectivity was investigated at different incident intensities. It was observed that reflectivity measured from a weak probe beam increased with time over several minutes of irradiation and eventually reaches a steady-state after long time irradiation ($\sim$ 30 minutes). The pump beam induced charge transfer across the interface and the probe beam monitors the change in reflectivity caused by charge transfer. Similar time dependent reflectivity response traces were obtained when the fs laser was tuned to a different fundamental wavelength near 800 nm.

The increase in reflectivity is attributed to photoinjection of charge carriers from Si to SiO$_2$ after irradiating the sample and this establishes an interfacial electric field as in EFISH processes. The presence of the interfacial electric field alters the index of refraction of the silicon through the Kerr effect, the change in index being proportional to $\chi^{(3)}$ and the square of the interfacial electric field. Thermal effects which might change the optical properties of the material were ruled out. Using the power law as applied in SHG the values of n_i were extracted with $n_1 = 2.2 \pm 0.3$ and $n_2 = 3.4 \pm 0.1$, the results show that electron injection which dominates in n-type Si and trap generation are third order processes in agreement with EFISH processes.

These novel results which are shown for the first time provide additional information to our understanding of EFISH processes at Si/SiO$_2$ interfaces in particular the mechanisms of charge transfer and trap generation processes and their effects on the photoinduced electric field and optical properties of the material. The results show that second harmonic generation and optical reflectivity measurements are powerful tools to study buried interfaces.

7.1   Outlook

Clearly the results presented in this study have opened new questions for further research. Dynamics of defect creation and charge trapping in transmission can be further explored by using vacuum ultraviolet light sources to create defects and probe the defects using the femtosecond laser. A single photon is required to photoinject charges from Si to the oxide using vacuum ultraviolet light sources compared to multiphoton processes reported in this study.

A tunable light source can be used to investigate how the SH signal in transmission and reflection varies with photon energy. Instead of using a photomultiplier tube to detect the SH signals a sensitive spectrometer can be used and spectral information of bulk resonance lines can be obtained. Phase information can be studied from a spectrograph which can be obtained by interfering the reflected SH signals with transmitted SH signals. The spectral results for the two detection geometries can be compared and information about defect generation and charge trapping can be revealed. Time resolved pump-probe SHG can be carried out to monitor the evolution of the interfacial electric field on short time scales such as picoseconds. This can be done by focussing both pump and probe beams on the sample. Both the pump and probe should generate SH signals and one beam (probe) can be delayed.

SHG in transmission can be investigated in the presence of externally applied bias, and the temporal evolution of the signals can be compared with known traces. The work can be extended to investigate smaller structures such as silicon nanowires, information about the electrical properties of nanowires can be obtained. Preliminary investigations showed that it is possible to obtain SHG from nanowires. The only challenge was that nanowires were easily destroyed by the fs laser. The problem can be overcome by defocussing the laser spot on the sample and the use a laser with a lower repetition rate say 1 kHz instead of 80 MHz.

The time dependent reflectivity investigated by pump-probe technique was obtained using n-type Si(111). The sensitivity of the experiment can be improved and silicon samples of different orientations and doping concentrations can be studied. Instead of using a photomultiplier tube a photon counter can be used. The temporal evolution of the reflectivity signals can be different for samples of different doping concentrations as in EFISH signals. A different laser colour or different polarisation of the probe beam can be used. The sensitivity of the Kerr effect caused by different wavelengths and polarisations of probe light can be investigated. Defects can be photoinduced and the temporal behaviour of the reflectivity signal after irradiation can be studied. Ultrafast time resolved pump-probe technique can be employed by use of fs laser, the change in reflectivity on short time scales can give further information about dynamics of charge transfer and trapping, in particular the establishment of the electric field on a short time scale.

Bibliography

[1] E. D. Palik and G. Ghosh. *Handbook of Optical Constants of Solids.* Academic Press, 1998.

[2] Y. V. White, X. Lu, R. Pasternak, N. H. Tolk, A. Chatterjee, R. D. Schrimpf, D. M. Fleetwood, A. Ueda, and R. Mu. Studies of charge carrier trapping and recombination processes in $Si/SiO_2/MgO$ structures using second-harmonic generation. *Applied Physics Letters*, 88(6):1–3, 2006.

[3] J. Bloch, J. G. Mihaychuk, and H. M. vanDriel. Electron photoinjection from silicon to ultrathin SiO_2 films via ambient oxygen. *Physical Review Letters*, 77(5):920–923, 1996.

[4] M. L. Green, E. P. Gusev, R. Degraeve, and E. L. Garfunkel. Ultrathin ($<$ 4 nm) SiO_2 and Si-O-N gate dielectric layers for silicon microelectronics: Understanding the processing, structure, and physical and electrical limits. *Journal Of Applied Physics*, 90(5):2057–2121, 2001.

[5] D. A. Buchanan. Scaling the gate dielectric: Materials, integration, and reliability. *IBM Journal Of Research And Development*, 43(3):245–264, 1999.

[6] S. Lombardo, J. H. Stathis, B. P. Linder, K. L. Pey, F. Palumbo, and C. H. Tung. Dielectric breakdown mechanisms in gate oxides. *Journal Of Applied Physics*, 98(12), 2005.

[7] T. Scheidt, E. G. Rohwer, H. M. von Bergmann, and H. Stafast. Optical second harmonic imaging: a versatile tool to investigate semiconductor surfaces and interfaces. *European Physical Journal-Applied Physics*, 27(1-3):393–397, 2004.

[8] T. Scheidt, E. G. Rohwer, H. M. V. Bergmann, and H. Stafast. Femtosecond laser diagnostics of thin films, surfaces and interfaces. *South African Journal Of Science*, 101(5-6):267–271, 2005.

[9] G. Lupke. Characterization of semiconductor interfaces by second-harmonic generation. *Surface Science Reports*, 35(3-4):77–161, 1999.

[10] N. Bloembergen, R. K. Chang, S. S. Jha, and C. H. Lee. Optical second-harmonic generation in reflection from media with inversion symmetry. *Physical Review*, 174(3):813–822, 1968.

[11] H. W. K. Tom, T. F. Heinz, and Y. R. Shen. 2nd-harmonic reflection from silicon surfaces and its relation to structural symmetry. *Physical Review Letters*, 51(21):1983–1986, 1983.

[12] T. F. Heinz, M. M. T. Loy, and W. A. Thompson. Study of Si(111) surfaces by optical second-harmonic generation - reconstruction and surface phase-transformation. *Physical Review Letters*, 54(1):63–66, 1985.

[13] G. Lupke, D. J. Bottomley, and H. M. Van Driel. SiO_2/Si interfacial structure on vicinal Si(100) studied with second-harmonic generation. *Physical Review B*, 47(16):10389–10394, 1993.

[14] C. H. Bjorkman, C. E. Shearon, Y. Ma, T. Yasuda, G. Lucovsky, U. Emmerichs, C. Meyer, K. Leo, and H. Kurz. Second-harmonic generation in Si-SiO_2 heterostructures formed by chemical, thermal, and plasma-assisted oxidation and deposition processes. *Journal Of Vacuum Science & Technology A-Vacuum Surfaces And Films*, 11(4):964–970, 1993.

[15] S. T. Cundiff, W. H. Knox, F. H. Baumann, K. W. Evans-Lutterodt, and M. L. Green. Second-harmonic generation at the interface between Si(100) and thin SiO_2 layers. *Journal Of Vacuum Science & Technology A*, 16(3):1730–1734, 1998.

[16] D. Schuhmacher, G. Marowsky, A. A. Fedyanin, T. V. Dolgova, and O. A. Aktsipetrov. Probe of the vicinal Si(111) surface by second harmonic phase spectroscopy. *Materials Science in Semiconductor Processing*, 4(3):51–53, 2001.

[17] C. Meyer, G. Lupke, U. Emmerichs, F. Wolter, H. Kurz, C. H. Bjorkman, and G. Lu-covsky. Electronic-transitions at Si(111)/SiO$_2$ and Si(111)/Si$_3$N$_4$ interfaces studied by optical 2nd-harmonic spectroscopy. *Physical Review Letters*, 74(15):3001–3004, 1995.

[18] W. Daum, H. J. Krause, U. Reichel, and H. Ibach. Identification of strained silicon layers at Si-SiO$_2$ interfaces and clean Si surfaces by nonlinear-optical spectroscopy. *Physical Review Letters*, 71(8):1234–1237, 1993.

[19] C. H. Bjorkman, T. Yasuda, C. E. Shearon, Y. Ma, G. Lucovsky, U. Emmerichs, C. Meyer, K. Leo, and H. Kurz. Influence of surface-roughness on the electrical-properties of Si-SiO$_2$ interfaces and on second-harmonic generation at these interfaces. *Journal Of Vacuum Science & Technology B*, 11(4):1521–1527, 1993.

[20] S. T. Cundiff, W. H. Knox, F. H. Baumann, K. W. EvansLutterodt, M. T. Tang, M. L. Green, and H. M. vanDriel. Si/SiO$_2$ interface roughness: Comparison between surface second harmonic generation and X-ray scattering. *Applied Physics Letters*, 70(11):1414–1416, 1997.

[21] M. A. Verheijen, C. W. vanHasselt, and T. Rasing. Optical 2nd harmonic-generation study of vicinal Si(111) surfaces. *Surface Science*, 251:467–471, 1991.

[22] S. A. Mitchell, T. R. Ward, D. D. M. Wayner, and G. P. Lopinski. Charge trapping at chemically modified Si(111) surfaces studied by optical second harmonic generation. *Journal Of Physical Chemistry B*, 106(38):9873–9882, 2002.

[23] S. Bergfeld, B. Braunschweig, and W. Daum. Nonlinear optical spectroscopy of suboxides at oxidized Si(111) interfaces. *Physical Review Letters*, 93(9):1–4, 2004.

[24] U. Emmerichs, C. Meyer, H. J. Bakker, F. Wolter, H. Kurz, G. Lucovsky, C. E. Bjorkman, T. Yasuda, Y. Ma, Z. Jing, and J. L. Whitten. Optical second-harmonic generation - a probe of atomic-structure and bonding at Si-SiO$_2$ interfaces, and other chemically-modified Si surfaces. *Journal Of Vacuum Science & Technology B*, 12(4):2484–2492, 1994.

[25] U. Emmerichs, C. Meyer, H. J. Bakker, H. Kurz, C. H. Bjorkman, C. E. Shearon, Y. Mao, T. Yasuda, Z. Jing, G. Lucovsky, and J. L. Whitten. Second-harmonic response of chemically-modified vicinal Si(111) surfaces. *Physical Review B*, 50(8):5506–5511, 1994.

[26] H. Hirayama, F. Ito, and K. Watanabe. Effect of hydrogen annealing on second-harmonic generation from SiO$_2$/Si(111) interfaces. *Journal Of Vacuum Science & Technology A*, 13(3):750–752, 1995.

[27] S. A. Mitchell, R. Boukherroub, and S. Anderson. Second harmonic generation at chemically modified Si(111) surfaces. *Journal Of Physical Chemistry B*, 104(32):7668–7676, 2000.

[28] H. Hirayama and K. Watanabe. Annealing effect on native-oxide/Si(111) interfaces studied by second-harmonic generation. *Physical Review B*, 51(20):14717–14720, 1995.

[29] F. Ito and H. Hirayama. Second-harmonic generation from SiO$_2$/Si(111) interfaces. *Physical Review B*, 50(15):11208–11211, 1994.

[30] C. W. van Hasselt, E. Mateman, M. A. C. Devillers, Th. Rasing, A. A. Fedyanin, E. D. Mishina, O. A. Aktsipetrov, and J. C. Jans. Oxide-thickness dependence of second harmonic generation from thick thermal oxides on Si(111). *Surface Science*, 331-333(2):1367–1371, 1995.

[31] C. Meyer, G. Lupke, Z. G. Lu, A. Golz, H. Kurz, and G. Lucovsky. Nonlinear optical spectroscopy of Si-heterostructure interfaces. *Journal Of Vacuum Science & Technology B*, 14(4):3107–3112, 1996.

[32] D. Lim, M. C. Downer, and J. G. Ekerdt. Second-harmonic spectroscopy of bulk boron-doped Si(001). *Applied Physics Letters*, 77(2):181–183, 2000.

[33] S. A. Mitchell, M. Mehendale, D. M. Villeneuve, and R. Boukherroub. Second harmonic generation spectroscopy of chemically modified Si(111) surfaces. *Surface Science*, 488(3):367–378, 2001.

[34] O. A. Aktsipetrov, A. A. Fedyanin, E. D. Mishina, A. N. Rubtsov, C. W. van Hasselt, M. A. C. Devillers, and Th. Rasing. Probing the silicon-silicon oxide interface of

Si(111)-SiO$_2$-Cr MOS structures by DC-electric-field-induced second harmonic generation. *Surface Science*, 352-354:1033–1037, 1996.

[35] K. A. Peterson and D. J. Kane. Electric-field-induced second-harmonic generation in GaN devices. *Optics Letters*, 26(7):438–440, 2001.

[36] T. G. Mihaychuk, J. Bloch, Y. Liu, and H. M. van Driel. Time-dependent second-harmonic generation from the Si-SiO$_2$ interface induced by charge transfer. *Optics Letters*, 20:2063–5, 1995.

[37] N. Shamir, J. G. Mihaychuk, and H. M. vanDriel. Transient charging and slow trapping in ultrathin SiO$_2$ films on Si during electron bombardment. *Journal Of Vacuum Science & Technology A-Vacuum Surfaces And Films*, 15(4):2081–2084, 1997.

[38] N. H. Tolk, M. L. Alles, R. Pasternak, X. Lu, R. D. Schrimpf, D. M. Fleetwood, R. P. Dolan, and R. W. Standley. Oxide interface studies using second harmonic generation. *Microelectronic Engineering*, 84(9-10):2089–2092, 2007.

[39] V. Fomenko and E. Borguet. Combined electron-hole dynamics at UV-irradiated ultrathin Si-SiO$_2$ interfaces probed by second harmonic generation. *Physical Review B*, 68(8):1–4, 2003.

[40] T. Scheidt, E. G. Rohwer, H. M. von Bergmann, and H. Stafast. Ultraviolet pulse laser induced modifications of native silicon/silica interfaces analyzed by optical second harmonic generation. *Journal Of Applied Physics*, 100:1–6, 2006.

[41] T. Scheidt, E. G. Rohwer, H. M. von Bergmann, and H. Stafast. Charge-carrier dynamics and trap generation in native Si/SiO$_2$ interfaces probed by optical second-harmonic generation. *Physical Review B*, 69(16):1–8, 2004.

[42] T. Scheidt, E. G. Rohwer, P. Neethling, H. M. von Bergmann, and H. Stafast. Ionization and shielding of interface states in native p$^{(+)}$-Si/SiO$_2$ probed by electric field induced second harmonic generation. *Journal Of Applied Physics*, 104(8):1–8, 2008.

[43] P.N Butcher and D Cotter. *The Elements of Nonlinear Optics*. Cambridge University Press, 1990.

[44] R.W. Boyd. *Nonlinear Optics.* Springer, 1992.

[45] P-F Brevet. *Surface Second Harmonic Generation.* Presses polytechniques et universitaires romandes, 1997.

[46] G.S. He and S.H. Liu. *Physics of Nonlinear Optics.* World Scientific Publishing, 1999.

[47] R.L. Sutherland. *Handbook of Nonlinear Optics.* Marcel Dekker, Inc., 2003.

[48] R. M. Corn and D. A. Higgins. Optical second harmonic generation as a probe of surface chemistry. *Chemical Review*, 94:107–125, 1994.

[49] Andrews D.L. and Demidov A.A. *An Introduction to Laser Spectroscopy.* Plenum Press, 1995.

[50] H. Cao, J. Y. Wu, H. C. Ong, J. Y. Dai, and R. P. H. Chang. Second harmonic generation in laser ablated zinc oxide thin films. *Applied Physics Letters*, 73(5):572–574, 1998.

[51] C. Y. Liu, B. P. Zhang, N. T. Binh, and Y. Segawa. Second harmonic generation in ZnO thin films fabricated by metalorganic chemical vapor deposition. *Optics Communications*, 237(1-3):65–70, 2004.

[52] J. E. Sipe, D. J. Moss, and H. M. van Driel. Phenomenological theory of optical second- and third-harmonic generation from cubic centrosymmetric crystals. *Journal Of The American Physical Society - Physical Review B*, 35(3):1129–1141, 1987.

[53] J. E. Sipe. New green-function formalism for surface optics. *Journal Of The Optical Society Of America B-Optical Physics*, 4(4):481–489, 1987.

[54] V. Mizrahi and J. E. Sipe. Phenomenological treatment of surface 2nd-harmonic generation. *Journal Of The Optical Society Of America B-Optical Physics*, 5(3):660–667, 1988.

[55] V. Raghunathan, R. Shori, O. M. Stafsudd, and B. Jalali. Nonlinear absorption in silicon and the prospects of mid-infrared silicon Raman lasers. *Physica Status Solidi A-Applications And Materials Science*, 203(5):38–40, 2006.

[56] R. DeSalvo, M. Sheikbahae, A. A. Said, D. J. Hagan, and E. W. Vanstryland. Z-scan measurements of the anisotropy of nonlinear refraction and absorption in crystals. *Optics Letters*, 18(3):194–196, 1993.

[57] R. DeSalvo, A. A. Said, D. J. Hagan, E. W. VanStryland, and M. SheikBahae. Infrared to ultraviolet measurements of two-photon absorption and n(2) in wide bandgap solids. *IEEE Journal Of Quantum Electronics*, 32(8):1324–1333, 1996.

[58] P.W. Milonni and J.H. Eberly. *Lasers.* Wiley Interscience, 1988.

[59] C. H. Kwak, Y. L. Lee, and S. G. Kim. Analysis of asymmetric Z-scan measurement for large optical nonlinearities in an amorphous AS_2S_3 thin film. *Journal Of The Optical Society Of America B-Optical Physics*, 16(4):600–604, 1999.

[60] M. Samoc, A. Samoc, B. Luther-Davies, Z. N. Bao, and L. P. Yu. Femtosecond Z-scan and degenerate four-wave mixing measurements of real and imaginary parts of the third-order nonlinearity of soluble conjugated polymers. *Journal Of The Optical Society Of America B-Optical Physics*, 15(2):817–825, 1998.

[61] M. SheikBahae, A. A. Said, T. H. Wei, D. J. Hagan, and E. W. Vanstryland. Sensitive measurement of optical nonlinearities using a single beam. *IEEE Journal Of Quantum Electronics*, 26(4):760–769, 1990.

[62] M. SheikBahae, A. A. Said, T. H. Wei, Y. Y. Wu, D. J. Hagan, M. J. Soileau, and E. W. Vanstryland. Z-scan - a simple and sensitive technique for nonlinear refraction measurements. *Nonlinear Optical Properties Of Materials*, 1148:41–51, 1990.

[63] J. Wang, M. Sheikbahae, A. A. Said, D. J. Hagan, and E. W. Vanstryland. Time-resolved Z-scan measurements of optical nonlinearities. *Journal Of The Optical Society Of America B-Optical Physics*, 11(6):1009–1017, 1994.

[64] J. W. Wu and F. G. Luo. Ultrafast femtosecond all-optical modulation through nondegenerate two-photon absorption in silicon-on-insulator waveguides. *Journal Of Russian Laser Research*, 29(5):490–496, 2008.

[65] M. Yin, H. P. Li, S. H. Tang, and W. Ji. Determination of nonlinear absorption and refraction by single Z-scan method. *Applied Physics B-Lasers And Optics*, 70(4):587–591, 2000.

[66] M. Kyoung and M. Lee. Nonlinear absorption and refractive index measurements of silver nanorods by the Z-scan technique. *Optics Communications*, 171(1-3):145–148, 1999.

[67] L. Yang, R. Dorsinville, Q. Z. Wang, P. X. Ye, R. R. Alfano, R. Zamboni, and C. Taliani. Excited-state nonlinearity in polythiophene thin-films investigated by the z-scan technique. *Optics Letters*, 17(5):323–325, 1992.

[68] R. de Nalda, R. del Coso, J Requejo-Isidro, J Olivares, A Suarez-Garcia, J Solis, and C.N. Afonso. Limits to the determination of the nonlinear refractive index by the Z-scan method. *Journal of Optical Society of America B*, 19(2):289–296, 2002.

[69] M. Dinu, F. Quochi, and H. Garcia. Third-order nonlinearities in silicon at telecom wavelengths. *Applied Physics Letters*, 82(18):2954–2956, 2003.

[70] A. D. Bristow, N. Rotenberg, and H. M. van Driel. Two-photon absorption and Kerr coefficients of silicon for 850-2200 nm. *Applied Physics Letters*, 90(19):1–3, 2007.

[71] F. Smektala, C. Quemard, V. Couderc, and A. Barthelemy. Non-linear optical properties of chalcogenide glasses measured by Z-scan. *Journal Of Non-Crystalline Solids*, 274(1-3):232–237, 2000.

[72] P.P. Banerjee. *Nonlinear Optics: Theory, Numerical Modeling and Applications*. Marcel Dekker, Inc., 2004.

[73] Rogers A. *Essentials of Photonics*. CRC Press, 2009.

[74] O. A. Aktsipetrov and A. A. Fedyanin. D.C. electric-field-induced second-harmonic generation in Si-SiO$_2$ multiple quantum wells. *Thin Solid Films*, 294(2):235–237, 1997.

[75] W. Wang, G. Lupke, M. Di Ventra, S. T. Pantelides, J. M. Gilligan, N. H. Tolk, I. C. Kizilyalli, P. K. Roy, G. Margaritondo, and G. Lucovsky. Coupled electron-hole dynamics at the Si/SiO$_2$ interface. *Physical Review Letters*, 81(19):4224–4227, 1998.

[76] Y. D. Glinka, W. Wang, S. K. Singh, Z. Marka, S. N. Rashkeev, Y. Shirokaya, R. Albridge, S. T. Pantelides, N. H. Tolk, and G. Lucovsky. Characterization of charge-carrier dynamics in thin oxide layers on silicon by second harmonic generation. *Physical Review B*, 65:1–4, 2002.

[77] T. Scheidt. *Ph.D. Thesis, Charge Carrier Dynamics and Defect Generation at the Si/SiO$_2$ Interface Probed by Femtosecond Optical Second Harmonic Generation.* Friedrich-Schiller University Jena- Germany, 2005.

[78] P. H. Neethling. *Electric field induced second harmonic measurements of highly boron doped p$^+$-type Si/SiO$_2$*. PhD Dissertation - University of Stellenbosch, 2008.

[79] J. I. Dadap, B. Doris, Q. Deng, M. C. Downer, J. K. Lowell, and A. C. Diebold. Randomly oriented angstrom-scale microroughness at the Si(100)-SiO$_2$ interface probed by optical second-harmonic generation. *Applied Physics Letters*, 64(16):2139–2141, 1994.

[80] D. Hojo, N. Tokuda, and K. Yamabe. Direct observation of two-dimensional growth at SiO$_2$/Si(111) interface. *Thin Solid Films*, 515(20-21):7892–7898, 2007.

[81] J. G. Mihaychuk, N. Shamir, and H. M. van Driel. Multiphoton photoemission and electric-field-induced optical second-harmonic generation as probes of charge transfer across the Si/SiO$_2$ interface. *Physical Review B*, 59(3):2164–2173, 1999.

[82] M. SheikBahae, A. A. Said, M. J. Soileau, D. J. Hagan, and E. W. Vanstryland. Nonlinear refraction and optical limiting in thick media. *Journal Of Optical Engineering*, 30(8):1228–1235, 1991.

[83] D. H. Reitze, T. R. Zhang, Wm. M. Wood, and M. C. Downer. Two-photon spectroscopy of silicon using femtosecond pulses at above-gap frequencies. *Optical Society of America*, 7(1):84–89, 1990.

[84] K. Torizuka, H. Takada, and K. Miyazaki. Low-threshold self-mode-locked Ti:sapphire laser with double dispersion compensators. *Japanese Journal Of Applied Physics Part 1-Regular Papers Short Notes & Review Papers*, 36(2):710–713, 1997.

[85] M. Cernusca, R. Heer, and G. A. Reider. Photoinduced trap generation at the Si-SiO$_2$ interface. *Applied Physics B-Lasers And Optics*, 66(3):367–370, 1998.

[86] G. A. Reider, M. Cernusca, and M. Hofer. Coherence artifacts in second harmonic microscopy. *Applied Physics B-Lasers And Optics*, 68(3):343–347, 1999.

[87] V. I. Gavrilenko. Differential reflectance and second-harmonic generation of the Si/SiO$_2$ interface from first principles. *Physical Review B*, 77(15), 2008.

[88] A. Rumpel, B. Manschwetus, G. Lilienkamp, H. Schmidt, and W. Daum. Polarity of space charge fields in second-harmonic generation spectra of Si(100)/SiO$_2$ interfaces. *Physical Review B*, 74, 2006.

[89] W. Daum. Optical studies of Si/SiO$_2$ interfaces by second-harmonic generation spectroscopy of silicon interband transitions. *Applied Physics A-Materials Science & Processing*, 87:451–460, 2007.

[90] N. Shamir, J. G. Mihaychuk, H. M. van Driel, and H. J. Kreuzer. Universal mechanism for gas adsorption and electron trapping on oxidized silicon. *Physical Review Letters*, 82(2):359–361, 1999.

[91] B.G. Streetman and S. K. Banerjee. *Solid State Electronic Devices*. Prentice Hall, 2005.

[92] E Hecht. *Optics*. Addison Wesley Longman, 1998.

[93] P. H. Neethling, T. Scheidt, E. G. Rohwer, H. M. Von Bergmann, and H. Stafast. Second harmonic generation as a technique to probe buried interfaces. *South African Journal Of Science*, 105(7-8):282–284, 2009.

[94] R. W. J. Hollering, A. J. Hoeven, and J. M. Lenssinck. Optical second-harmonic generation study of Si and Ge deposition on si(001). *Journal Of Vacuum Science & Technology A*, 8(4):3194–3198, 1990.

[95] Z. Marka, R. Pasternak, Y. Jiang, S. N. Rashkeev, S. T. Pantelides, N. H. Tolk, P. K. Roy, and J. Kozub. Band offsets measurement of Si-SiO$_2$ interfaces by internal photoemission induced second-harmonic generation. *Quantum Electronics and Laser Science*, 38:930–931, 2003.

[96] T. Scheidt, E. G. Rohwer, and H. M. von Bergmann. Optical second harmonic generation as a probe for internal electric fields at the Si/SiO$_2$ interface. *South African Journal Of Science*, 101(1-2):91–92, 2005.

[97] B. Jun, Y. V. White, R. D. Schrimpf, D. M. Fleetwood, F. Brunier, N. Bresson, S. Cristoloveanu, and N. H. Tolk. Characterization of multiple Si/SiO$_2$ interfaces in silicon-on-insulator materials via second-harmonic generation. *Applied Physics Letters*, 85(15):3095–3097, 2004.

[98] X. Lu, R. Pasternak, H. Park, J. B. Qi, N. H. Tolk, A. Chatterjee, R. D. Schrimpf, and D. M. Fleetwood. Temperature-dependent second- and third-order optical nonlinear susceptibilities at the Si/SiO$_2$ interface. *Physical Review B*, 78(15), 2008.

[99] H. Bergner, V. Bruckner, L. Leine, and M. Supianek. Reflectivity and transmittance investigations of photoexcited charge-carriers in silicon in the picosecond time domain. *Applied Physics A-Materials Science & Processing*, 43(2):97–104, 1987.

[100] R. A. Cheville, W. B. Haynes, and N. J. Halas. Time-resolved reflectivity studies of the GaAs(100)/oxide and GaAs(100)/ZnSe interface. *Applied Physics Letters*, 59(12):1476–1478, 1991.

[101] N. Fukata, Y. Yamamoto, K. Murakami, M. Hase, and M. Kitajima. In situ spectroscopic measurement of defect formation in SiO$_2$ induced by femtosecond laser irradiation. *Physica B-Condensed Matter*, 340:986–989, 2003.

[102] W. Fischler, P. Buchberger, R. A. Hopfel, and G. Zandler. Ultrafast reflectivity changes in photoexcited GaAs Schottky diodes. *Applied Physics Letters*, 68(20):2778–2780, 1996.

[103] A. J. Sabbah and D. M. Riffe. Femtosecond pump-probe reflectivity study of silicon carrier dynamics. *Physical Review B*, 66(16), 2002.

[104] Z. Toth, B. Hopp, A. Mechler, Z. Bor, S. D. Moustaizis, A. Athanassiou, S. Georgiou, C. Kalpouzos, and C. Fotakis. Reflectivity transients on solid surfaces induced by 0.5 ps high power excimer laser irradiation. *Laser Physics*, 10(1):241–245, 2000.

[105] T. Ikari, A. Fukuyama, T. Murata, M. Suemitsu, N. Haddad, V. Reita, J. P. Roger, and D. Fournier. Carrier recombination velocities at the SiO_2/Si interface investigated by a photo-thermal reflection microscopy. *Materials Science And Engineering B-Solid State Materials For Advanced Technology*, 124:345–348, 2005.

[106] J. M. Liu, L. A. Lompre, H. Kurz, and N. Bloembergen. Phenomenology of picosecond heating and evaporation of silicon surfaces coated with SiO_2 layers. *Applied Physics A-Materials Science & Processing*, 34(1):25–29, 1984.

[107] D. R. Lide. *Handbook of Chemistry and Physics*. CRC Press, 1994.

[108] J. I. Dadap, X. F. Hu, N. M. Russell, J. G. Ekerdt, J. K Lowell, and M. C. Downer. Analysis of second-harmonic generation by unamplified, high-repetition-rate ultrashort laser pulses at Si(001) interfaces. *IEEE Journal of Selected Topics in Quantum Electronics*, 1(4):1145–1155, 1995.